Development of Automated Tape Winding Setup for Thermoplastic Fibre Reinforced Polymer Composites and Bi-Axial Creep Testing Setup for Tubular Coupons

by

Hai Giang Minh Doan

A thesis submitted in partial fulfillment of the requirements for the degree of

Master of Science

Department of Mechanical Engineering
University of Alberta

© Hai Giang Minh Doan, 2019

ABSTRACT

Polymer composite pipelines are gaining popularity for the advantages they have over steel pipelines such as superior corrosion resistance, higher strength-to-weight ratio and increased flexibility. However, polymer composite pipelines, especially those with a thermoplastic polymer matrix, are more prone to creep. Creep can lead to significant deformation and affect the safe operation of the pipeline. There is limited research in the creep behaviour of fibre reinforced thermoplastic polymer composites in tubular coupon form; previous research has focused mainly on flat coupons or thermoset polymer composite pipes.

The first part of this thesis describes a manufacturing process to produce thermoplastic fibre reinforced high density polyethylene tubular specimens. The prototyping setup was developed by adding extra equipment to an industrial filament winding machine. Two batches of high-quality, bonded tubular specimens were produced. The quality of the tubes were verified through dimensional measurements, crush tests and analysis of their microstructure.

The second part of this thesis describes the creep test method developed to determine the long-term behaviour of the material. The specimens were subjected to well-defined loads: 10 MPa pure hoop stress and 5 MPa pure axial compression stress. Two independent measurement techniques, strain gauges and digital image correlation, were employed to measure strain. Strain gauge measurements were in good agreement with theoretical predictions and digital image correlation measurements. The material's Poisson ratio changed during testing, possibly due to fibre realignment. The observed behaviour agrees with results found in literature. The Burgers model and Findley's Power Law were found to closely fit the experimental creep data.

ACKNOWLEDGEMENTS

Thank you to Dr. Pierre Mertiny for giving me the opportunity to go on this journey through graduate school. Your timely guidance was much appreciated throughout the years. The project not only increased my technical knowledge but I felt it pushed me to become a stronger person. It was a challenging process but I did not give up and was forced to tackle obstacles by looking for the solution from different points of view.

Thank you to Alberta Innovates and Shawcor for providing the financial support for the project. The AOP project enriched my experience by involving me in an exciting product development project but also introduced me to a team of knowledgeable and passionate people.

Thank you to the members of the Mechanical Engineering machine shop and electrical shop. I appreciate all the help and technical support you provided me.

Thank you to Hossein Ashrafizadeh, Bernie Faulkner and Jacob Sorken who worked closely with me on developing the manufacturing and/or testing setup. The project's success would not have been possible without you.

Last but not least, thank you to my family and colleagues. I believe our experiences shape who we are and I would not be who I am today if it was for your support.

TABLE OF CONTENTS

LISTS OF TABLES

LIST OF FIGURES

1.0 Introduction to Polymer Composite Pipelines

1.1 Characteristics and Applications of Polymer Composite Pipelines

Canada and the United States have over 3 million kilometers of oil and gas pipelines [1, 2]. According to a Fraser Institute report published in 2015, pipelines are the safest method to transport oil and gas [3]. Although traditionally made from steel or iron, the use of fibre-reinforced polymer composite (FRPC) pipes are gaining popularity [4]. The FRPC pipe which serves as motivation for this thesis is shown in Figure 1. It is composed of a strength bearing fibre-reinforced layer sandwiched between a polymer liner and a protective outer layer [5, 6]. Multiple layers of long continuous bonded fibres [7] are helically wound around the liner to form the strength bearing layer [5]. The polymer outer layer, called a jacket, provides protection for the pipe against external damage.

FRPC pipes provide safety, environmental and cost-savings improvements over steel pipelines. The fluids transported in pipelines can be corrosive [8] and failure of corroded pipes can have major safety and environmental impacts. Pipeline corrosion was responsible for over a third of Alberta's pipeline-related incidents in 2017 [9] and an estimated annual cost of $7 billion USD in the United States (based on a 2001 NACE study) [10]. Corrosion concerns can be alleviated with use of FRPC pipes which have superior corrosion resistance compared to steel pipes [11]. Composite pipes also possess a higher strength-to-weight ratio and greater flexibility; these characteristics help lower installation and transportation costs [12].

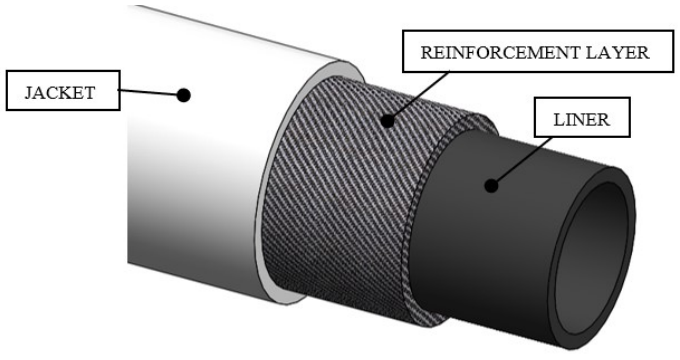

Figure 1: Structure of a FRPC pipe (reproduced based on image in [13])

The combination of weight reduction and corrosion resistance have made composite pipes especially advantageous in deep-sea oil and gas applications [14]. Subsea oil fields are being developed at depths up to 3000 m [15]; the use of FRPC reduces the weight of both the pipe and supporting structures resulting in significant financial savings [14]. Not limited to the oil and gas industry, FRPC pipes are also used in water distribution [16], sewage [17] and geothermal heating systems [18].

The unique properties of FRPC requires special considerations during the pipeline design process. Composites are anisotropic meaning their properties depend on the orientation of the material unlike isotropic materials which have the same properties regardless of direction [19]. Standard ASTM F2686-14 [5] addresses the anisotropic behaviour by specifying the required reinforcing fibre layers in FRPC pipes to be helically wound with layers alternating from +55° and then -55° with respect to the pipe axis. This winding angle is approximately the optimal angle for pipe strength under internal pressure [20]. Temperature also has a major influence on the properties of FRPC. Operating at elevated temperatures can cause some polymers to soften or degrade [21]. The invention of high-temperature polymers such as polyether ether ketone (PEEK) and polyphenylene sulfide combined with the use of carbon fibre has enabled FRPC pipe to be used in continuous operating conditions up to 200°C [22]. Another concern with composite materials is creep; experiencing constant stress will cause the material to continually deform, even at room temperature [23]. The expected lifetime of certain FRPC pipelines is 20 years [24]; therefore, they may experience significant deformation due to creep during this time. Researchers have used experimental and modelling approaches to study the issue of creep. Long-term creep tests lasting up to 10,000 hours [25, 26] have been conducted to quantify the effect of creep on failure strength and life time of the pipe. Models have been developed, based on short-term creep experiments, to predict the long-term creep behaviour of the material [27]. Simulations have an advantage over the experimental approach because multiple geometries can be tested in a relatively short time [28]. Regardless of whether the experimental and/or modelling approach is employed in FRPC pipeline design, an understanding of creep behaviour in polymer composite materials, which will be discussed further in this thesis, is required to ensure a reliable product for the safe transport of the fluid. For this reason, the Advanced Composite Materials and Engineering Group at the University of Alberta has partnered with an industrial partner on a project employing an experimental and modelling approach to the issue of creep. In an effort to

continually improve and develop new product, the industrial partner is developing models capable of predicting long-term material behaviour to incorporate into their design process. The research group will provide reliable creep data to calibrate and verify the models. To achieve this, the research group developed an in-house prototyping and creep testing setup for tubular coupons which is the objective of this study.

1.2 Thesis Objectives

The thesis work is part of a larger collaboration with an industrial partner. The Advanced Composites Materials Engineering Group at the University of Alberta took on the task of producing tubular coupons and conducting creep tests. The data provided by the research group will be used as input to calibrate and verify the accuracy of design models developed by the company.

As a result of the above collaboration, there were two objectives in this thesis work:

1) Conversion of a filament-winding machine to produce high-quality, bonded tubular specimens from glass fibre reinforced high-density polyethylene (GFR-HDPE) tape. Develop and document the manufacturing process and ensure it is repeatable.
2) Development of a testing setup to conduct creep testing of the thermoplastic FRPC tubular specimens under bi-axial loading conditions. The test setup must achieve consistent results that agree with previous research and theoretical results.

1.3 Structure of the Thesis

The thesis is divided into six chapters. The first two chapters provide background information about FRPC pipes and creep theory, respectively. The tape winding and creep testing setups are described in Chapters 3 and 4, respectively. Chapter 5 discusses the characteristics of the tubular specimens and the results of creep testing. The results will include analysis of the initial elastic strains, creep strains, Poisson ratio, strain rate and creep compliance. Limitations and improvements to the test setup are discussed and a comparison of strain gauges and digital image correlation (DIC) are given. Chapter 6 will summarize the achievements of this study and make recommendations for future work.

1.4 Comparison Between Thermoset and Thermoplastic Composite Pipes

A fibre-reinforced polymer composite requires a minimum of two components [19]: the fibres and the polymer matrix. The type of polymer matrix, thermoset or thermoplastic, has a significant influence on the properties and behaviour of the composite. Thermoset (TS) polymers have significant cross-linking, which means they have many covalent bonds between the polymer chains [21]. Due to cross-linking, thermosets do not soften at elevated temperatures and typically exhibit greater strength and hardness than their thermoplastic (TP) counterparts [21].

On the other hand, TPs demonstrate high toughness and impact performance [29]. By applying heat, TPs can be reshaped allowing them to be recycled [30] and electro-fused, a welding process used for pipeline connections [31]. Storing of raw materials and manufacturing of TP-FRPC pipes is also easier because thermoplastics have a longer shelf life and do not require a separate curing process [30]. The advantages of TPs have made it a popular material and many companies around the world, such as Airborne Oil & Gas (Ijmuiden, Netherlands), Magma Global (Portsmouth, United Kingdom) and Shawcor (Toronto, ON, Canada), offer TP-FRPC piping. The widespread use of TP-FRPC further increases the importance of creep research since thermoplastics, without the presence of significant cross-linking, are more susceptible to creep [32].

To address the importance of creep research in thermoplastic composite materials for piping applications, the first part of the thesis research will focus on developing an in-house method to fabricate tubular specimens from glass fibre reinforced thermoplastic high-density polyethylene (GFR-HDPE), a material used for onshore FRPC piping. The second part of the thesis research focuses on developing a creep test setup to test the tubular specimens and increase the knowledge of the material's long-term behaviour.

1.5 Manufacturing Methods of Polymer Composite Pipe

Two methods of producing FRPC pipe are filament winding and automated tape winding. Filament winding machines have existed since the early 1940s [33] and were traditionally used for producing thermoset polymer composites parts. In a wet filament winding setup, as shown in Figure 2, single fibre strands or bundles of fibres, called rovings [34], are pulled from creels

through a resin bath. The fibres are tensioned, by either mechanical or electrical devices, as they leave the creels to control the fibre alignment and void content of the finished part [35]. As the rovings pass through the bath, they are impregnated with the matrix material [36]. Combs are used to keep the rovings separated until they are fed through a wind eye which forms them into a band to be placed on the rotating mandrel [37]. The orientation of the comb and wind eye can be adjusted by rotating the rotation eye. The carriage moves from side to side, allowing the rovings to be placed along the length of the mandrel. The motion of the carriage and the rotation of the mandrel are coordinated to allow the placement of the rovings at specific angles [34]; only one placement angle is allowable per layer. Each pass of the carriage will lay down a band of rovings; multiple passes are required to complete one layer. The thickness of the part is determined by the number of layers wound onto the mandrel. After the fibres are wound on the mandrel, a curing stage is required to enable cross-linking in the polymer [36]. Curing of thermoset composites can occur at room temperature [34], in an oven [35] or an autoclave [36].

Figure 2: View of filament winding setup

In both filament winding and tape winding, fibre-reinforced composite material is wound around a mandrel to form a part. Unlike wet filament winding, tape winding uses premanufactured unidirectional fibre reinforced polymer tape. The tape material is made of long continuous fibres already impregnated with a polymer and then slit into thin strips with rectangular cross-sections. Automated thermoplastic tape winding is an uninterrupted process involving in-situ placement, heating and consolidation of the tape and does not require a curing stage [38]. Consolidation is a process in which heat and pressure are applied to the plies, or layers, of tape to form them into a single structure [36]. A good quality bond requires intimate contact between the newly placed material and the previously placed tape, as well as, autohesion. Autohesion is a process in which polymer chains diffuse between the mating surfaces [39]. Temperature is a critical parameter in the tape winding process. Setting the temperature too low will result in insufficient bonding while too high a temperature will cause material degradation and the polymer to be pushed outward from the tape [40, 41] which could result in voids in the material [36]. The processing temperature for amorphous and crystalline thermoplastics should be above the glass transition and melting point temperature, respectively [42]. Heating sources such as infrared, laser or hot gas blower are used [41] in the tape winding process.

Compaction pressure, tape winding speed, and tape tension are also important parameters [36, 41] to reduce the number of defects. Higher consolidation pressure and longer consolidation time can produce less voids in the completed structure [43]. Rigid or deformable rollers can be used to apply the compaction pressure but deformable rollers will allow better for pressure distribution [44]. Faster processing speeds can result in lower consolidation because there is not enough time for the heat and pressure to induce bonding [45]. In general, the temperature, pressure and length of processing time at which the tape and substrate are consolidated at will determine the quality of the bonding.

1.6 Previous Research on Thermoplastic Tape Winding

The popularity of TP-FRPC and the advantages of tape winding has led to extensive research in the field. Literature review of tape winding setups developed by previous researchers to study consolidation of thermoplastic composite tape was conducted to aid in the development of an in-house tape winding setup. As will be shown, the literature review proved to be valuable

in determining previously used methods to apply heat and pressure for consolidation, as well as, methods to verify part quality. Due to their importance, the influence of temperature, winding speed and compaction pressure were the focus of many studies. Beyeler, Phillips and Güçeri [46] developed a custom experimental setup for hoop-winding and consolidating of carbon fibre reinforced (CFR) polyphenylene sulfide tape employing laser-heating. For their setup, lack of compaction pressure resulted in thick matrix dominant layers between each ply which were not present under higher compaction pressures. For higher compaction pressures, the thickness of each individual ply reduced approximately 25% after consolidation compared to the unprocessed tape thickness. The researchers suggested the dimensional change was a result of the matrix being squeezed out.

Quadrini, Squeo, and Prosperi [47] also built a custom laser-heated hoop-winding setup for use with FRPC polypropylene tape. Part quality was verified by conducting ring compression tests and checking for delamination. It was found varying the processing speed affected part thickness. Slower winding speeds resulted in thinner specimens. Too much heat was added which led to increased matrix flow allowing newly placed plies of tape to penetrate previously laid layers. At the highest processing speed, the thickness of the six-layer part was greater than the thickness of six plies of unprocessed tape. Non-uniform tape thickness, tape continuity and variations in the first placed layer of tape were used to explain the ring's thicker than expected final dimensions.

Several different tape winding setups were developed to study CFR-PEEK. Agarwal [48] used microscopy and differential scanning calorimetry (DSC) to measure void content and crystallinity of ring samples, respectively. Bond strength was determined using beam shear tests, according to the ASTM 2344-84 test standard [49], and double cantilever beam tests. A compaction roller was used with a CO_2 laser for consolidation pressure and heating. The independent variable was laser power, adjusted from 30 watts to 75 watts. Lower interlaminar strength and toughness, resulting from poor bond quality, were observed even for processing temperatures above melting temperature of the material. Poor bond quality was observed even when the void content was less than 2%. These observations led Agarwal to hypothesize that there should be sufficient processing time to allow polymer chains to diffuse in between plies. DSC revealed changes in crystallinity in the finished product was a function of increasing processing temperature. It was suggested the change in crystallinity resulted from annealing of

inner layers as they are repeatedly reheated by the laser as the mandrel rotated. This was supported by the observation that the surface layer, being the last layer, did not have significant changes in crystallinity compared to the original tape.

Mazumdar and Hoa [50] also used microscopy and DSC to study CFR-PEEK rings but their heat source was hot nitrogen gas instead of a laser. Similar to Agarwal, they observed variations in crystallinity for different ring layers. Double cantilever curved beam and peel tests were used to determine bond quality. Thermocouples were inserted in between the middle layers of the rings as the winding process occurred to determine a minimum temperature for good bond quality. To study residual stress, Mazumdar and Hoa observed the amount of overlap or opening that occurred when the rings were cut. Increased heat for constant winding speed reduced the residual stress observed. Lower tape speed resulted in fewer resin rich areas than higher tape speeds; it was suggested this could be due to the matrix being squeezed out or being vaporized from the heat.

Stokes-Griffin and Compston did a series of experiment and modelling work on automated tape placement of CFR-PEEK tape [40] on a flat surface. The setup involved use of a near infra-red laser, deformable silicone compaction roller and infrared thermal camera for temperature measurements. Processing temperature was adjusted within the range of 400°C to 600°C while tape placement speed was set to 100 mm/s or 400 mm/s. Short beam strength tests (following ASTM D 2344) and scanning electron microscopy (SEM) were used to characterize the finished product's interlaminar strength and microstructure, respectively. For this setup, it was found the lower placement speed of 100 mm/s with a processing temperature of 500°C produced the strongest specimens. It was speculated these parameters allowed for adequate processing time and increased crystallinity of the part leading to improved strength properties.

Tannous, Barasinski, Binetruy, and Courtemanche [44] explored the effect of compaction roller material on the required winding tension and slippage of tape axially along the mandrel as it is placed. Tests were conducted using a metal and silicone compaction roller under different compaction pressures and tape tensions. It was found the increased friction between the silicone compaction roller and the tape required higher tension forces to pull the tape through during processing, but the tape experienced less slippage axially. This observation is especially important for applications winding at acute angles since the tape tension will have a significant component acting along the mandrel's axis.

Instead of building custom equipment, modifying existing filament winding machines was a common practice which enabled the fabrication of tubes and rings from TP-FRPC tape. Buijs and Nederveen [41] investigated the effectiveness of preheating the incoming tape, as well as, heating the incoming tape, substrate and mandrel on the consolidation of tape wound specimens. The preheating section employed an infrared heater while heating of incoming tape and substrate was achieved with hot gas torches. Aramid reinforced polyamide-12 prepreg tapes were used to produce tubes with the winding angle close to 90°. The tubes were tested in shear (following ASTM D2344 test standard) and torsion to determine level of consolidation. Processing temperatures had to be within a specific range (220-230°C) to allow proper bonding while not causing fibre buckling or matrix extrusion from the tape. Fibre buckling (possible due to the negative coefficient of thermal expansion of aramid) was controlled by reducing tape tension as more layers were applied. For this setup, a slow winding speed, under 1 cm/s, and a molten matrix were required to achieve proper bonding.

Colton and Leach [43] used a modified filament winding machine to study the importance of consolidation pressure and winding speed on the quality of carbon fibre reinforced PEEK hoop-wound tubes and rings. The setup employed hot gas blowers to heat the incoming tape; infrared heating was also used to preheat the substrate before tape placement. The system had an air-cooled compaction roller to avoid the roller from overheating and damaging the part. Although both the pressure of the compaction roller and winding speed had significance influence on the void content and width of the rings, the winding speed had a greater impact on void content. Increasing compaction pressure reduced the void percentage for slower winding speeds. A slower winding speed, allowed for a longer processing window, resulting in lower void percentage and components with wider final dimensions. The compaction roller was able to smooth over surface flaws and had a positive effect on the surface finish; however, the roller had to be periodically cooled to avoid the tape material from sticking to it. The temperature of the substrate material was also important to ensure good bonding between layers. Preheating the mandrel reduced effects due to different thermal coefficients of expansion of the mandrel and tape material.

Dell'Anna, Lionetto, Montagna and Maffezzoli [45] investigated ultrasonic welding as a heat source for consolidating GFR-poly ethylene terephthalate (PET) tape. Their filament winding machine employed an ultrasonic horn and steel roller. Void content and density of the

pipes were determined using standards ASTM D2734-03 [51] and ASTM D792 [52], respectively. For their setup, a winding speed higher than 0.18 rad/s resulted in decreased density and increased void content due to reduced consolidation time.

There has been a lot of interest in finding the optimal processing parameters for high-strength and high-temperatures materials such as CFR-PEEK but no published studies involving GFR-HDPE materials were found. The importance of GFR-HDPE is growing due to the use of the material in onshore piping applications and its recent qualification for use in the deep-sea oil and gas industry [53]. The material's growing importance necessitates research to determine the appropriate processing parameters to reliably produce high-quality parts from GFR-HDPE tape. Another limitation of the previous research was that the winding angle investigated was 90° (or close to 90°) with respect to the mandrel axis since the focus was mainly on achieving proper consolidation. This leaves a gap for tubes wound at different tape winding angles to be investigated.

2.0 Creep Theory

2.1 Basics of Creep

Fibre-reinforced polymer composites are viscoelastic materials meaning they have some elastic and some viscous properties [23]. Deformation of an elastic material occurs immediately, but it will revert to its former shape after the load is no longer applied. Deformation of viscous materials is time-dependent and permanent. Polymer composites continue to deform over time under an applied load but will try and return to the initial form once the load is gone [23, 54]. The time-dependent behaviour of polymer composite materials results in two long-term phenomena: creep and relaxation [55].

Relaxation occurs when the stress in a material reduces as the material continues to experience constant strain [55]. Creep is the gradual increase in strain of a material subjected to a constant load [23]. It is affected by temperature, loading conditions, time and the properties of the constituent materials of a composite. There are three phases of creep: primary, secondary and tertiary as shown in Figure 3 [55]. The initial elastic strain is caused by the changing bond distances and angles of the polymer chains as load is applied [56] . The initial strain is followed by the primary and secondary, also called steady-state, creep phases. The continued application of force causes the polymer chains to untangle and rearrange themselves resulting in greater alignment of the chains [56, 55]. The strain rate increases during tertiary creep and can eventually lead to failure [57]. The presence of cross-linking in thermoset polymer composites explains why they are more creep resistant than thermoplastic composites: the covalent bonds between the polymer chains inhibit their motion [55]. Network polymers such as epoxies have more bonds between chains than linear or branched polymers such as polyethylene [21].

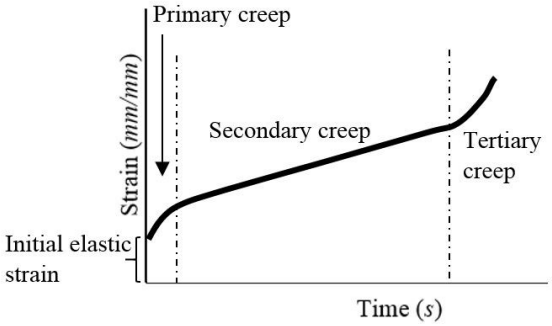

Figure 3: Three stages of creep (reproduced based on image in [58])

Viscoelastic behaviour can be divided into linear and nonlinear. The relationship between stress and strain must be proportional [58] and the superposition principle [23] must be satisfied for linear viscoelasticity to apply. A proportional relationship between stress and strain means a change in the applied stress should produce the same change in the resulting strain. The second condition means the total deformation of a material due to a number of stresses applied at various times will be equal to the sum of the deformations due to each individual load. Another indication the material is linear viscoelastic is the compliance versus time curves at several stress states will be the same [23]. Compliance, $D(t)$, gives the relationship between the strain, $\varepsilon(t)$, and the constant stress, σ_0, experienced by the material as shown in Equation (1). Polymer composites experience both linear and nonlinear viscoelasticity. Due to time dependent and nonlinear behaviour of polymer composites it is difficult to predict the performance and strength of the materials over their lifetime. To aid in the design process, models can be used to predict the long-term properties of the composites.

$$D(t) = \frac{\varepsilon(t)}{\sigma_0} \tag{1}$$

2.2 Viscoelastic Behaviour/Creep Models

Models have been developed to predict linear and nonlinear viscoelastic behaviour. Linear viscoelastic behaviour can be explained using spring and dashpot elements [59]. A linear spring element, shown in Figure 4a, represents elastic behaviour and deforms immediately when a load

is applied. Its behaviour, following Equation (2), where σ is the applied stress, ε is the corresponding strain and E is the Young's modulus. A dashpot element, shown in Figure 4b, represents the viscous behaviour. It behaves according to Equation (3) where η is the viscosity coefficient and $\dot{\varepsilon}$ is the strain rate. Equation (3) shows that applying an instantaneous strain to the dashpot will cause the stress level to jump to infinity; however, since this scenario is not possible, there will always be a delay in the dashpot's deformation. The Kelvin, Maxwell and Burgers models all use the concept of spring and dashpot elements.

(a) (b)

Figure 4: (a) spring and (b) dashpot element

$$\sigma = E\varepsilon \tag{2}$$

$$\sigma = \eta \frac{d\varepsilon}{dt} = \eta\dot{\varepsilon} \tag{3}$$

The Maxwell model, in Figure 5a, connects a linear spring and dashpot element in series while the Kelvin model, in Figure 5b, has them connected in parallel. Equation 4 and Equation 5 gives the strain as a function of time, when a constant stress, σ_0, is applied, for the Maxwell and Kelvin models, respectively. These simple models are used to determine stress-strain relationships in viscoelastic polymers but their assumptions limit their usefulness in accurately predicting creep or relaxation behaviour [60]. For the Maxwell model, the total strain is the sum of the strain experienced by the two elements. For the Kelvin model, the total stress is the sum of the stress experienced by the two elements. Both models do not consider inertia effects. Due to these simplifications, the Kelvin model does not show instantaneous initial strain or the irreversible deformation due to an applied load [59]. Recovery of the strain after removal of the applied load is not present in the Maxwell model; it also does not accurately describe the strain

rate during primary creep. There are significant shortcomings of these models which limits their accuracy; however, combining the two models together, as in the Burgers model, allows for better representation of viscoelastic behaviour.

(a) (b)

Figure 5: (a) Maxwell model and (b) Kelvin model

$$\varepsilon(t) = \frac{\sigma_0}{E} + \frac{\sigma_0}{\eta} t \tag{6}$$

$$\varepsilon(t) = \frac{\sigma_0}{E}\left(1 - e^{-\frac{Et}{\eta}}\right) \tag{7}$$

The Burgers model combines the Maxwell and Kelvin models in series [59] and does not consider inertial effects. The strain-time relationship under a constant stress is shown in Equation (8) which is the sum of Equation (6) and Equation (7). The terms E_1, E_2, η_1, η_2 are material dependent and can be found by curve fitting creep data. Figure 7 compares the strain-time curves provided by the Maxwell, Kelvin and Burgers models. The Burgers model most closely resembles an experimental creep curve; however, the model is only valid for linear viscoelastic behaviour.

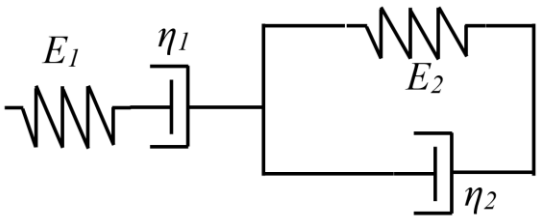

Figure 6: Burgers model

$$\varepsilon(t) = \frac{\sigma_0}{E_1} + \frac{\sigma_0}{\eta_1}t + \frac{\sigma_0}{E_2}\left(1 - e^{-\frac{E_2 t}{\eta_2}}\right) \quad (8)$$

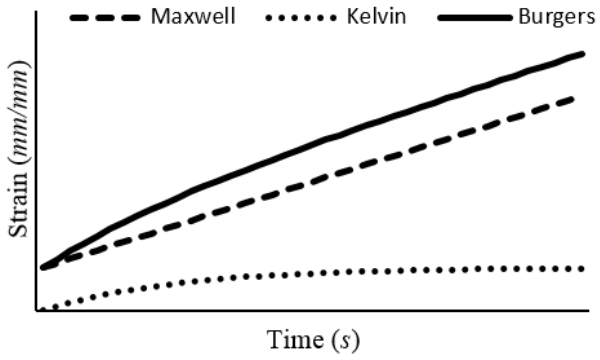

Figure 7: Strain versus time plots for Maxwell, Kelvin and Burgers models

Findley's Power Law, shown in Equation (9), can represent nonlinear viscoelastic behaviour. It was empirically derived and found to model creep in unreinforced plastics but many researchers have applied it to polymer composites [59, 61]. ε_0 is the initial elastic strain, ε^+ is a function of temperature, material and load while n is a material dependent parameter.

$$\varepsilon(t) = \varepsilon_0 + \varepsilon^+ t^n \quad (9)$$

2.3 Previous Research on Creep Testing

A method to conduct creep testing of TP-FRPC tubular specimens is of interest in this study. There are standards for long-term material testing of FRPC: ISO 899 [62] relates to flexural creep in dumbbell-shaped specimens, ISO 7509 [63] concerns with the long-term time-to-failure of TS-FRPC pipe subjected to internal pressure and ISO 7684 [64] deals with the creep of pipes subjected to an external compressive force. No standards were found which are directly applicable for creep testing of TP-FRPC pipes under internal pressure; therefore, review of previous research had to be conducted. The literature review for creep testing methods was divided into two focus areas: thermoset and thermoplastic polymer composite. Being the more mature technology, publications for thermoset composites were more readily available; the scope of the review for thermoset composites was limited to creep tests conducted on tubular specimens. The goal was to determine test procedures and information obtained from creep tests of tubular specimens. For thermoplastic composites, creep tests on both laminates and tubular specimens were of interest. The goal was to understand the behaviour of the material and learn which models could be used to predict the viscoelastic behaviour of a thermoplastic matrix.

2.3.1 Thermoset Pipe

Vlasov et al. [65] looked at the creep behaviour of GFR-epoxy and GFR-polyester pipes subjected to internal pressure. The pipes with polyester resin were made with winding angles of 35° and 45° while the epoxy pipes had winding angles of 45°. For extra protection, a coating of polyester resin was applied to the inner surface of the pipes. Internal pressure, at 10% to 80% of the short-term leak pressure of the part, was applied and maintained until liquid began to form on the outside surface of the pipes. Strain gauges and a strain meter was used to measure axial and hoop strain. Under high loading conditions, the secondary creep phase was short or not present while under low loading conditions, tertiary creep did not occur. It was found the strain limit of the matrix material determined when leakage occurred.

Ghorbel [66] also noted the influence of matrix ductility in his creep tests. Ghorbel studied the effects of water absorption on the creep behaviour of GFR polyester resin pipes and GFR vinylester pipes. The fibre layup for both sets of pipes was ±55° [67]. The samples were

soaked in water at 60°C for 3000 hours before being pressurized. Extensometers were used to measure axial and hoop strain. The creep in hoop direction was negligible. The material's time-dependent creep behaviour followed Findley's Power Law. The material creep parameters were determined using least squares fit regression.

Yao and Ziegmann [68] also studied the effects of moisture content on creep and proposed moisture absorption and temperature variations produced similar effects on the long term properties of GFR-epoxy composites. Two sets of flexural creep tests were conducted; one for samples with various moisture content at room temperature and another for dry specimens at temperatures ranging from 23°C to 143°C. Load was applied for 20 minutes followed by a 20 minute rest period to allow for recovery. A linear variable differential transformer (LVDT) was used to measure deflection of the pipes. Creep compliance was compared between the test results to determine relationships between moisture content and temperature variation. Increased moisture content and increased temperature resulted in degradation of the material properties.

Xian et al. [69] also noted the detrimental effects of water absorption on long-term material properties subjected to flexural loads. Before testing, GFR polymer square tubes were submerged in water baths at 20°C, 40°C and 60°C for six months. The tubes were then subjected to three-point bending loads ranging from 40% to 60% of the ultimate flexural strength for a period of over 600 hours. Strain was measured using fibre Bragg grating sensors. Increased water absorption was detrimental to the bonding at the matrix-fibre interface and weakened the material. Specimens at 50% loading of ultimate flexural strength reached steady-state creep within a few hours but it was approximately 25 days before second phase strain rate was observed for samples loaded at 30% of ultimate flexural strength.

Yang et al [70] also used three-point bending loads to determine long-term creep behaviour. Isothermal and cyclic thermal flexural creep tests were conducted on CFR-epoxy tubes. The tubes had a fibre layup of $[\pm 15/0/90]_s$ and were subjected to loads ranging from 45% to 75% of the ultimate flexural strength at temperatures of −60°C, −20°C, 25°C, 60°C, and 100°C. Test duration was over 500 hours. Strain gauges were used to measure axial and hoop strain. Higher loads and higher temperatures resulted in a higher strain rate. No creep was observed at temperatures below −20°C. The material parameters for the Findley model were determined using the experimental data.

2.3.2 Thermoplastic Laminates

Due to their different material structure, certain models used for representing thermoset composites might not be suitable for use with thermoplastics [71]; therefore it is important to explore previous research for suitable models. Fliegener, Hohe and Gumbsch [71] developed a finite element simulation using a modified Burgers model to account for nonlinear viscoelasticity and then compared it to experimental results. Polypropylene plates reinforced with discontinuous long glass fibres (up to 50 mm in length) were loaded parallel and then perpendicular to the fibre orientation. Tests were conducted for loads ranging from 2.5 MPa to 12.5 MPa (50% of the quasi-static strength) at room temperature with 50% humidity for approximately 167 hours. An extensometer was used to measure strain. The parameters for the Burger model were determined numerically and then used as input for the finite element simulation. There was good agreement with experimental results but the simulation consistently underestimated the total strain while overestimating the strain rate in the secondary creep region. The linear model could provide upper and lower bounds for the creep curve.

Xiao [72] conducted creep and recovery experiments on CFR-PEEK laminates under various uniaxial tensile loadings. 90°, 16-ply dog-bone specimens were tested at 95°C, 125°C and 150°C while 15°, 12-ply specimens were tested at temperature ranges between 24°C and 121°C (24°C ,44°C, 74°C, 91°C,106°C and 121°C). One set of specimens was allowed to creep for 20 minutes followed by a recovery period of 200 minutes. A second set of specimens had a creep test duration of 50 minutes with a recovery period of at least 600 minutes. An air oven served as a test chamber; thermocouples were employed to measure temperature. Strain was measured using strain gauges. Both sets of specimens exhibited similar creep behaviour. The recovery compliance versus time curves for the 15° laminates changed shape with increasing load while the recovery compliance curve shape for the 90° laminates remained relatively constant. The difference in recovery was explained by the crystalline morphology of the material and its different response to transverse and shear loadings.

Nguyen and Ogale [73] studied the creep behaviour of CFR-PEEK under bending loads at temperatures ranging from 120°C to 160°C . 0° and $[\pm 45°]_s$ laminates were aged for 10 hours before conducting four-point bending tests lasting approximately one hour. Strain gauges in a half-bridge arrangement measured strain. Creep compliance along the fibre direction was

predominantly time independent while the $[\pm 45°]_s$ laminate exhibited greater creep compliance which varied with time. Loading rate, temperature and loading level affected the initial deformation of the material. Too quick of a loading rate would result in overshoot.

Brauner, Herrmann, Niemeier and Schubert [55] used a modified Burger model with an interpolation method to develop a finite element model and compared its predictions to data from tensile creep tests of GFR-polypropylene laminates following the DIN EN ISO 899-1:2003 [74] test standard. Loads ranging from 15% to 30% of the maximum allowable load were applied parallel, perpendicular and at 45° to the fibres alignment direction. The tests were conducted for 144 hours at 23°C, 50°C and 80°C. The model had a maximum average deviation from the experimental data for the unidirectional laminates of less than 10%. The model was less reliable for higher load, higher temperature and longer test durations.

2.3.3 Thermoplastic Pipe

Kruijer, Warnet and Akkerman [75] developed a theoretical model to predict long-term deformations in thermoplastic pipe subjected to internal pressure and then compared its predictions to experimental creep test data. The test pipes had two layers of helically wound steel-reinforced HDPE (type PE100) tape wrapped over top of a liner made of the same grade HDPE. The first and second tape layers had a wind angle of -57° and +57°, with respect to the pipe axis, respectively. The pipe was held at a constant pressure of 10 MPa (100 bar) for three hours at room temperature. Two tests were conducted with loading rates of 0.5 MPa/s (5 bar/s) and 0.025 MPa/s (0.25 bar/s). The researchers designed an LVDT device to measure axial and hoop strain. Due to the effect of tape angle, the pipe lengthened significantly more in the axial direction than in the hoop direction. The slower loading rate of 0.025 MPa/s resulted in a much higher strain in the pipe before test pressure was reached. The model predicted hoop strain more accurately than axial strain. The slower loading rate of 0.025 MPa/s resulted in a more accurate prediction of the model for axial strain; the researchers hypothesized the slower rate (lower stress rate) introduced less nonlinearity to the HDPE.

The literature review conducted for this study indicates that there is significant research in the area of creep behaviour of both thermoset and thermoplastic polymer composite materials. It provides valuable insight to some of the parameters which affect creep such as temperature,

applied stress, moisture, and matrix properties. This information is summarized in Table 1. Knowledge of previous experimental setups helped in the development of the test setup for this study; however, is clear that creep data is only accurate and applicable to the specific material for which it was studied. There is still a need for creep data of GFR-HDPE, which is the focus of this study. Creep testing of TP-FRPC pipes is limited and most studies have focused predominantly on laminates, the use of tubular specimens in this study will avoid the free-edge effects experienced by laminates [76].

Table 1: Parameters affecting creep in polymer composite materials

Reference	Composition	Key Points
Yang et al [70]	Carbon-fibre/epoxy	*"the creep rate increased with increasing stress and temperature levels"*
Yao [68]	Glass-fibre/ epoxy	*"the increment of short-term creep compliance became bigger as moisture content increased"*
Fliegener [71]	Glass-fibre/ polypropylene	*"effects of the nonlinearity of the matrix on the creep behavior of the composite were…significant"*
Brauner [55]	Glass-fibre/ polypropylene	*"in fiber direction, no creeping was measured"*
Nguyen [73]	Carbon-fibre/ PEEK	*"a higher degree of crystallinity is known to display a smaller time-dependent response"*
Nguyen [73]	Carbon-fibre/ PEEK	*"a very fast rate of loading…resulted in an overshoot in the deformation"*

3.0 Automated Tape Winding Setup

3.1 Tape Material

GFR-HDPE tape (HDPE Tape – (CFRT), Shenggang, Taizhou, ZJ, China) was used to fabricate the tubular specimens. As per the manufacturer, the thickness and width of the tape is 0.33 mm and 49 mm as demonstrated in Figure 8. The fibre weight to matrix weight fraction of the tape was verified by fibre burnout tests to be within manufacturer specifications of 60 ± 2 %.

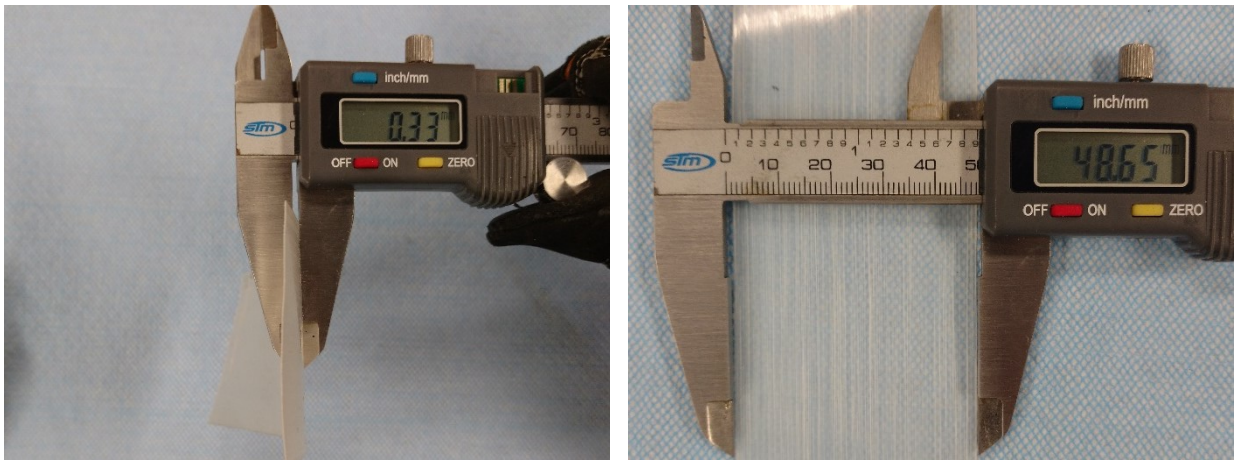

Figure 8: Dimensions of the GFR-HDPE tape

3.2 Determining Tape Melting Temperature

Fibre reinforced composites have been shown to have different melting temperatures than the pure matrix material [72] . Given the importance of processing temperature, the approximate melting temperature of the tape was determined. 0.125 m long sections of the unprocessed tape were cut and then placed in a preheated oven for 1 hour at 10°C increments ranging from 120°C to 150°C. At 120°C, the tape section was unchanged but above 130°C melting was observed. Visible material degradation of the tape was not observed on the section heated at 150°C.

3.3 Tape Winding Equipment

The filament winding machine (WMS-4 Axis, McClean-Anderson, Schofield, WI, United States) owned by the Advanced Composite Materials Engineering Group at the University of Alberta was modified to enable the production of tubular specimens made from GFR-HDPE tape. Additional equipment for storing and guiding the incoming tape, as well as, consolidating the part was added to the existing machine. The current prototyping setup is shown in Figure 9. From the tape creel the tape is directed through the guide roller which guides the direction of the tape as shown in Figure 10. The tension on the tape was controlled by friction between the outer metal plate and inner cardboard core of the tape creel; tightening the knob on the tape creel increased the tension.

Hot-air blowers are less expensive and easier to modify for processing different tape widths than laser or infrared heating sources [77]; therefore, a hot-air blower (Hotwind Premium, Leister Technologies AG, Kaegiswil, Switzerland) was used to heat the incoming tape as it leaves the guide pulley. An aluminum compaction roller was used to apply pressure to the placed tape. The compaction force applied by the compaction roller was spring-controlled. The spring constant measured for the spring was 2.8 N/mm. The compaction roller has 13 thru-holes drilled along its axial direction. Tubing is used to direct compressed air at the roller's holes to cool it during manufacturing and thus prevent degradation of the tape.

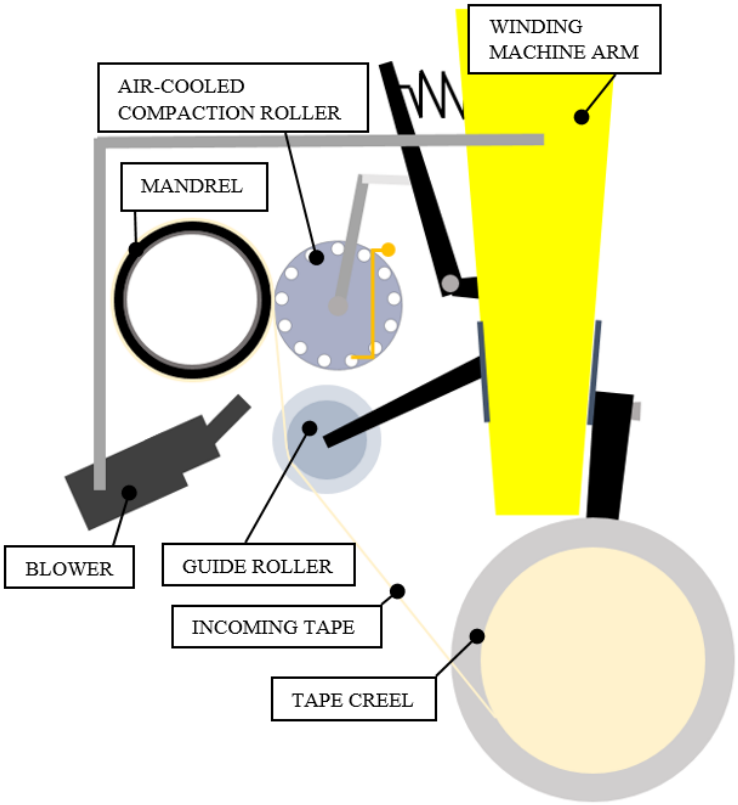

Figure 9: Diagram for prototyping setup

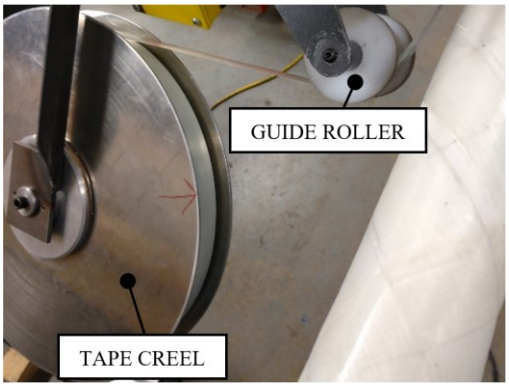

Figure 10: Direction of incoming tape

Although the thermal imaging camera (FLIR E60, FLIR Systems, Wilsonville, OR, United States) was not available for the tape winding sessions specific to this study, it was used in previous tape winding sessions with a similar tape material. the temperature of the incoming tape, compaction roller and placed tape can be monitored with a thermal imaging camera as demonstrated in Figure 11. Due to the different emissivity of the aluminum roller, the temperature measured for the roller is not accurate, but it is possible to see the temperature distribution in the roller during the process. The supply pressure of compressed air for cooling the roller was set to 448 kPa (65 psi) for this study but valve knobs shown in Figure 12 were adjusted to control the air flow to the roller to keep the roller's temperature from degrading the tape.

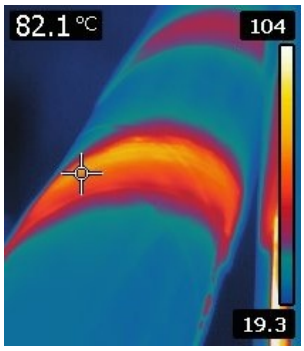

Figure 11: Thermal image of placed tape

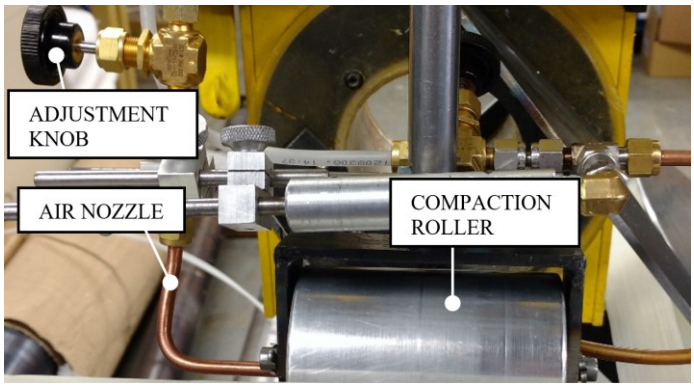

Figure 12: Cooling system for compaction roller

3.4 Tubular Specimen Fabrication

The winding angle for the tubes was chosen to be -45°/+45° since this winding angle is known to produce matrix-dominant properties [73] and provide the lowest Young's modulus in pipe hoop and axial direction compared to other cross-ply winding angles [78]. It is expected that the creep response of the material, which is highly dependent on the matrix properties, would be most pronounced for this winding angle. The following describes the process to fabricate a 1.37m long tube with 10 layers with -45°/+45° winding angle.

An aluminum tube, with an outer diameter of 50.8 mm, acted as the structural mandrel for the incoming tape. 1.02 mm gauge metal wire was wrapped around the mandrel to increase

its diameter. A plastic liner was then slid over top of the aluminum tube; the wire reduced the clearance between the metal tube and liner to prevent rotation during the fabrication process. The use of a low thermal conductivity liner with a relatively similar coefficient of thermal expansion to the tape (at least compared to a metal mandrel) has two advantages: reduced fibre waviness [79] and reduced heat conducted away from the tape as it is placed on the mandrel. It was not desired for the tape to bond to the liner; therefore, aluminum foil was wrapped over the liner. A release agent (MAC-860, McLube, Aston, PA, United States) was applied and allowed to dry. Figure 13 shows the mandrel prior to tape placement. A machine program (filename: 2_6inch45d_tape44.mmt) was loaded into the filament winding machine. The program specified the winding angle, ±45°, and number of passes, three, per layer. (The carriage arm was adjusted to have a 50.8mm offset and 1° eye rotation to best achieve ideal tape compaction.)

Figure 13: Mandrel prior to tape placement

Before the first pass, the GFR-HDPE tape was manually secured to the mandrel with high-temperature adhesive tape. Since bonding to the mandrel was not desired, the first layer was placed on the mandrel at a quicker speed than the subsequent layers; this speed allowed sufficient heating to allow the tape to conform to the shape of the mandrel. For subsequent passes, the travel speed of the carriage and mandrel rotation speed was reduced from 3% to 2% of the machine's maximum allowable mandrel rotation speed to allow the tape to reach its melting temperature. After each pass of the tape, the tape was cut from the creel and taped down to the mandrel. The carriage would then return to its initial position and start the second pass. After the initial layer was complete, the carriage started from the other end of the tube and placed the tape at the -45° angle. This process was repeated until 10 layers of the tape had been placed. A 'heat and roll' pass was used when necessary to ensure bonding and smooth out the surface. It was an additional pass where no new tape was placed but allowed the hot air blower and

compaction roller to apply additional heat and pressure to the already laid tape. The specimens were produced in two batches using different processing parameters. Table 2 and Table 3 show the processing parameters for all layers of tape to produce the tubes.

Table 2: Processing parameters for tape winding batch #1

Layer(s)	Carriage Speed (%)	Hot-air Blower Fan Setting	Hot-air Blower Heater setting
1	3%	3	9
2 to 7	2%	3	9
8 to 10	2%	3	9.5

Table 3: Processing parameters for tape winding batch #2

Layer(s)	Carriage Speed (%)	Hot-air Blower Fan Setting	Hot-air Blower Heater setting
1	3%	3	9
2 to 4	2%	3	9
5 to 8	2%	3	9.5
9 to 10	2%	3	10

The thermal imaging camera was not available during the winding sessions used to produce Batch #1 and Batch #2 of this study, so the tape was visually monitored to check for adequate melting of the tape. After fabrication, the tube was cut into sections. The ends of each tube, where the tape was secured with the high-temperature adhesive tape was considered waste and not used for testing. From each tube, four 203.2 mm (8 inch) long tubular specimens were cut; 12.7 mm (0.5 inch) long rings were cut from in between each specimen. The rings were used for crush tests to check for bond quality.

4.0 Creep Testing Experimental Setup

4.1 Testing and Data Acquisition Equipment

Creep tests were conducted in a tri-axial testing machine. Digital image correlation (DIC) and strain gauges were used to measure strain. Figure 14 shows the layout of the equipment and Figure 15 depicts how they are involved in the test process. The testing software (MTS Station Manager, MTS Systems, Eden Prairie, MN, United States) sends instructions to the micro-controller (MTS Model 458.10 MicroConsole) which activates the actuators in the testing machine and pressure intensifier to apply axial loads and pressurize the specimen. While the creep test is running, a strain gauge on the specimen measures its physical deformation and relays the electronic signal to the strain gauge signal conditioner. The signal conditioner amplifies the signal and information is recorded by the testing software. Also during the creep test, the cameras for the DIC system are taking pictures of the specimen via the image capture software (Vic-Snap, Correlated Solutions, Irmo, SC, United States). After the test is complete, image analysis software (Vic-3D, Correlated Solutions, Irmo, SC, United States) is used for post-processing the data and calculating strains. The strain measurement techniques are independent of each other and are used for comparison. The following section will describe the test software and the principles of strain gauges and DIC in more detail.

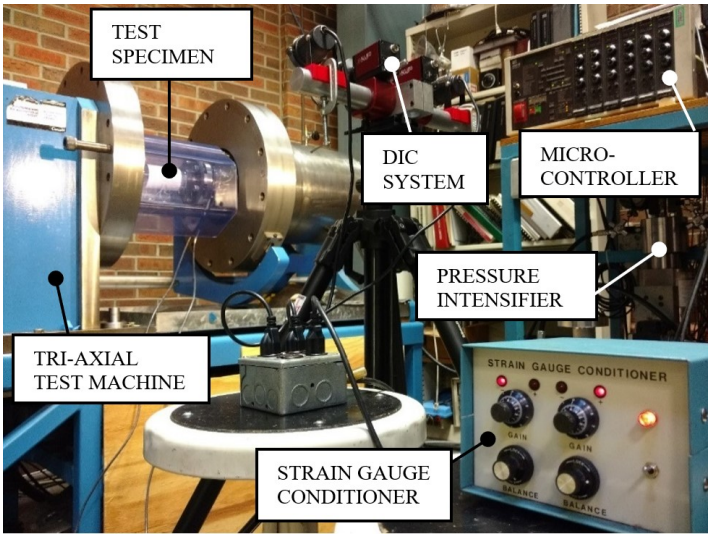

Figure 14: Components for test setup

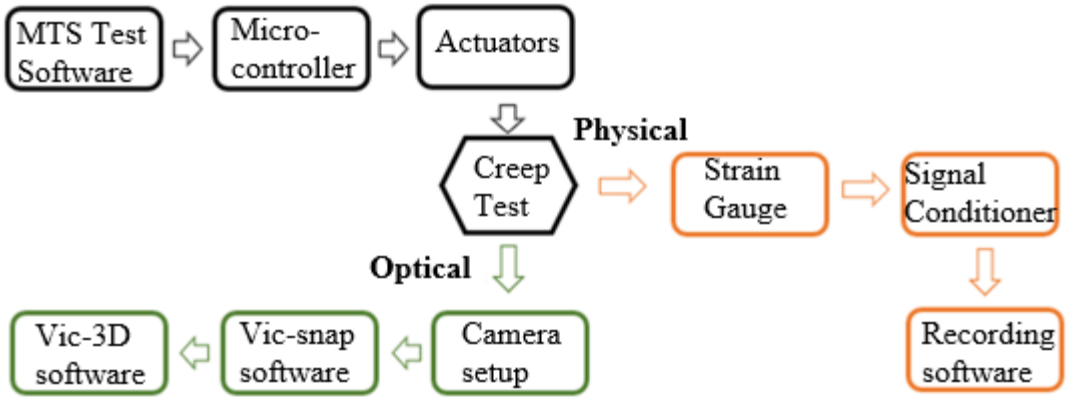

Figure 15: Flow chart for testing procedure

4.1.1 MTS Test Software

Figure 16 shows the graphical user interface (GUI) for the MTS test software. The creep test program is divided into five functions: Data Acquisition (DAQ), Ramp Up, Hold, Pressure Monitor and Ramp Down. The DAQ and Ramp Up functions activate at the start of the test. DAQ is used for recording test data while Ramp Up provides a signal for the microcontroller to gradually apply the force and pressure following a linear ramp function until the desired load level is reached. Once the desired load level is reached, the Hold function holds these loading conditions constant for the specified duration of the test. The Pressure Monitor function activates simultaneously with the Dwell function and interrupts the Hold function if a failure event was detected. In this case, a failure event is triggered if the pressure drops to below 50% of the desired hold pressure. The Ramp Down function ramps down the applied loads to zero and marks the completion of the test.

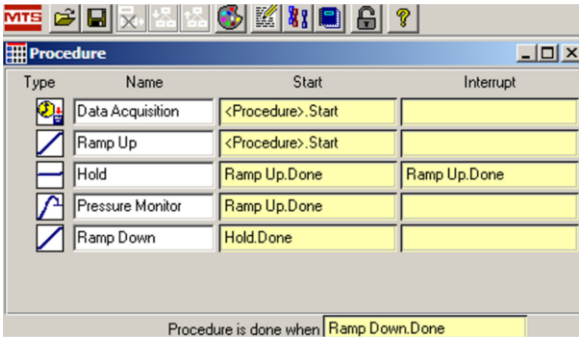

Figure 16: GUI for MTS test software

4.1.2 Strain Gauges

The tee-rosette strain gauge (CEA-06-250UT-350, Micro-Measurements, Raleigh, NC, USA) was selected to simultaneously measure the axial and hoop strains during creep testing. Its operating temperature is between -75°C and 175°C and can measure strain in the ±5% range. The strain gauge on the specimen (the active strain gauge) is connected in series to a dummy gauge and signal conditioner to form a quarter-bridge Wheatstone bridge arrangement with temperature compensation. The dummy gauge was made by applying the same type of strain gauge to a strip of unprocessed tape; the strain gauge was oriented at a 45° angle to the fibres so it would have the same orientation in respect to the fibres as the one on the test specimen. A lacquer coating (M-Coat D, Micro Measurements, Raleigh, NC, USA) was applied to protect the surface of the dummy gauge.

An built in-house signal conditioner based on the Vishay 2100 signal conditioner was used to amplify the signal from the Wheatstone bridge. The device has two channels; one to receive the axial strain signal and the other for the hoop strain. The excitation voltage was set to 5.00 V based on the manufacturer's recommendation [80] which takes into account the size of the strain gauge and substrate material. The electrical circuit used to connect the active strain gauge to the signal conditioner is shown in Figure 17. Lead wires (26 AWG) were soldered onto the active strain gauge but to reduce the amount of soldering required intermediate pin connectors were used to connect the active strain gauge to the dummy gauge and shielded cable. To reduce electromagnetic interference, 22 AWG shielded cable was used to run from the intermediate connector to the signal conditioner.

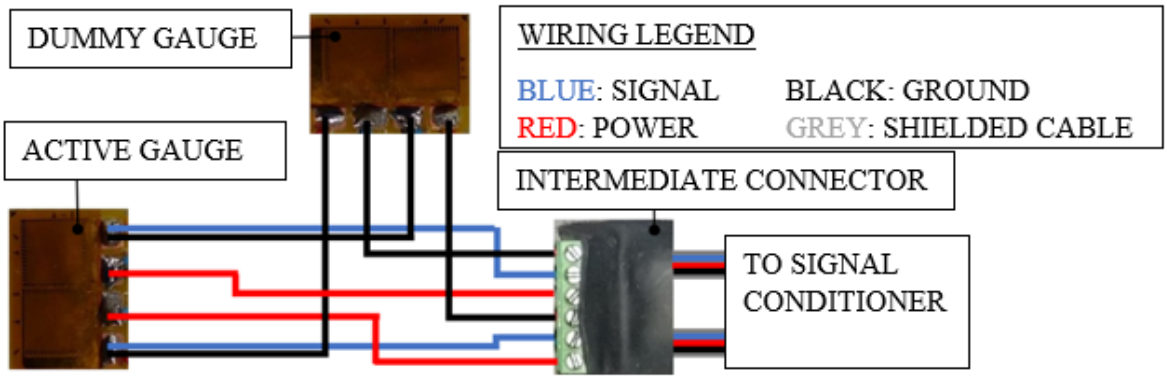

Figure 17: Strain gauge wiring

The signal conditioner will output the strain experienced by the strain gauge in terms of voltage. The equation to convert this voltage into strain is based on the principle of the Wheatstone bridge [81]. In the Wheatstone bridge circuit shown in Figure 18, there are four resistors (R_1, R_2 ,R_3, and R_4) and the relationship between output voltage, V_{out}, and excitation voltage, V_{exc}, is given by Equation (10). There is no output voltage if all the resistances are the same. A change in resistance of one of the resistors will result in an output voltage. The resistance change, ΔR, in a stressed strain gauge is given by Equation (11) where GF is the gauge factor, ε is the strain experienced by the strain gauge and R_{SG} is its initial resistance. The gauge factor is a measure of the fractional change in electrical resistance of the strain gauge for a given fractional change in its length; GF commonly has a value of 2 [81]. The strain gauge in this study had gauge factor values of 2.14 and 2.16 for the axial and hoop directions, respectively. Replacing one of the resistors in a Wheatstone bridge with a stressed strain gauge will result in an output voltage given by Equation (12), which is obtained by combining equations (10) and (11) if all resistances were initially the same.

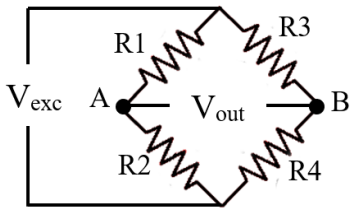

Figure 18:Wheatstone bridge

$$V_{out} = \left[\frac{R_4}{R_3 + R_4} - \frac{R_2}{R_1 + R_2}\right] V_{exc} \tag{10}$$

$$\Delta R = R_{SG} GF \varepsilon \tag{11}$$

$$\frac{V_{out}}{V_{exc}} = -\frac{GF\varepsilon}{4}\left[\frac{1}{1 + \frac{\varepsilon GF}{2}}\right] \tag{12}$$

4.1.3 Digital Image Correlation (DIC)

Digital image correlation (DIC) is an optical measurement technique that captures the movement of an object in a series of images and then compares the differences between those images to provide quantitative information such as displacement and strain [82]. To determine the specimen's displacement, the Vic-3D image analysis software divides each image into a number of subdomains [83]. Each subdomain has a different pattern and the software views each subdomain as a matrix of numbers, as demonstrated in Figure 19, based on its pattern. Black and white pixels have a value of 0 and 100, respectively. After motion, the software tracks the subdomain by comparing the new image to the original. The software calculates a similarity score, also called the correlation function, and the location that results in the lowest error is deemed the new location of the subdomain.

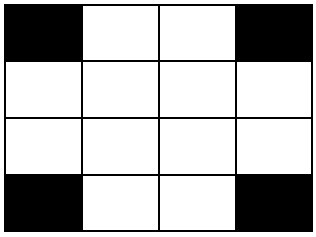

(a)

0	100	100	0
100	100	100	100
100	100	100	100
0	100	100	0

(b)

Figure 19: (a) Subdomain image on screen and (b) image stored by VIC-3D

Like strain gauges, DIC only captures the strain on the surface of the specimen which makes it a good method to compare the strain measurements. To calculate strain, the Vic-3D image analysis software converts the image into a grid of points [84]. Each point has information on its position and displacement obtained from the correlation function. The step size determines the distance, measured in pixels, between each data point. The grid is divided into triangular elements as shown in Figure 20(a) and the software tracks the movement of these elements. By computing the amount each triangle has been deformed as demonstrated in Figure 20(b), the strain tensor for each triangle can be determined. The strain for the data point is interpolated from the strain of the triangles around it as demonstrated in Figure 20(c). To smooth out the noise, the strains from a number of data points are grouped together. The number of data points in each group are determined by the filter size. The surface of the specimen must have a random,

non-repeating pattern so each triangular element can have a unique appearance, allowing the software to track its motion. The pattern is called a speckle pattern and can be applied using felt markers, inkjet printing or spray paint [85].

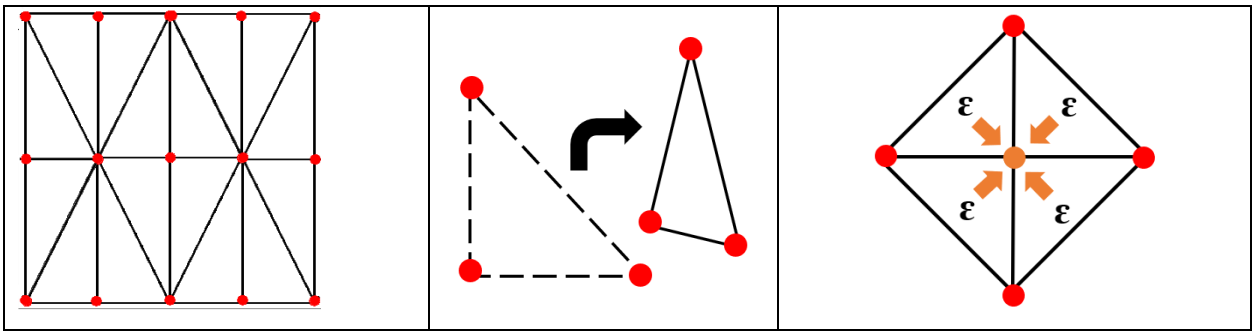

Figure 20: (a) Grid of points for DIC, (b) deformation of triangle element, (c) interpolating strain (reproduced from [84])

The components of the DIC system, seen in Figure 21, consists of two camera lenses (28-85 mm, Nikon, Tokyo, JP) each attached to CCD cameras (Pike F-421, Allied Vision Technologies GmbH, Stadtroda, Germany) and two LED lights. The 4-megapixel cameras have a resolution of 2048 x 2048 and a maximum frame rate of 16 fps. The LED lights were chosen to increase the brightness of the scene while minimizing the amount of heat produced since heat radiation can distort the DIC strain measurements [86] and raise the specimen temperature. The components are placed on a sturdy tripod (Manfrotto 3258, Lino Manfrotto + Co., S.p.A, Cassola, VI, Italy).

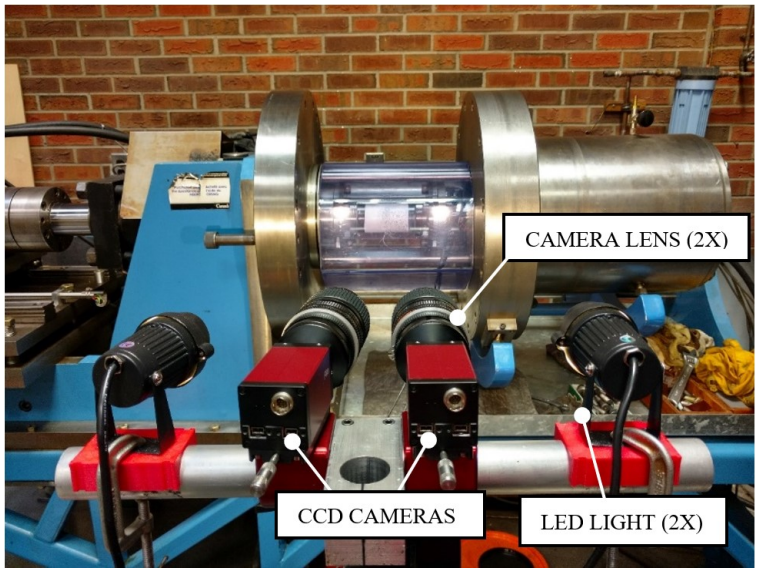

Figure 21: Components for the DIC system

4.1.4 Vic-Snap and Vic-3D User Interface

Figure 22 shows the GUI for the image capture software, Vic-Snap. It displays the image of the specimen as seen by the two cameras. For the DIC process, two types of images are used: calibration images and speckle images. Calibration images are required for syncing the two cameras and speckle images are the pictures of the specimen which are used for strain calculations. The calibration process will be described in more detail in Section 5.2.5. For image capture, the total acquisition time and acquisition interval for the images can be selected using the "Timed Capture" button. The calibration and speckle images are then imported into Vic-3D for processing. The GUI for Vic-3D is shown in Figure 23. Once imported, the list of speckle and calibration images are shown on the left-hand side of the screen. The buttons to calibrate and analyze the images are in the toolbar.

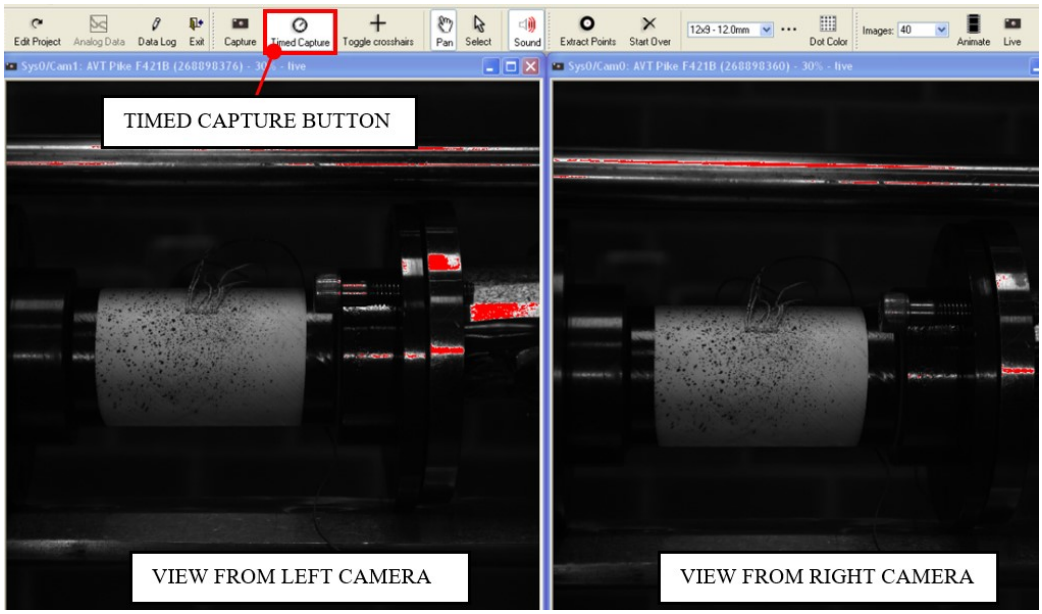

Figure 22: Graphical user interface for Vic-Snap

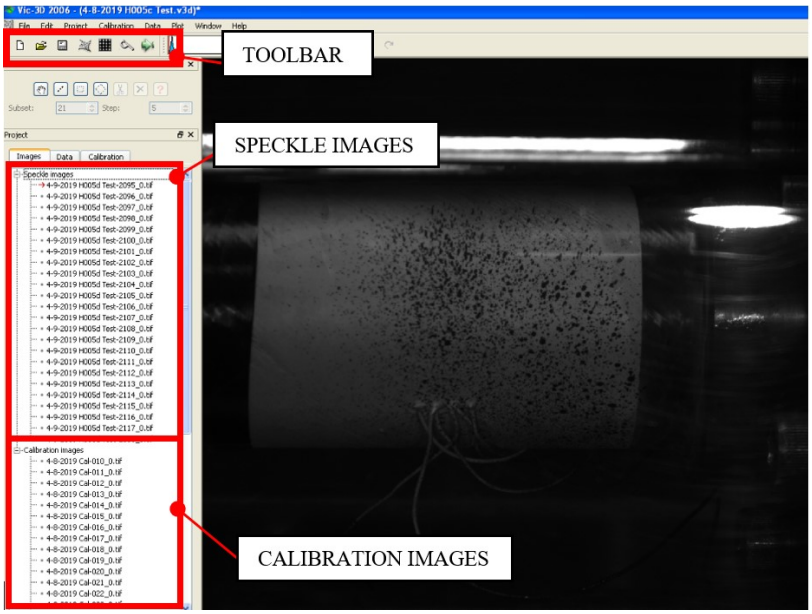

Figure 23: Graphical user interface for Vic-3D

4.1.5 Test Conditions

The first test condition for the tubular samples was 10 MPa pure hoop stress. HDPE has been demonstrated to creep at stresses as low as 2 MPa at room temperature [87]. It was expected GFR-HDPE would experience creep at low stresses as well since creep behaviour is

predominantly determined by the properties of the matrix material. In this case, a stress value of 2 MPa was deemed too low to be within a reasonable operating range for the testing equipment. Therefore, a stress value of 10 MPa was chosen. The higher stress would also result in reaching steady-state creep more quickly, which is a benefit since, for safety reasons, the testing machine is not allowed to operate overnight. Although the test pressures for this study are low, the stresses in the specimens are similar to the stresses used by Vlasov et al. [65] for their creep tests of thermoset composites pipes. Those specimens were subjected to hoop stresses as low as 5.5 MPa although for longer periods of time. Testing at typical pipeline operating pressures was not required in this study because the purpose is to provide creep data as input to calibrate and verify numerical models; therefore, well-defined loads that induce creep in the material was considered sufficient for these purposes.

The specimen is deemed a close-ended pipe since it is not infinitely long and its ends are capped by the piston and fixture on the testing machine, which results in axial forces during pressurization. The pure hoop loading condition was achieved by applying an internal pressure while the piston of the test machine applied a compressive force to cancel out the axial force created by the internal pressure. Free body diagrams (FBD) as shown in Figure 24(a) and Figure 24(b) were used to calculate the necessary test pressure and axial loads. The calculations were made using thin wall assumptions which is valid for tubes that have a thickness-to-inner-diameter ratio less than 0.05 [88]. The pressure, P, or stress in an object, is determined by the amount of force, F, over a given area, A, as shown in Equation (13). The cross-sectional view of the specimen is seen in Figure 24(a). The internal pressure, $P_{i,}$ of the specimen and the outside atmospheric pressure, $P_{o,}$ act on the area outlined by orange and purple lines, respectively. The force in the hoop direction, F_H, is acting within the walls of the specimen. By summing the forces in the hoop direction, the force acting in the specimen along the hoop direction in terms of pressure is given by Equation (14). Combining Equation (14) and Equation (13) gives the hoop stress of the specimen. In calculating the required test pressure, the gage pressure of the testing equipment is used for P_i; therefore, the value for P_o was considered to be zero. Figure 24(b) was used to determine the required axial force to cancel out the axial force induced by internal pressure. The internal pressure acts on the area enclosed by the circle with diameter, d_i, while outer pressure acts on the area of the circle with diameter d_o. By summing the forces in the axial direction, the axial force, $F_{A,}$ given in terms of the pressures is shown in Equation (16). The axial

stress experienced by the tube, σ_{axial} shown in Equation (17) , was determined by combining equation (16) and Equation (13). The ability to test specimens under comparatively low loads has the advantage of reducing the risk of specimen leakage or slippage from the end fittings which would interrupt the test.

The second test condition for the tubular specimens was 5 MPa in pure axial compression. The specimen would not be pressurized while a compressive axial load was applied. The required axial load was calculated by setting σ_{axial} in Equation (17) to zero and solving for F_A. This allows the study of the material's response to compressive loads and demonstrate the difference between 5 MPa and 10 MPa stress levels.

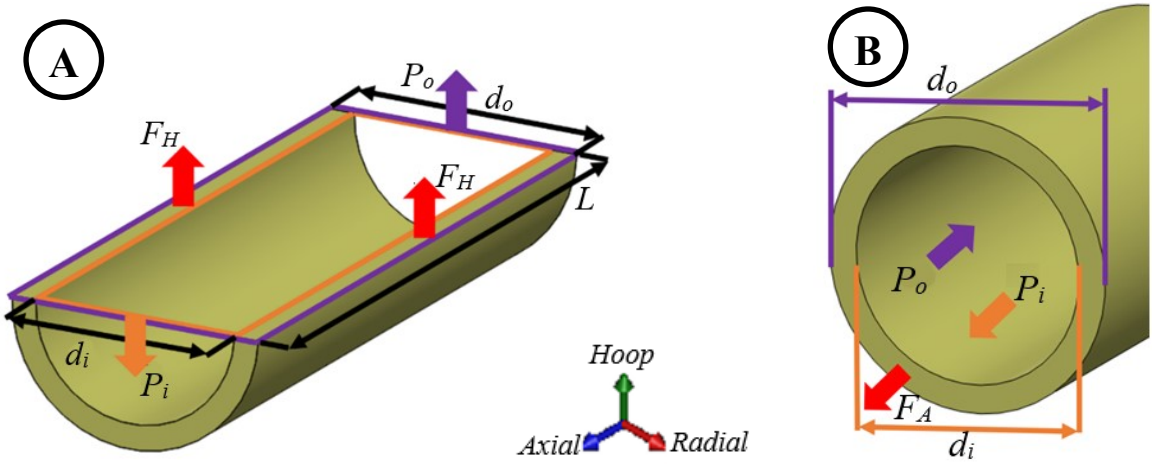

Figure 24: (a) FBD of hoop direction and (b) FBD of axial direction

$$F = \frac{P}{A} \tag{13}$$

$$\sum F_{hoop} \quad -P_i d_i L + P_o d_o L + 2F_H = 0$$
$$\Leftrightarrow 2F_H = P_i d_i L - P_o d_o L \tag{14}$$

$$\sigma_{hoop} = \frac{P_i d_i - P_o d_o}{d_o - d_i} \tag{15}$$

$$\sum F_{axial} \quad \frac{P_i \pi d_i^2}{4} - \frac{P_o \pi d_o^2}{4} + F_A = 0$$

$$\tag{16}$$

$$\Leftrightarrow -F_A = \frac{1}{4}(P_i \pi d_i^2 - P_o \pi d_o^2)$$

$$\sigma_{axial} = \frac{(P_i \pi d_i^2 - P_o \pi d_o^2)}{\pi(d_o^2 - d_i^2)} - F_A \frac{4}{\pi(d_o^2 - d_i^2)} \quad (17)$$

The creep tests had a 10 second ramp up period. Based on the derivation of the creep models, a step stress equal to the test load should be applied [59] but this is physically not possible. A ramp up period of 10 seconds was used because this duration has been considered acceptable to previous researchers [89] and it does not cause failure of the test equipment or specimen. The creep test is three orders of magnitude longer than the ramp up period; therefore, although the ramp up period is not instantaneous, it is considered to have minimal effect on the results.

4.2 Specimen preparation

Test specimen preparation is a multi-step process that involves drawing strain gauge location lines, bonding the end fittings, applying the strain gauge and painting the speckle pattern for DIC.

4.2.1 Strain Gauge Location Lines

The strain gauge was placed in the middle of the specimen and aligned axially along the specimen's axis. The selected orientation and location allows for simultaneous measurement of hoop and axial strains while minimizing effects from end fittings. Straight lines need to be drawn on the specimen to aid in strain gauge placement. Misalignment of the strain gauge will result in measurement errors [90]. A straight line was drawn on the tube using the assembly shown in Figure 25. The assembly is made using a right-angle straight edge held by a vise grip. A magnetic level is attached to the straight edge to ensure it is vertical. The tube is held against the straight edge and a pencil is used to mark a straight line down the surface. The location of the line on the tube determined the placement of the strain gauge; therefore, the line was drawn on an area where the surface was smooth without surface imperfections. A measuring tape was used to measure the middle of the tube and draw a straight line as seen in Figure 26.

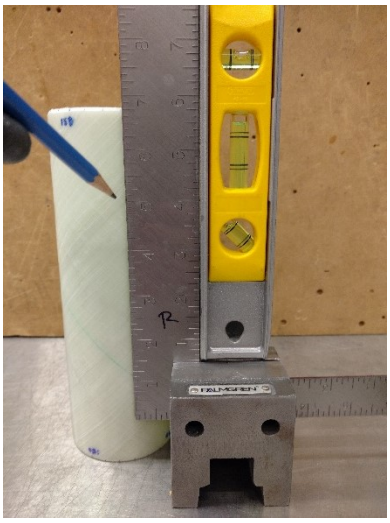

Figure 25: Assembly for drawing strain gauge location line

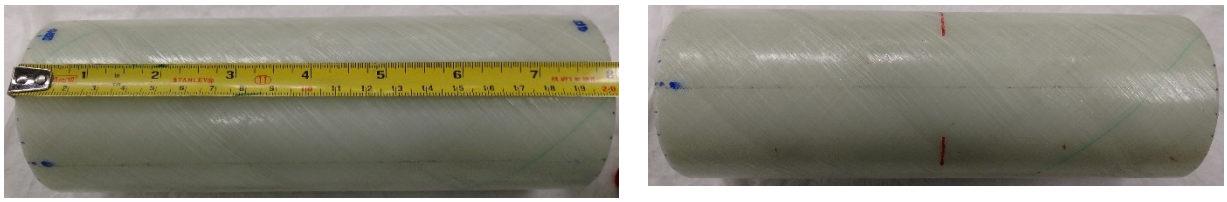

Figure 26: Drawing the strain gauge location line (hoop direction)

4.2.2 End Fittings

Mild-steel end fittings were used to secure the tubular specimen into the testing machine. The fitting were adhesively bonded to a tubular specimen and consist of a pair of inner sleeves and outer flanges as shown in Figure 27. The specimen bonds to the outer and inner cylindrical faces of the inner sleeve and outer flange, respectively. The parts were machined to allow a consistent adhesive layer thickness of 0.5 mm to 1.0 mm; this adhesive bond thickness was demonstrated to be effective in bonding FRPC tubes [91] with epoxy adhesive (DP460, 3M, Maplewood, MN, United States). Due to the difficulty of bonding to HDPE, the surface of the tube had to be cleaned and flame treated [92] to promote bonding to the end fitting assembly. The procedure for bonding the end fittings is described in Appendix A.

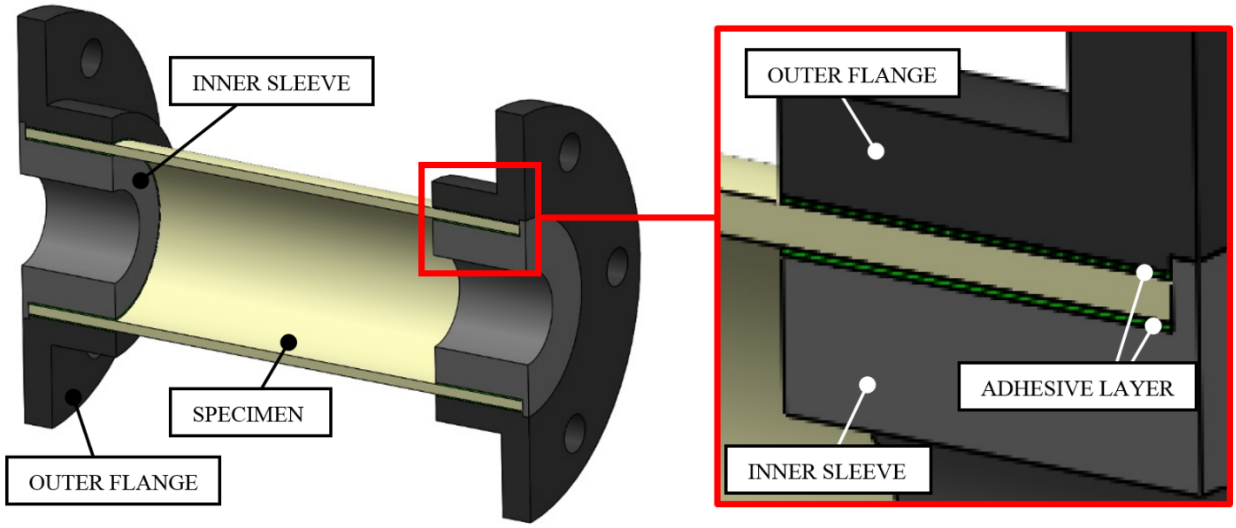

Figure 27: Cut-sectional view of test end fittings

4.2.3 Preparing Specimen for Strain Measurements

The strain gauge application process followed the manufacturer's guidelines [93, 94] with minor modifications to account for a different adhesive, ambient temperature and humidity level. The procedure for applying and soldering the strain gauge is described in Appendix B. The speckle pattern, required for the DIC software to track the motion of the specimen, was applied using the procedure described in Appendix C. The quality of the speckle pattern was confirmed prior to testing. A pattern was considered to be acceptable if the projection error between the two cameras of the DIC system were within acceptable limits. Common error values are between 0.02 and 0.05 [95]. Once the quality of the speckle pattern was verified, the specimen was ready to be installed into the testing machine. Appendix D describes the method used to setup the camera system, calibrate the DIC system and confirm the speckle pattern quality.

4.3 Setting Up the Test Equipment

The test setup involved the following steps:

1) Installing the specimen into the testing machine
2) Filling the pressure intensifier
3) Adjusting the microcontroller
4) Calibrating the strain gauge system
5) Preparing test program and DIC measurement

The above steps are described in Appendix E. Additionally, the method used to remove the end fittings from the tubular coupon after the test is described in Appendix F.

5.0 Results and Discussions

5.1 Summary of Prototyping Trials

The final prototyping setup as described in Section 4.4 was developed over a number of winding sessions and modifications to the equipment were required. Initially a metal mandrel was used without a liner but the mandrel acted as a heat sink and removed heat from the placed tape. Preheating the mandrel in the oven prior to the winding session was a concept used to alleviate this issue. The proposed solution was not effective since, without a sustained heat input for the mandrel, it cooled down quickly. A solid compaction roller with no air heating was used but it was found the roller became too hot and caused the tape material to adhere to the roller. Once the desired manufacturing parameter and sample quality was achieved, two batches of samples were fabricated for creep testing.

5.2 Characteristics of Pipe Samples

5.2.1 Dimensional Measurements

The dimensions of the tubular specimens were measured using a digital caliper. The wall thickness (WT) and inner diameter (ID) on both ends of the tube were measured at 15° intervals along the circumference. Figure 28 and Figure 29 shows the variation in inner diameter and wall thickness, respectively, for the first specimen in Batch #1. The plots of inner diameter and wall thickness for the other specimens are included in Appendix G. The average ID of the tubes from Batch #1 is 61.81 mm with standard deviation of 0.06 mm; average ID for Batch #2 is 61.88 mm with standard deviation of 0.05 mm. The average WT of the tubes from Batch #1 is 3.65 mm with standard deviation of 0.03 mm; average WT for Batch #2 is 3.61 mm with standard deviation of 0.03 mm. Based on a two-mean, unequal variance t-test, the average ID and WT from Batch #1 and Batch #2 can be considered the same within a 95% confidence interval. The consistent ID dimensions between batches can be attributed to winding the tape material over a commercially manufactured tube liner with standard OD. The consistent wall thickness can be explained by the application of a compaction roller to smooth out uneven surfaces. The thickness of the 10-layer tube (approximately 3.6 mm) is thicker than the expected thickness for 10 layers

of unprocessed tape (3.30 mm). This occurrence could be caused by the variation in tape thickness introduced during manufacturing of the unconsolidated tape or lateral compaction of the tape during the tape winding process. The tape was placed on the mandrel in the 'lag' pattern which means the tape from subsequent passes slides against previously laid tape. Lateral compaction causing increased thickness of final product dimensions has been observed in other tape placement applications [96, 97].

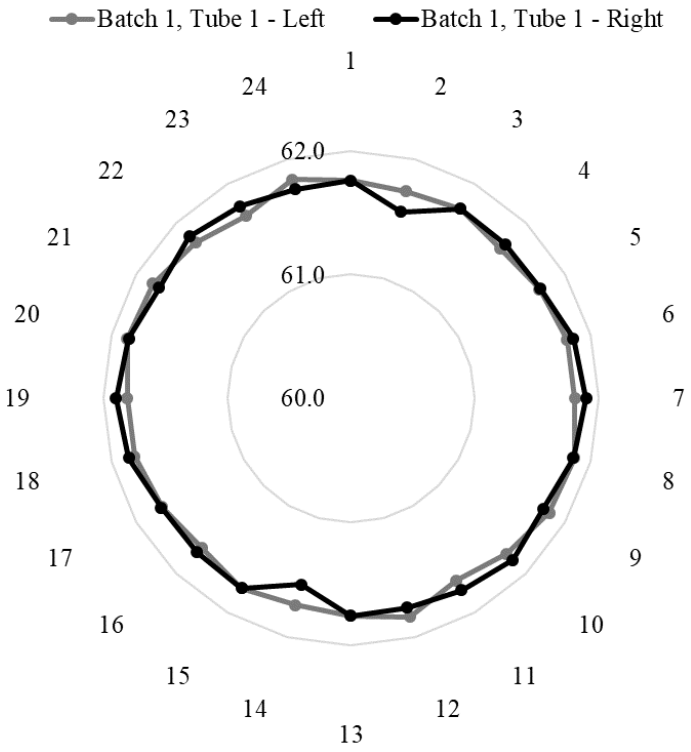

Figure 28: Variation in inner diameter (in mm)

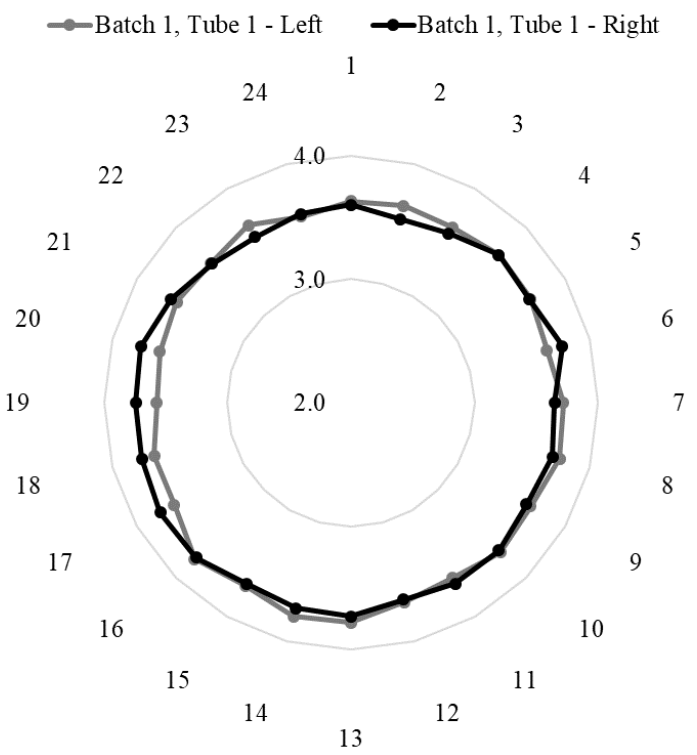

Figure 29: Variation in wall thickness (in mm)

The wall-thickness-to-inner-diameter ratio, averaged over both batches, is 0.058, which is slightly higher than the commonly accepted value of 0.05 for the thin wall assumption to be valid. However, there are varying views on the threshold for validity of the thin wall assumption [88]. Another theory considers thin-wall assumption to be valid if the outer-diameter-to-inner-diameter (OD/ID) ratio is less than 1.16 [88]. The average OD/ID ratio for all specimens is 1.12. Calculating the required loading conditions to obtain the desired stresses in the specimens using thick-wall cylinder equations would be more accurate since in reality the radial stresses are non-zero and the hoop stresses do vary through the thickness of the pipe while the thin-wall assumption requires the opposite. Lame's Theorem [98] provides analytical equations for calculating the stresses in thick-walled cylinders but assumes the material is isotropic and homogenous which is not applicable in this study. Equations developed for thick-walled composite pipes are much more complex [99] and is considered outside the scope of this thesis. Considering that an OD/ID ratio of 1.12 is considered by some researchers to be valid for thin-wall assumption, the tests were conducted using the equations derived in Section 5.5.1. It is considered the thin-wall equations will provide a simplified approximation to actual conditions.

5.2.2 Microstructure

Scanning electron microscopy was used to study the microstructure of the consolidated parts from both batches. Samples were cut to allow straight on viewing of the fibre cross-sections. The SEM samples were encased in a 25.4 mm (1") diameter epoxy puck. The puck was wet ground using silicon carbide paper with progressively rougher grit grades (180, 320, 600, 800 and 1200 grit). The epoxy puck was then polished with a 1µm diamond slurry. The puck was carbon coated to produce a conductive surface which reduces electron charge affecting the image. The SEM was set to back-scattered electron mode at 70x magnification.

Figure 30 are representative samples of a part microstructure for Batch #1 and #2. The fibres, matrix and encasing epoxy structure appear as the white, dark grey and light grey areas, respectively. All ten layers of tape fibres are visible with matrix-dominant and fibre-dominant regions interspersed throughout the structure. In certain areas, the tape layers blend together which resembles the microstructure observed by Mazumdar and Hoa [50]. The blending could be the result of the high processing temperatures and compaction pressure causing the melted HDPE to be pushed out towards the edges as the tape layers are placed. The fibre layers of the Batch #2 sample are more closely compacted; this could be a result of the higher processing temperatures allowing greater flow of the HDPE.

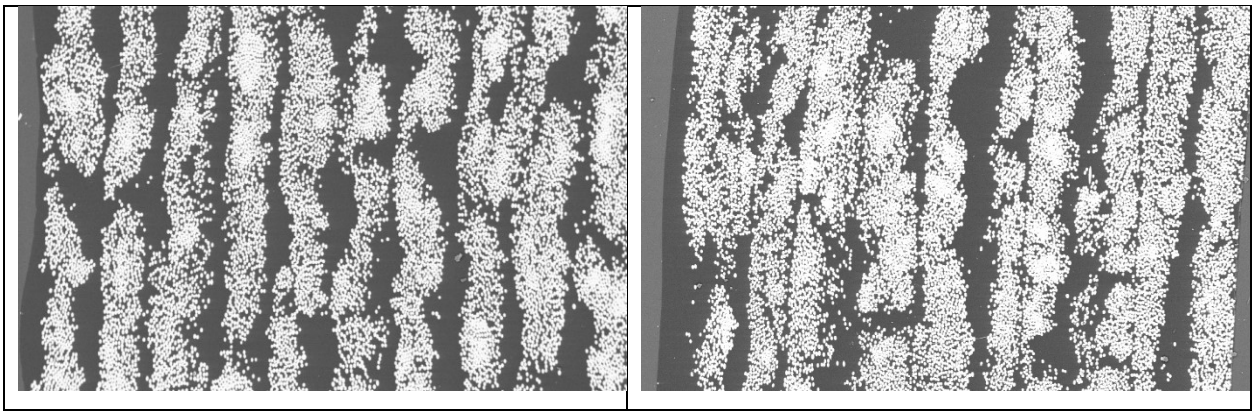

Figure 30: Microstructure of consolidated specimen from batch #1 (left) and batch #2 (right)

The weight fraction of the fibre in the GFR-HDPE tape was 60.4 % as determined by fibre burnout tests. Therefore, the fibre volume fraction of the tape was calculated to be 38.6% using Equation (18) where m_c and m_f are the mass of the composite and fibres, respectively. Their

densities are denoted by ρ_c and ρ_f, respectively. The fibre volume fractions is denoted by V_f. The density of the GFR-HDPE tape, 1.56 g/cm^3, was provided by the manufacturer while the density of the fibre-glass, 2.44 g/cm^3, was found in an online material database [100].

$$V_f = \frac{m_c/\rho_c}{m_f/\rho_f} \tag{18}$$

Image analysis software (ImageJ, Wayne Rasband, NIH, Maryland, United States) was used to compare the fibre volume fraction of the consolidated part to the unprocessed tape. Three SEM images from each batch were used to determine the fibre area fraction. The fibre area fraction can be used to approximate the fibre volume fraction assuming the cross section shown in Figure 30 is representative of the entire specimen's microstructure. The image was cropped to remove areas of the epoxy surrounding the specimen and then converted into an 8-bit binary image. The area ratio of black to white in the image was calculated using ImageJ. The area fraction, which is equivalent to the fibre volume fraction, in the consolidated part for Batch #1 and Batch #2 are 43.3% and 43.5%, respectively. The tape winding process increased the fibre volume fraction of the part which agrees with the observation of liquid HDPE being squeezed out as the tape was consolidated. This image analysis process does not take into account voids in the matrix region; therefore the void content of the specimen was analyzed in a separate step.

To calculate the void space content in the specimens, the same six SEM images were modified from the original as demonstrated in Figure 31(a). The fibre areas were coloured black using image editor software (Paint.net, dotPDN LLC) leaving the matrix regions and suspected void spaces to appear as dark and light grey areas, respectively. The image threshold was adjusted in ImageJ until the suspected void space areas were highlighted in green as shown in Figure 31(b). In some cases, the highlighted green areas could be contamination introduced by grinding performed during SEM sample preparation. Overall, the average suspected void content was 0.18% and 0.41% for Batch #1 and Batch #2, respectively. The microstructure of the unprocessed tape was not studied; therefore, it is unclear if the voids were already present in the tape or introduced by the tape winding process. One possible reason for the higher void content observed in Batch #2 is the higher processing temperature. Pockets of moisture within polymers are one cause of void spaces. Formation of void space due to moisture begins at the melting

temperature for semi-crystalline polymers [101], such as HDPE. As the polymer is heated, moisture escapes but the quicker the material reaches melting temperature, the less time for moisture to escape. The higher heat setting used in the second winding session could cause the GFR-HDPE tape to reach melting temperature quicker and possibly retain more moisture. The void content observed in the present study is even lower than the void content of approximately 1.5% achieved by Agarwal [48]. The relatively low void fraction observed in this study could be attributed to the low relative humidity (approximately 11%) environment in which the tape was stored; another reason could be the high compaction force used to consolidate the tape layers.

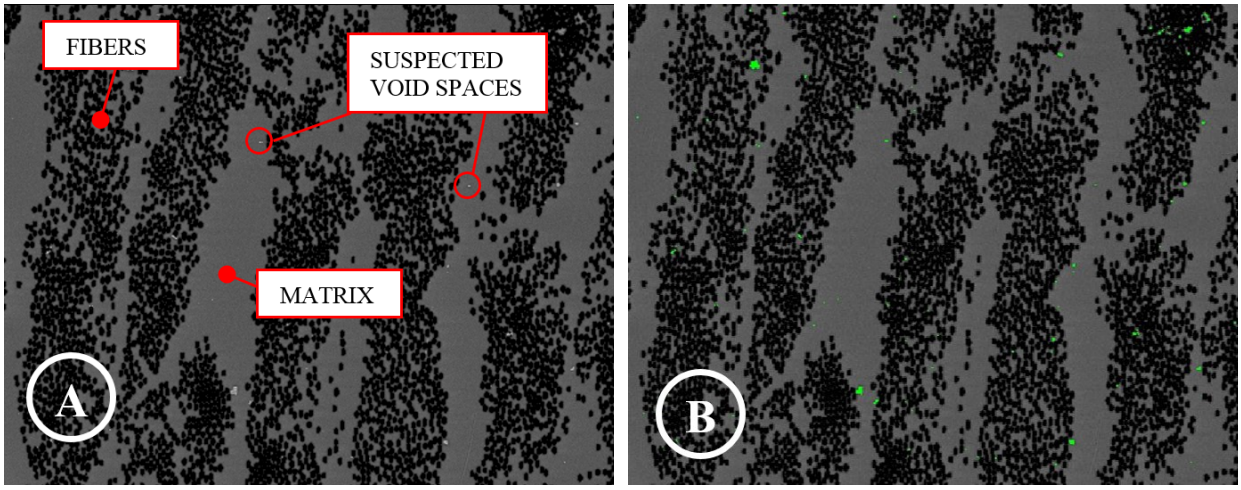

Figure 31: (a) Modified image to calculate void spaces and (b) green areas of suspected void spaces

5.2.3 Bond Quality

The bond quality of consolidated tubes was verified by crushing the rings cut from the tube in a vise as shown in Figure 32. The rings were crushed in one direction and then rotated 90° to be crushed a second time. Localized delamination, circled in red as seen in Figure 32, was observed in several ring samples. The amount of delamination was considered to be minimal since the rings experienced much greater deformation during the crush test than what is expected in the actual creep test. Tubular samples adjacent to the rings experiencing localized delamination was record but all specimens were considered suitable for testing. Quantitative measurements of bond strength were not considered necessary since producing prototypes with good bonding to be used for creep testing was the main goal. Future work could involve strength

testing of the tubes based on the ASTM D2344 test standard [49] as was conducted by previous researchers [40, 41, 48].

Figure 32: Crush test to check bond quality

5.3 Detailed Testing Parameters

Table 4 summarizes the test conditions for each specimen. The tests under 10 MPa pure hoop stress were conducted first and then the same specimen were subjected to 5 MPa pure axial stress for the axial compression tests. After the pure hoop tests were complete and the pressure intensifier was ramped down, the specimen supply valve was closed to isolate the specimen from the intensifier. The specimen was allowed to rest overnight in the testing machine. In all tests the desired torsional load was set to zero; however, due to fluctuations in the actuating equipment or sensor readings, the torsional load was non-zero and fluctuating. The torsional load was always under 0.3 Nm (2 in-lb) which is considered negligible compared to the internal pressure and axial loadings. Different test durations were conducted: short-term (approximately 2 hours), intermediate (4 hours) and longer term (6 and 7 hours). Figure 33 demonstrates the typical internal pressure and axial loadings for the creep tests; the loading conditions were stable and deviation from the set test levels was under 10%.

Table 4: Test matrix for creep experiments*

Test Name	Specimen ID	Wall Thickness	Internal Pressure	Axial Force
	(mm)	(mm)	(MPa)	(N)
H004	61.92	3.64	1.176	-3829
H004b	61.92	3.64	N/A	-3829
H005	69.14	3.65	1.158	-3548
H005b	69.14	3.65	N/A	-3757
H006	69.14	3.59	1.158	-3487
H009	61.89	3.65	1.181	-3553
H009b	61.89	3.65	N/A	-3762
H010	69.02	3.60	1.165	-3495
H010b	69.02	3.60	N/A	-3495

*Tests H001 and H002 were burst tests conducted using different tape material for another study. Results from H003 were not reported because the strain gauge was damaged during installation. Tests H007 and H008 were not creep tests but were used to troubleshoot equipment issues.

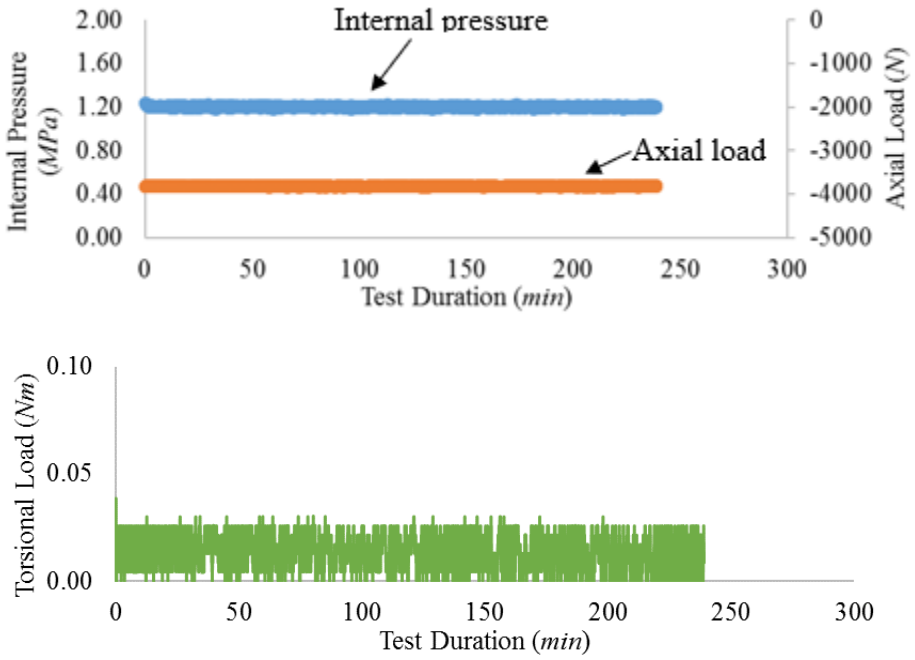

Figure 33: Typical internal pressure, axial and torsional loading for creep tests

5.4 Pure Hoop Creep Test Results

5.4.1 Comparing Initial Elastic Strain to Classical Lamination Theory

In addition to comparing strains determined by DIC and strain gauge measurements, the initial elastic strain was predicted using Classical Lamination Theory (CLT). The theory can be used to calculate the stresses and strains in laminates, a flat structure made of two or more layers of composite material, and has the following assumptions [19]:

- Each layer is homogenous, elastic and orthotropic
- "A line straight and perpendicular to the middle surface remains straight and perpendicular to the middle surface during deformation"
- "Displacements are continuous and small" compared to the thickness of the whole structure
- There is perfect bonding between the layers
- The structure experiences plane stress condition since it is a thin structure

CLT can be used to design laminated plates and thin-wall pressure vessels [19]. A tube is considered to be similar in structure to a pressure vessel; therefore, CLT was used in this study. In reality, the material is heterogenous, instead of homogenous, and there will be radial stress acting through the wall of the tube but CLT is considered to provide an acceptable approximation. In two-dimensions, the stress-strain relationship is given by Hooke's Law as shown in Equation (19) where E is the Young's modulus. For a three-dimensional material with the assumptions mentioned above, the stress-strain relationship is given by Equation (20) where Q is the reduced stiffness matrix. Calculation of the reduced stiffness requires four engineering constants: Young's modulus in fibre direction (longitudinal modulus, E_1) and perpendicular to fibre direction (transverse modulus, E_2), major Poisson ratio (ν_{12}) and in-plane shear modulus (G_{12}). The minor Poisson ratio, ν_{21}, is related to the major Poisson ratio through Equation (21). The terms of the reduced stiffness matrix are calculated using Equation (22) to Equation (25). The required material properties of the GFR-HDPE tape were not provided by the manufacturer;

therefore, they were approximated using the “rule of mixtures” (ROM) and semi-empirical models.

$$\sigma = E\varepsilon \tag{19}$$

$$\sigma = [Q]\varepsilon = \begin{bmatrix} Q_{11} & Q_{12} & 0 \\ Q_{12} & Q_{22} & 0 \\ 0 & 0 & Q_{66} \end{bmatrix} \varepsilon \tag{20}$$

$$\frac{v_{12}}{E_1} = \frac{v_{21}}{E_2} \tag{21}$$

$$Q_{11} = \frac{E_1}{1 - v_{12}v_{21}} \tag{22}$$

$$Q_{22} = \frac{E_2}{1 - v_{12}v_{21}} \tag{23}$$

$$Q_{12} = \frac{v_{21}E_1}{1 - v_{12}v_{21}} \tag{24}$$

$$Q_{66} = G_{12} \tag{25}$$

In addition to assuming the fibres and matrix move together and experience the same amount of strain, ROM requires the following assumptions [19]:

- The fibres and matrix are perfectly consolidated
- “The fibres are continuous” and all oriented in the same direction
- All fibres are the same size and have the same properties with equal spacing between them
- There are no void spaces within the material
- The behaviour of the fibres and matrix are governed by Hooke’s Law

The matrix modulus, E_m, and fibre modulus, E_f, contribute to the longitudinal modulus of the composite based on their volume fraction (V_m amd V_f, respectively) within the composite. Similarly, the composite's major Poisson ratio depends on the Poisson ratio of the matrix (v_m) and the fibre (v_f) and their volume fraction. Equation (26) and Equation (27) were used to calculate E_1 and v_{12}, respectively. The void space content observed in the image analysis of the micrographs were not included in the calculations. The material properties for glass fibre and HDPE used in the calculations are summarized in Table 5; they were obtained from a textbook [19] and online database [100, 102]. The exact Young's modulus of fibre glass and HDPE used in the tape is not known; therefore, maximum and minimum values were used to determine the expected range for initial elastic strain.

$$E_1 = E_f V_f + E_m V_m \tag{26}$$

$$v_{12} = v_f V_f + v_m V_m \tag{27}$$

The rule of mixtures is suitable for calculating E_1 and v_{12}, but E_2 and G_{12} were calculated using semi-empirical models for increased accuracy. Equation (28) was used to calculate the transverse modulus where ξ is the reinforcing factor; it has a value of 2 under the assumption that the fibres are arranged in a square packing arrangement. η is the shape factor and is calculated using Equation (29). Equation (30) was used to calculate G_{12} and its shape factor was calculated using Equation (31). Separately, glass fibre and HDPE are each considered isotropic which allowed the fibre shear modulus, G_f, and matrix shear modulus, G_m, to be calculated using Equation (32).

$$E_2 = \frac{E_m\left(1 + \xi\eta V_f\right)}{1 - \eta V_f} \tag{28}$$

$$\eta = \frac{E_f/E_m - 1}{E_f/E_m + \xi} \tag{29}$$

$$G_{12} = \frac{G_m\left(1 + \xi\eta V_f\right)}{1 - \eta V_f} \tag{30}$$

$$\eta = \frac{G_f/G_m - 1}{G_f/G_m + \xi} \tag{31}$$

$$G = \frac{E}{2(1+v)} \tag{32}$$

Table 5: Material properties for glass fibre and HDPE

Material Properties		Glass Fibre	HDPE
Young's Modulus - Minimum (MPa)		68900	700
Young's Modulus - Maximum (MPa)		85000	1340
Poisson Ratio		0.2	0.46
Volume Fraction		Minimum	Maximum
	Batch #1	0.433	0.567
	Batch #2	0.435	0.565

Equation (22) through Equation (25) do not consider the orientation angle of the fibres. Equation (33) to Equation (38) were used to transform each element of the reduced stiffness matrix based on the winding angle, where *c* and *s* are the cosine and sine (in degrees) of the angle, respectively. Each layer of the tubes has a thickness, *t*, and a height with respect to its midplane, *h*, as shown in Figure 34. The reduced stiffness matrix and height of each layer was used to calculate the [*A*], [*B*] and [*D*] matrices as shown in Equation (39) to Equation (41) . The [*A*] matrix or extensional stiffness matrix allows for calculation of the strains due to in-plane forces (N_x, N_y, N_{xy}). The [*B*] matrix or coupling stiffness matrix is used to calculate the strains (ε^0_x, ε^0_y, γ^0_{xy}) and curvatures (κ_x, κ_y, κ_{xy}) at the midplane due to the applied bending moments and forces, respectively. The [*D*] matrix is the bending stiffness matrix and allows for calculation of the curvature due to bending moments (M_x, M_y, M_{xy}).

$$\bar{Q}_{11} = Q_{11}c^4 + Q_{22}s^4 + 2(Q_{12} + 2Q_{66})s^2c^2 \tag{33}$$

$$\bar{Q}_{12} = (Q_{11} + Q_{22} - 4Q_{66})s^2c^2 + Q_{12}(c^4 + s^4) \tag{34}$$

$$\bar{Q}_{22} = Q_{11}s^4 + Q_{22}c^4 + 2(Q_{12} + 2Q_{66})s^2c^2 \quad (35)$$

$$\bar{Q}_{16} = (Q_{11} - Q_{12} - 2Q_{66})c^3s - (Q_{22} - Q_{12} - 2Q_{66})cs^3 \quad (36)$$

$$\bar{Q}_{26} = (Q_{11} - Q_{12} - 2Q_{66})cs^3 - (Q_{22} - Q_{12} - 2Q_{66})c^3s \quad (37)$$

$$\bar{Q}_{66} = (Q_{11} + Q_{22} - 2Q_{12} - 2Q_{66})c^2s^2 + Q_{66}(c^4 + s^4) \quad (38)$$

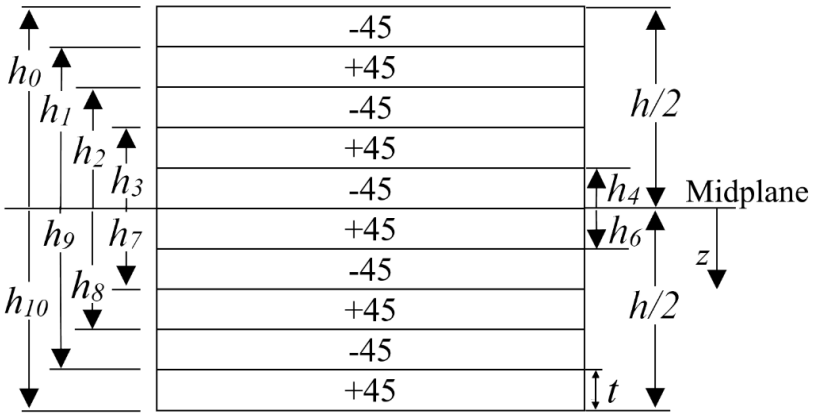

Figure 34: Coordinate system of the specimen (reproduced based on image from [19])

$$A_{ij} = \sum_{k=1}^{10} [\overline{Q_{ij}}](h_k - h_{k-1}) \quad (39)$$

$$B_{ij} = \frac{1}{2}\sum_{k=1}^{10} [\overline{Q_{ij}}](h_k^2 - h_{k-1}^2) \quad (40)$$

$$D_{ij} = \frac{1}{3}\sum_{k=1}^{10} [\overline{Q_{ij}}](h_k^3 - h_{k-1}^3) \quad (41)$$

In this study, it was assumed there were no bending moments, and the in-plane forces were due to the applied test pressures and compressive axial force. The torsional load was controlled by the testing machine and remained close to zero. The internal pressure and axial

force measured by the test system at 10 seconds into the test were used to calculate the hoop and axial stresses according Equation (15) and Equation (17) described in Section 5.1.5. The stresses were converted into forces per unit length by multiplying them by the specimen thickness. Once the in-plane forces and [A], [B] and [D] matrices were known, the midplane strains and curvatures were found using Equation (42). Equation (43) was used to find the strain on the top layer of the composite tube.

$$\begin{bmatrix} N_x \\ N_y \\ N_{xy} \\ M_x \\ M_y \\ M_{xy} \end{bmatrix} = \begin{bmatrix} [A] & [B] \\ [B] & [D] \end{bmatrix} \begin{bmatrix} \varepsilon_x^0 \\ \varepsilon_y^0 \\ \gamma_{xy}^0 \\ \mathrm{K}_x \\ \mathrm{K}_y \\ \mathrm{K}_{xy} \end{bmatrix} \tag{42}$$

$$\begin{Bmatrix} \varepsilon_x \\ \varepsilon_y \\ \varepsilon_z \end{Bmatrix} = \begin{Bmatrix} \varepsilon_x^0 \\ \varepsilon_y^0 \\ \varepsilon_z^0 \end{Bmatrix} + h \begin{Bmatrix} \mathrm{K}_x \\ \mathrm{K}_y \\ \mathrm{K}_z \end{Bmatrix} \tag{43}$$

The initial elastic strain and final creep strain values for the pure hoop creep tests are shown in Figure 35. A log-time scale was chosen to better display the initial strain experienced by the specimens. Due to an operator error, excitation voltage was not being sent to the strain gauge for approximately the first 30 seconds of the H006 test; therefore the observed strain is zero during this period. This occurrence demonstrates the importance of an additional measurement method, such as DIC, to serve as a backup in case the primary measurement method experiences issues. It also demonstrates an advantage of real-time data acquisition versus methods that require post-processing, such as DIC, because attempts can be made to rectify observed issues during the test. In post-processing methods, any issues with the strain measurements would not be known until after the test is over and the data is being analyzed. Test H005 did not ramp up to test loading conditions within 10 seconds; the cause for this occurrence is unclear but it is possible that there was still air within the specimen which resulted in pressurization issues.

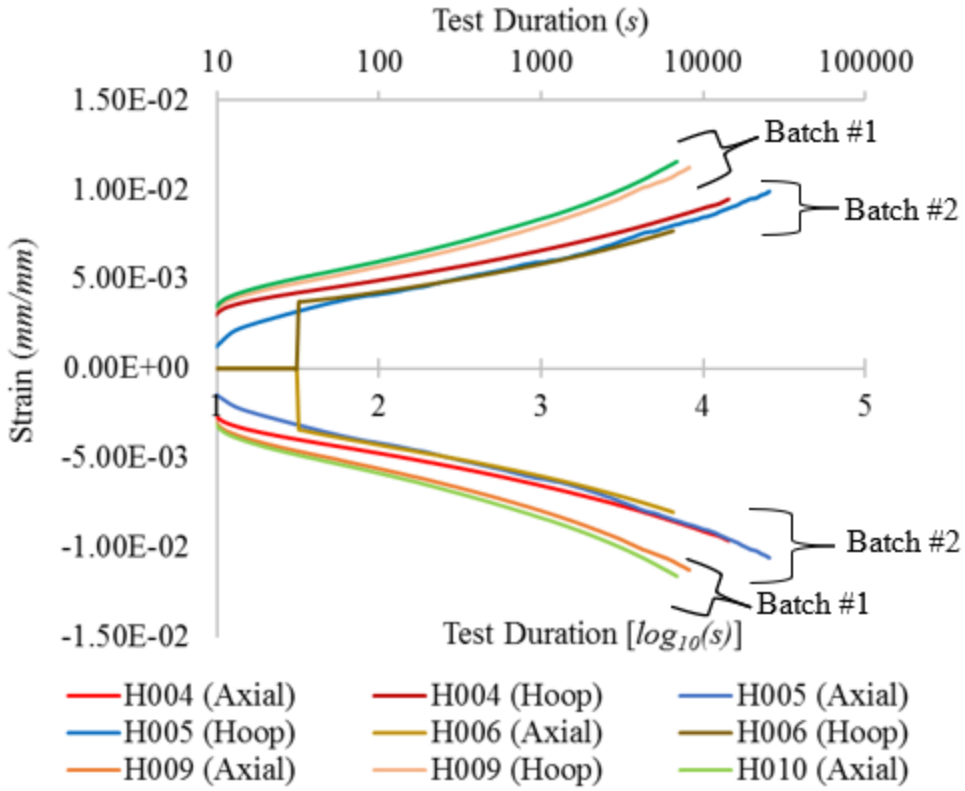

Figure 35: Strains experienced during pure hoop creep tests (H004 to H006 are specimens from Batch #2, H009 and H010 are specimens from Batch #1)

Specimens from Batch #1 (H009 and H010) experienced higher levels of initial elastic strain and final creep strain than those from Batch #2 (H004, H005, and H006). The dimensions, fibre volume fraction and void space content of the two batch of specimens are similar; however, the difference in strain could be explained by differences in crystallinity. Agarwal [48], as well as, Mazumdar and Hoa [50] attributed changes in the crystallinity of the composite structure to the annealing experienced by the tape as it is heated and reheated during the winding process. Agarwal observed higher heat input during winding of CFR-PEEK tape resulted in a higher percentage of crystallinity in the finished product. PEEK and HDPE are both semi-crystalline thermoplastic polymers. Additionally, it has been demonstrated that different cooling rates of liquid HDPE have resulted in different crystalline structures [103]. In this study, the GFR-HDPE tape received different heat inputs during the two winding sessions and was allowed to cool to room temperature. It is plausible to conclude this process resulted in different degrees of crystallization in the finished product. A greater level of crystallinity corresponds to a greater

number of secondary valence bonds between molecules [56] which explains the greater resistance to creep [73]. Differential scanning calorimetry tests were not conducted to verify the crystallinity of the specimens since this was not considered to be within scope of the project; however, differential scanning calorimetry tests could be conducted on specimens as part of future work.

Specimens within the same batch experienced similar levels of strain. Final strain values were different because test durations were not the same for all specimens; therefore, a reference time of 100 minutes was used to compare the creep strain experienced. At 100 minutes, the axial strain and hoop strain measured for specimens H004, H005 and H006 were within 7% and 10% of each other, respectively. The measured axial and hoop strain for H009 and H010 were both within 7% of each other. It can be concluded that repeatable creep strain values were observed for each batch.

Table 6 displays the calculated stresses and strains, as well as, the measured initial strains at 10 seconds for each test. Ten seconds was chosen as a reference point because it is the start of the hold stage of the creep test and the loading condition should be stable. The hoop and axial stresses were calculated using the equations derived from the thin-wall assumption mentioned in Section 5.1.5. The axial stress on each specimen is non-zero, therefore, the test is not under pure hoop loading; however, the axial stresses are much less than the hoop stresses so can be considered to be approximately under pure hoop loading condition. H006 was excluded from the calculations since the strain readings were not available at 10 seconds into the test. The measured strains, except for H005, were within the predicted range of strain values based on the maximum and minimum material properties shown in Table 5. A possible explanation for the discrepancy between theoretical and measured strain for H005 is due to the abnormal ramp up condition. The delayed ramp up period suggests additional forces were acting on the specimen which caused deviation from the expected strain values. Despite the approximations and assumptions of the thin-wall assumption and the CLT, there was good agreement between calculated and measured strain values for most of the tests; this provides confidence in the accuracy of the strain gauge readings.

Table 6: Comparison of measured and calculated initial strains

Test Number	H004	H005	H009	H010
Calculated Axial Stress (MPa)	-0.17	-2.47	0.21	0.22
Calculated Hoop Stress (MPa)	10.47	4.73	10.41	10.39
Max. Calculated Axial Strain (mm/mm)	-4.55E-03	-3.19E-03	-4.29E-03	-4.28E-03
Min. Calculated Axial Strain (mm/mm)	-2.31E-03	-1.67E-03	-2.19E-03	-2.19E-03
Measured Axial Strain (mm/mm)	-2.73E-03	-1.49E-03	-3.11E-03	-3.23E-03
Max. Calculated Hoop Strain (mm/mm)	5.06E-03	3.32E-03	5.10E-03	4.91E-03
Min. Calculated Hoop Strain (mm/mm)	2.77E-03	1.77E-03	2.67E-03	2.67E-03
Measured Hoop Strain (mm/mm)	3.10E-3	1.28E-03	3.39E-03	3.53E-03

5.4.2 Comparison of Strain Gauge and DIC Measurements

The use of the DIC technique allows strain measurement in multiple areas of varying sizes while the strain gauge only measures strain on the surface area it is bonded to. For this study, two areas of interest were selected for DIC analysis. An area covering the strain gauge area was selected to allow comparison of the strain gauge measurements as shown in Figure 36(a). This area viewed within the analysis software, Vic-3D, is 150 pixels wide and 70 pixels tall. Measurements from this area will be referred for the remainder of the thesis as DIC-A. The second area called DIC-B was selected to be 10 pixels below area DIC-A and is 150 pixels wide and 210 pixels tall. Area DIC-B is shown in Figure 36(b). DIC-B was chosen to be in the middle of the specimen to minimize any effects caused by the end fittings. The strain gauge measures a limited area of the specimen and can be affected by adhesive bondline thickness or irregularities in the tube at the strain gauge location so DIC-B will be used to verify if the strain gauge measurements are representative of the rest of the specimen.

Figure 37 and Figure 38 show a sample of the strain contour maps for DIC-A and DIC-B, respectively. According to the DIC software coordinate system, DIC-A measures an area of approximately 6mm in height and 15 mm in length while DIC-B measures an area approximately 24 mm in height and 15 mm in length. DIC provides a visual representation of the strain fields on the surface of the specimen while the strain gauge only provides a numerical value. The strain contour map is not uniform and a moiré pattern is observed; this could be the result of the non-ideal speckle pattern, which will be discussed in more detail in Section 6.6.

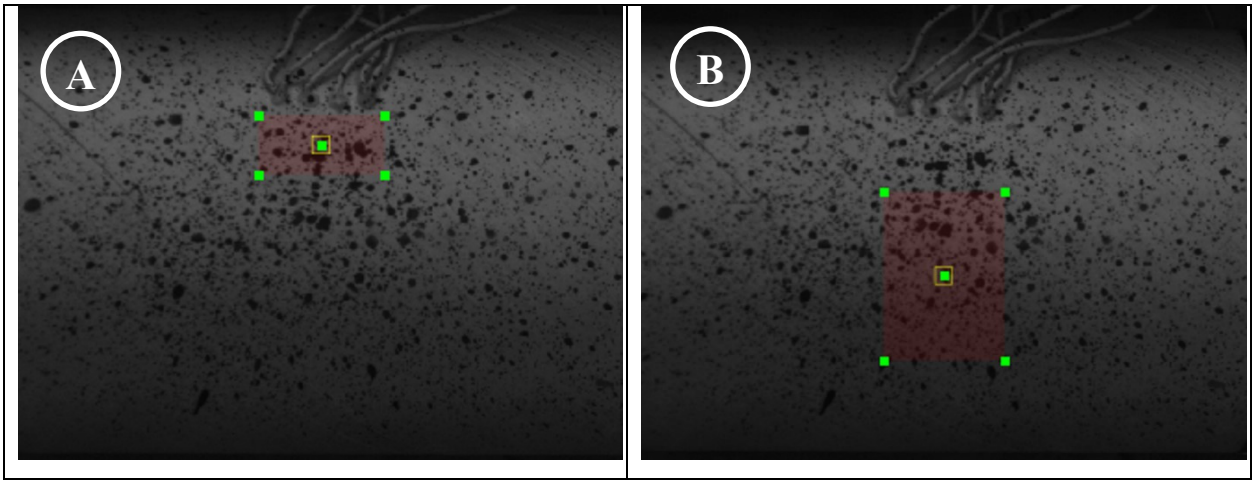

Figure 36: Areas of interest for DIC analysis (a) DIC-A; (b) DIC-B

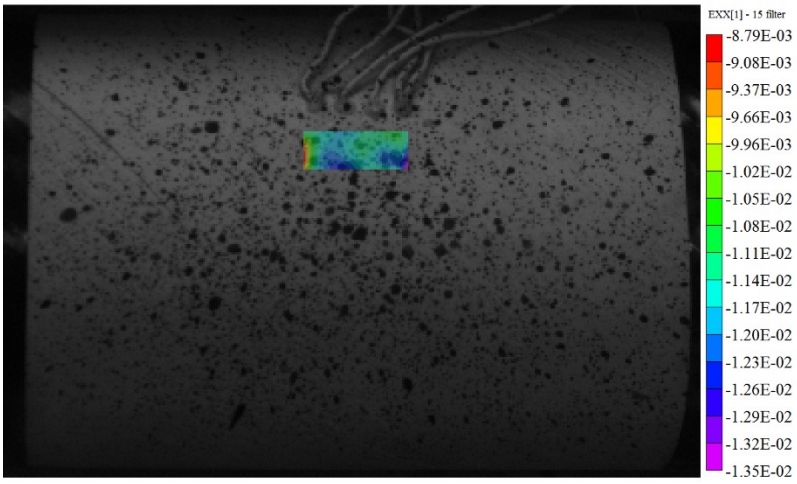

Figure 37: Strain contour map for DIC-A

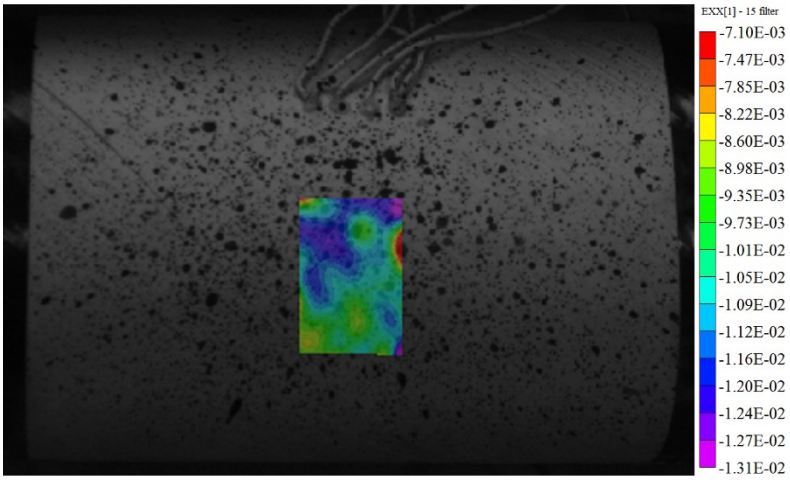

Figure 38: Strain contour map for DIC-B

Table 7 compares the measurements obtained from DIC and the strain gauges. The DIC data was noisy; therefore, certain points were above and some were below the strain gauge measurements. To account for the noisy data, the absolute average of the percent difference between DIC and SG readings was taken. In most cases the DIC-A and strain gauge measurements are in good agreement despite the moiré pattern which demonstrates the DIC technique can be used to verify SG measurement. The results provide added confidence in the strain gauge readings.

In most cases, the axial strain values for DIC-B were in close agreement with the SG values; however, the hoop strain values show greater deviation. In general, the axial strains measured by DIC tend to have less discrepancy with the strain gauge measurements than hoop strains. There is a possibility that misalignment of the strain gauge is the source of the error, but three checks were performed during the specimen preparation process to ensure its proper alignment. Even slight misalignment of the SG would introduce a similar error in the axial strain but hoop strain deviation is consistently higher which suggests the source of error is due to the DIC system. Potential causes for this discrepancy will be discussed in more detail in Section 6.6.

Table 7: Absolute percent difference compared to strain gauge data (averaged)

Test Name	DIC-A		DIC-B	
	Axial	**Hoop**	**Axial**	**Hoop**
H004	6%	6%	8%	34%
H005	2%	22%	1%	19%
H006*	1%	13%	8%	63%
H009	2%	8%	4%	3%
H010	5%	8%	1%	19%
H004b	4%	16%	8%	24%
H005b	14%	37%	7%	29%
H010b	8%	47%	11%	44%

*The data points in which there was no excitation voltage were excluded from the average

Figure 39 and Figure 40 provide the strain versus time curve for one specimen from each batch; the strain measured by both DIC and SG are displayed. First stage and second stage creep are observed; none of the specimens experienced tertiary creep due to the low loading conditions. In comparison, at room temperature, various grades of HDPE subjected to 10 MPa tensile stress experienced over 0.02 mm/mm strain at the one hour mark of the creep test [87]; this demonstrates the significant improvement in creep resistance the reinforced composite has in comparison to the pure polymer.

Measurements from DIC-A tends to have more noise than DIC-B; this could be due to the smaller area of DIC-A, which means the software has less data points to smooth out the data and filter out noise [84]. The profile of the creep curves captured by DIC and SG are similar but the DIC hoop strain data tends to be noisier than its axial strain data. Additionally, the DIC system tends to measure a higher hoop strain compared to the strain gauges. Graphs for the other tests will be shown and discussed in more detail in Section 6.6, where possible reasons for the discrepancy between DIC and SG are discussed. Overall, it demonstrates that a DIC setup and procedure has been developed that is capable of obtaining good agreement with the SG readings.

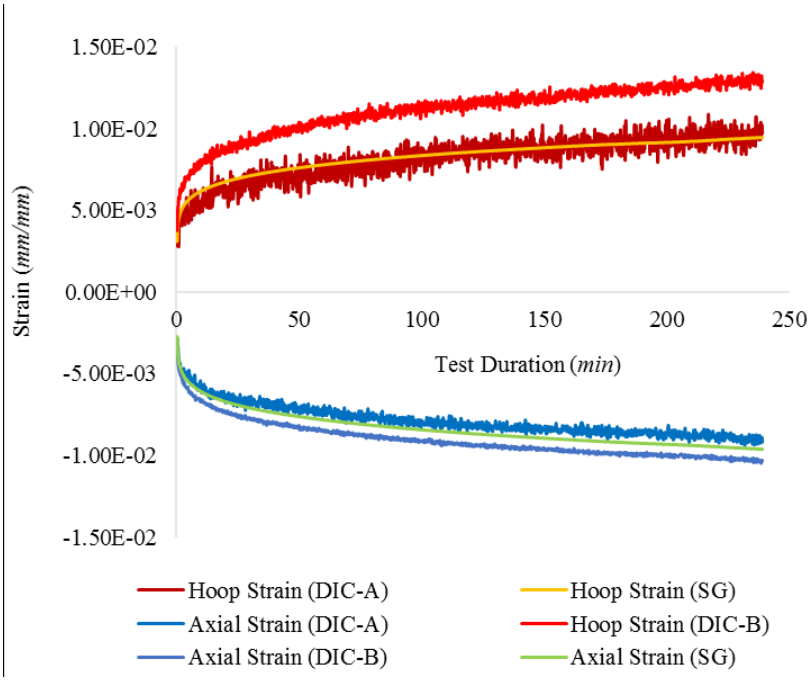

Figure 39: H004 test results

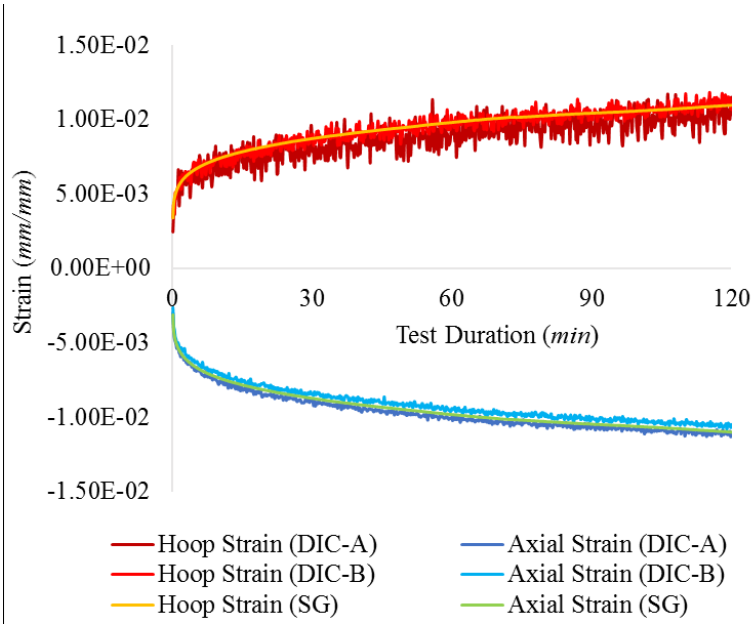

Figure 40: H009 test results

5.4.3 Poisson Ratio

The long-term effect of bi-axial loads on the Poisson ratio for the tubular specimens was investigated. Poisson ratio is defined as the negative of the ratio between strain perpendicular to the applied loading direction over the strain in the applied loading direction. Poisson ratio, ν, can

be calculated using Equation (44) where ε_{hoop} and ε_{axial} are the hoop and axial strain, respectively. The Poisson ratio can be calculated from the CLT [19] and is given by Equation (45) where ν_{xy} is the major Poisson ratio; A^*_{12} and A^*_{11} are the terms from the inverse of the extensional stiffness matrix [A]. The derivation of this equation assumes the laminate is symmetric, the coupling stiffness matrix, [B], is zero and force is applied in only one direction. In reality, the [B] matrix is not zero but bending moments are considered negligible compared to the internal pressure and axial forces and will not have a large effect on strains.

$$\nu = -\frac{\varepsilon_{hoop}}{\varepsilon_{axial}} \tag{44}$$

$$\nu_{xy} = -\frac{A^*_{12}}{A^*_{11}} \tag{45}$$

The calculated Poisson ratios and DIC results were compared to the SG measurements. The Poisson ratio calculated from CLT ranges from 0.83 to 0.88, corresponding to higher and lower Young's modulus for both the GF and HDPE, respectively. The small difference in fibre volume fraction between Batch #1 and Batch #2 meant their calculated Poisson ratio agreed up to the third decimal place. The Poisson ratio for isotropic materials has an upper limit of 0.5; however, this restriction does not apply to anisotropic materials [104]. The log-time scale graph in Figure 41 shows the Poisson ratio based on the axial and hoop strain data captured by the strain gauges. The graph only displays the data starting at the point when each test reached the hold pressure and axial loading conditions. During the ramp up period, accurate measurement of the Poisson ratio is not possible because the pressurization and axial loadings do not resemble pure hoop loading. The actual Poisson ratio ranges from 0.88 to 0.98 which is considered in good agreement with the theoretical values. A reason for the discrepancy would be that the axial stress is small but non-zero; therefore, a component of the transverse Poisson ratio will be contributing to the strains. Additionally, the CLT assumes the material is homogenous and experiences only plane stress, which is not true. The material is heterogenous and there will be a radial stress in the tube's wall. The derivation of the Poisson ratio equation assumes that the laminate is symmetric, therefore; the coupling stiffness matrix is zero. For this study, the coupling stiffness

matrix is not zero but the moments and other forces not acting in the hoop direction are considered negligible.

All specimens exhibited an increase in Poisson ratio as the creep test proceeded. H006 initially demonstrated a much steeper increase in Poisson ratio; this observation is considered to be a startup effect as the strain gauge did not receive an excitation voltage until 32 seconds into the test. The slope for the H006 curve stabilized over time. The increase in Poisson ratio can be explained by the fibre realignment phenomena. Fibres tend to realign towards the direction of the applied stress [105]; in this case they would realign towards the hoop direction, increasing the angle between the longitudinal axis of the specimen as demonstrated in Figure 42. The fibre angle of the specimen is initially 45° but due to fibre realignment, the fibre angle with respect to the hoop direction would decrease to an angle θ while the angle in the axial direction increases to a new angle, β.

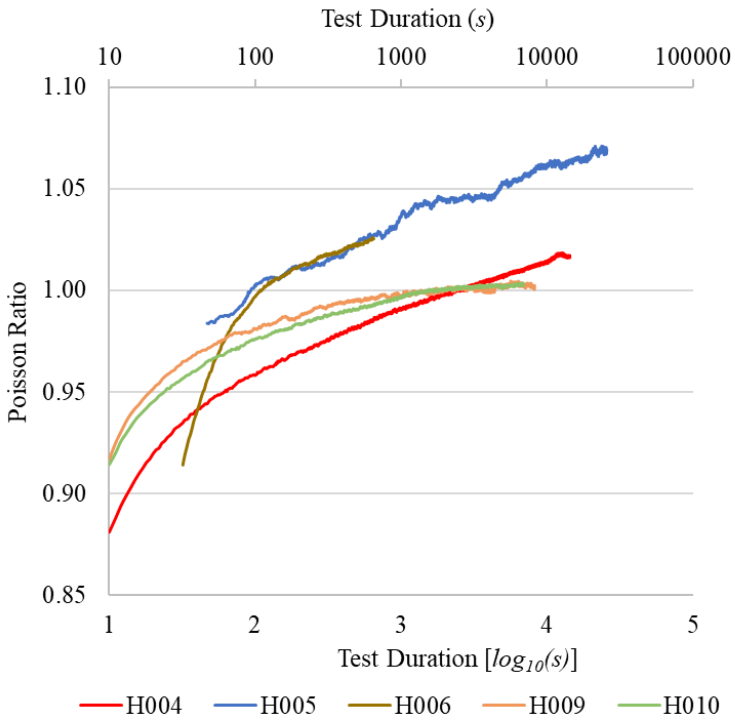

Figure 41: Poisson ratio from strain gauge data

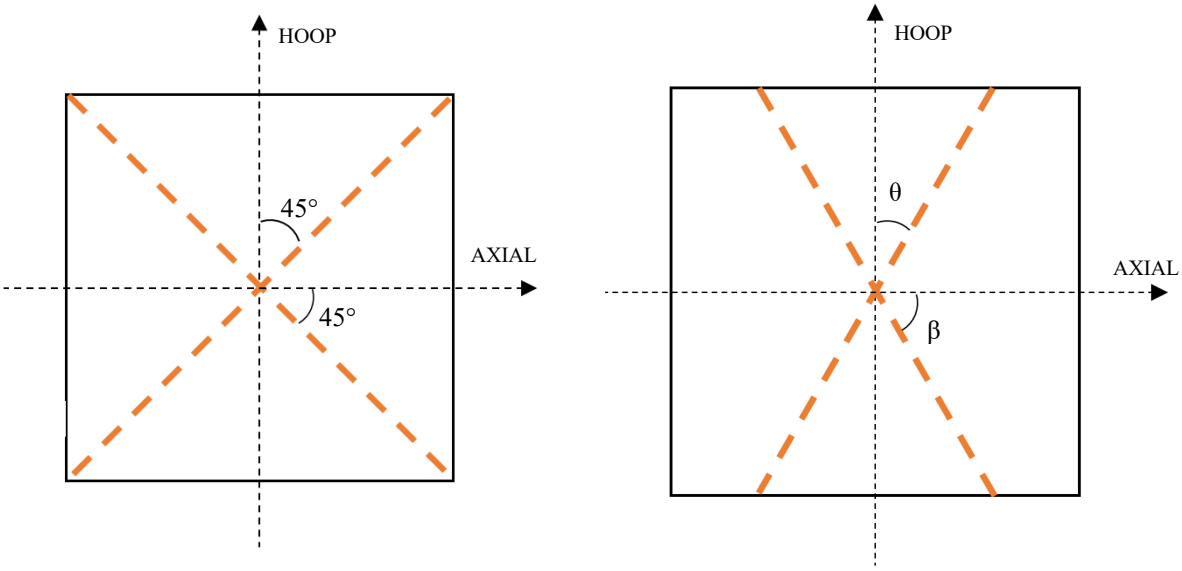

Figure 42: Representation of fibre realignment in specimen

The Poisson ratio eventually increases above 1, indicating the axial strain is higher than the hoop strain despite the loading conditions being predominantly in the hoop direction. This counterintuitive behaviour has been observed in ±45° pipes pressurized in pure hoop [106], as well as, ±45° laminates loaded in pure tension [107]. In both cases, the highest strains before failure were in the direction perpendicular to the applied load which supports the results captured by the strain gauges. The change in Poisson ratio could be a result of the fibre realignment in the specimen. The relationship between winding angle in ±θ degree angle-ply laminates and Poisson ratio, as predicted by the CLT, is shown in Figure 43. As the angle between the fibres and the loading direction decreases below 45°, the Poisson ratio increases. This trend is observed for both low moduli and high moduli properties for the glass fibre and HDPE. The behaviour is not unique to the material in this study; CLT predicts that the Poisson ratio of other FRPCs will behave in this manner [104]. Rosenow [108] observed that a +45° wound pipe with no -45° layers would result in higher hoop strains than axial strains when pressurized in pure hoop loading. The results of Rosenow and the current study would suggest the observed final strains of the specimen is also related to the interaction between the +45° and -45° layers.

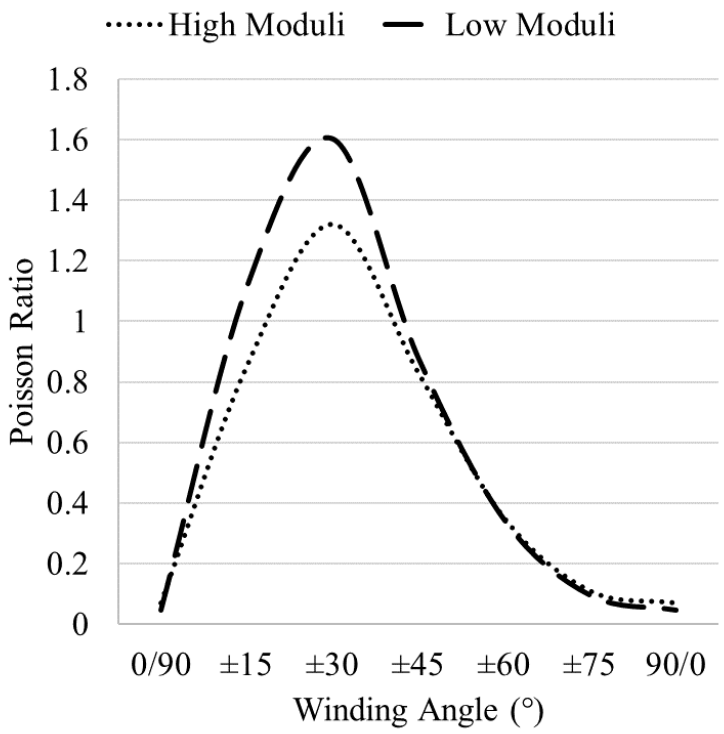

Figure 43: Relationship between winding angle and Poisson ratio for angle-ply laminates

In comparison, Figure 44 shows the Poisson ratio obtained from DIC data. The data was averaged over 5 data points to reduce noise. The starting Poisson ratio from DIC data ranges from 0.84 to 1.15. The upward trend in Poisson ratio observed in the SG data is not as pronounced in the DIC data; in fact, results from H004 and H005 show a downward trend in Poisson ratio. As mentioned previously, the DIC method tends to measure a higher hoop strain but comparable axial strains in comparison with the strain gauges. Since the Poisson ratio is the negative of the ratio of axial to hoop strain; higher than actual hoop strains will result in lower Poisson ratios.

In summary, the strain gauges were able to capture the Poisson ratio in good agreement with theoretical values calculated using CLT. The increase in Poisson ratio could be due to fibre realignment; the behaviour observed is in agreement with previous studies. The DIC data was noisy and in some cases shows a downward change in Poisson ratio which goes counter to previous research.

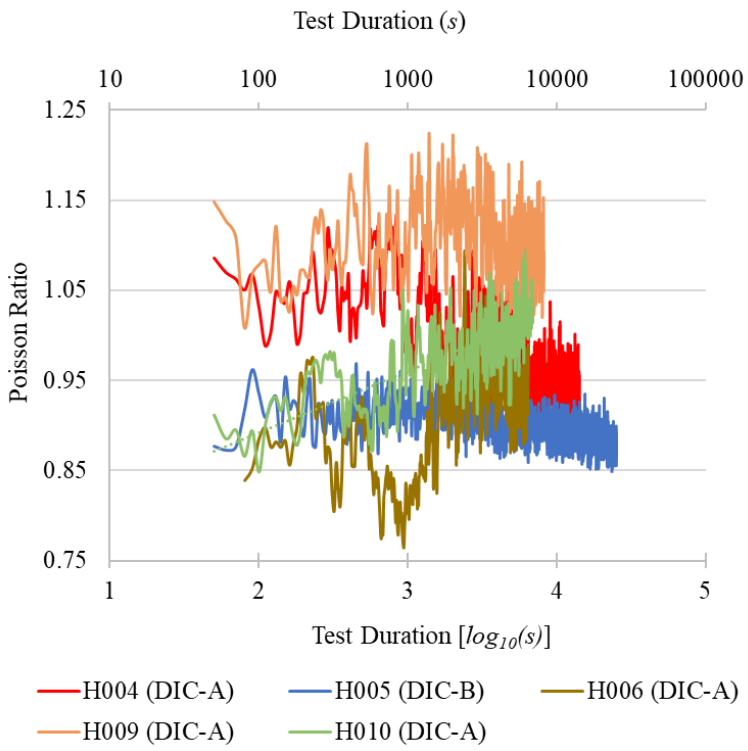

Figure 44: Poisson ratio from DIC data

5.4.4 Compliance and Strain Rate

Two variables of interest obtained from the creep tests are creep compliance and strain rate. Strain rate is the change in strain with respect to a unit of time. To calculate the strain rate, ε_i, at a certain time, i, Equation (46) is used where ε_{i+100} and ε_{i-100} are the strain values at 100 seconds after and 100 seconds before time i, respectively. Similarly, t_{i+100} and t_{i-100} denote the time at 100 seconds after and 100 seconds before time i, respectively. Figure 45 shows the strain rate for the creep tests under pure hoop loading. A region of decreasing strain rate is observed which corresponds to the primary creep stage [109]. The short-term creep tests still exhibit decreasing strain rates when the tests ended. For H004 and H005, the rapidly decreasing strain rate is followed by the steady-state creep region in which the strain rate is more stable (despite the noise) and appears to be close to or at a minimum. The operating life of the material will have the longest duration under steady-state creep due to the shorter time duration of primary and tertiary creep [110]; therefore, it is the most important region for obtaining creep material properties. The results show that steady-state creep is not achieved for the short-term test

durations; it is recommended to conduct future tests for a minimum of 4 hours to reach steady-state creep. Due to the low strain rate values, they are affected by noise in the strain gauge measurement as the tests progress. The low strain rate of GFR-HDPE in the steady-state region is advantageous for application to structures with a long operating life, such as pipelines. The low strain rate means less deformation over time. It is noted that the low stress state also contributes to the low strain rate; therefore, tests at higher loadings should be conducted as part of future work to understand the behaviour of the material under a variety of loading conditions.

$$\dot{\varepsilon}_i = \frac{\varepsilon_{i+100} - \varepsilon_{i-100}}{t_{i+100} - t_{i-100}} \tag{46}$$

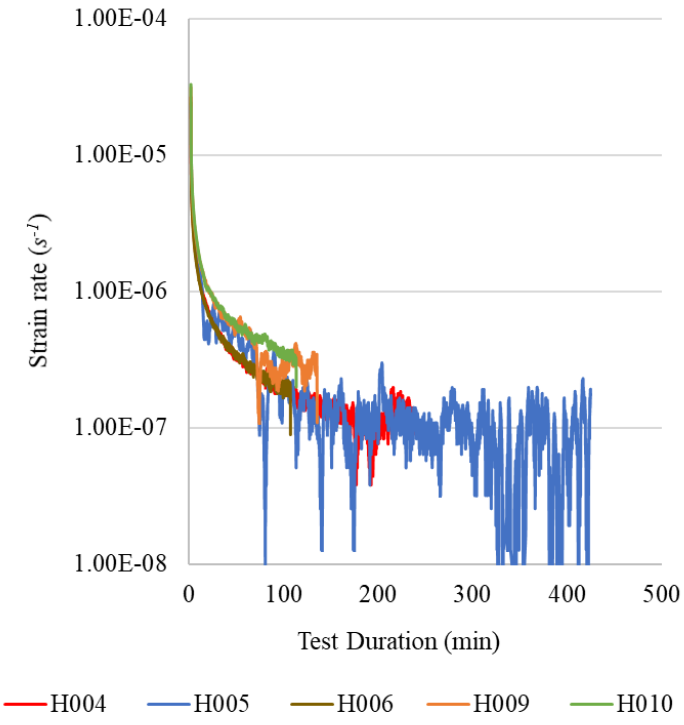

Figure 45: Pure hoop strain rate

Figure 46 compares the strain rate of specimens from Batch #1 (H009 and H010) to a specimen from Batch #2 (H004). The ratio of strain rates being higher than unity, indicated by the red line, demonstrates the specimens from Batch #1 have a higher strain rate than specimens from Batch #2. This result is expected because the final strain value for Batch #1 specimens is higher

and could be the result of differences in crystallinity as mentioned previously. As the test progresses, the strain ratio value increasingly fluctuates. Specimen strain rates from both batches are near zero and fluctuations, such as that caused by noise, will result in large fluctuations in the strain rate ratio.

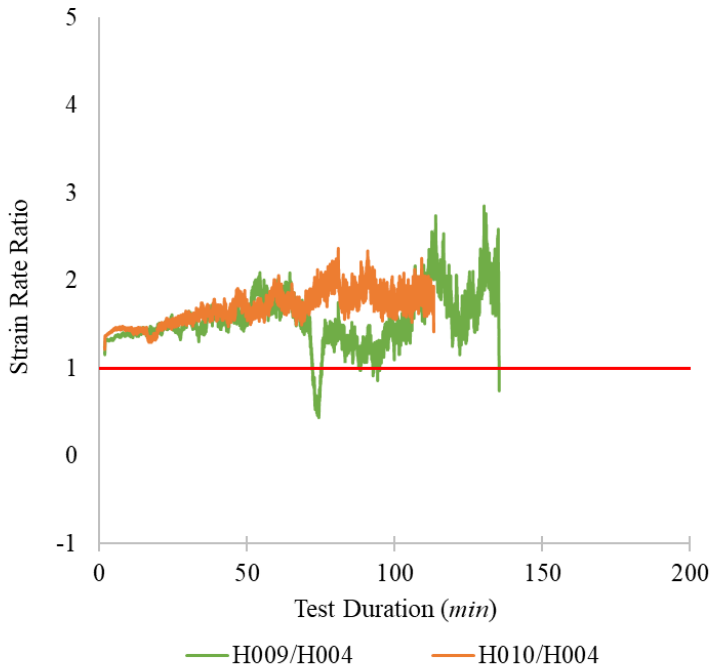

Figure 46: Comparison of strain rate

Figure 47 shows the change in creep compliance of the specimens during the pure hoop tests. The increase in creep compliance, which is the ratio of strain to applied stress, has been observed during creep of other fibre-reinforced polymer composites [72, 68]. The result is expected since the stress is held constant while the material experiences creep strain over time. In comparison, Elleuch and Taktak [111] observed a creep compliance above 2×10^{-3} MPa^{-1} for pure HDPE subjected to 10 MPa pure tensile stress; this value was observed at approximately 2.5 hours (9000 seconds) into the creep test. The comparison between this study and the work of Elleuch and Taktak supports previous research [73] which has shown reinforcing a pure polymer with fibres can result in a lower creep compliance.

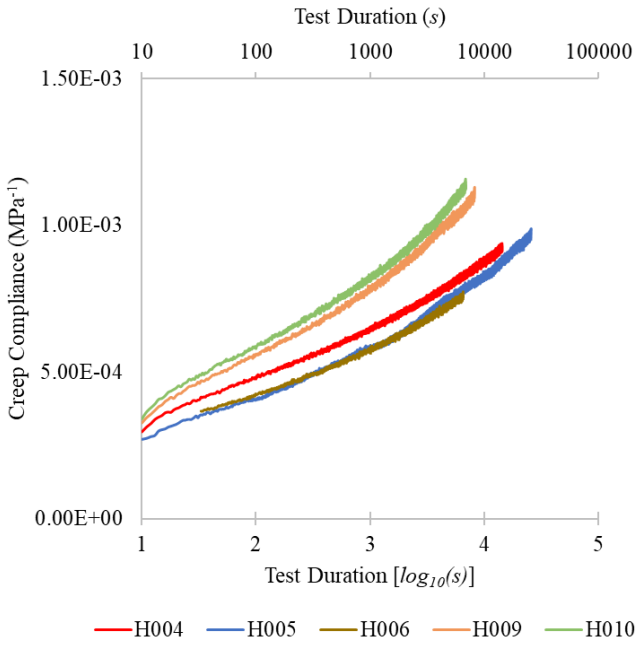

Figure 47: Pure hoop creep compliance

5.5 Pure Axial Compression Creep Test Results

The initial strain was calculated for the pure hoop tests to verify the measured strain agreed with the CLT; the calculation was not conducted for the compressive tests since the fibres are considered to be realigned to a new, undefined angle after the pure hoop creep tests. In addition, the specimen was left to in the testing machine overnight, which could result in recovery of the material. Recovery effects could also affect the fibre angle of the specimen. The added parameter of fibre angle was considered to add too much variability to the calculation to make it worthwhile. It is assumed the strain gauges were still in working condition after the initial test due to the low loading conditions and no debonding of the strain gauge was observed. The initial and final strains for the specimens under pure compressive loading are shown in Figure 48.

The axial and hoop strains from H005b and H010b were within 2% and 7% of each other at the reference time of 100 minutes. Due to a calculation error, the axial force applied to H004b (the first axial compression test conducted) was higher than it should be which would explain the higher strain.

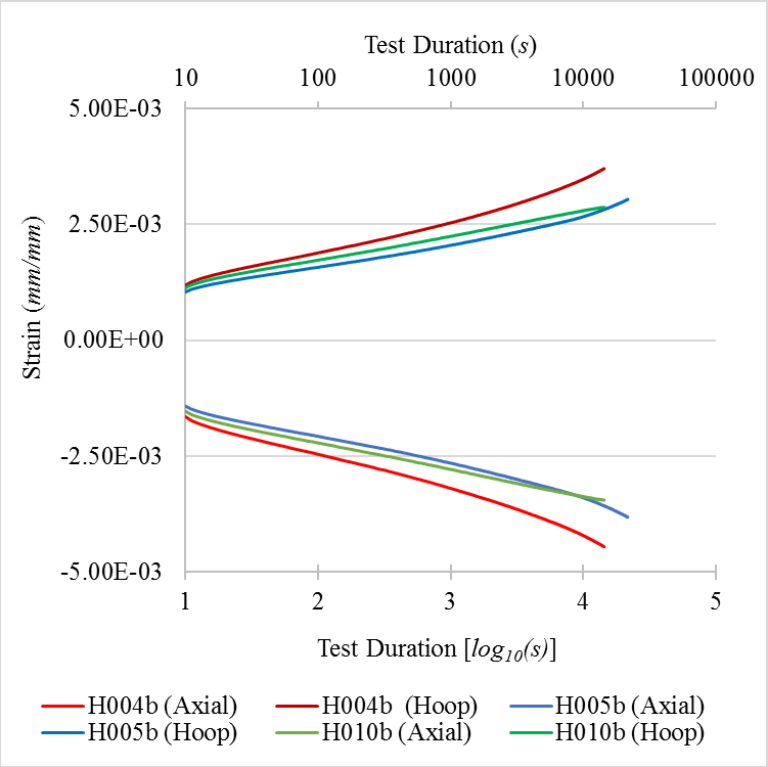

Figure 48: Strains experienced during axial compression creep tests

Figure 49 shows the strain gauge and DIC measurements for an axial compression test. The applied stress is 5 MPa; therefore the strain values are expectedly lower than the pure hoop tests which were conducted at 10 MPa. The bias in the hoop strains is also observed for these tests; however, this result demonstrates DIC can be used for good agreement with strain gauge measurements for both axial and compressive loading conditions.

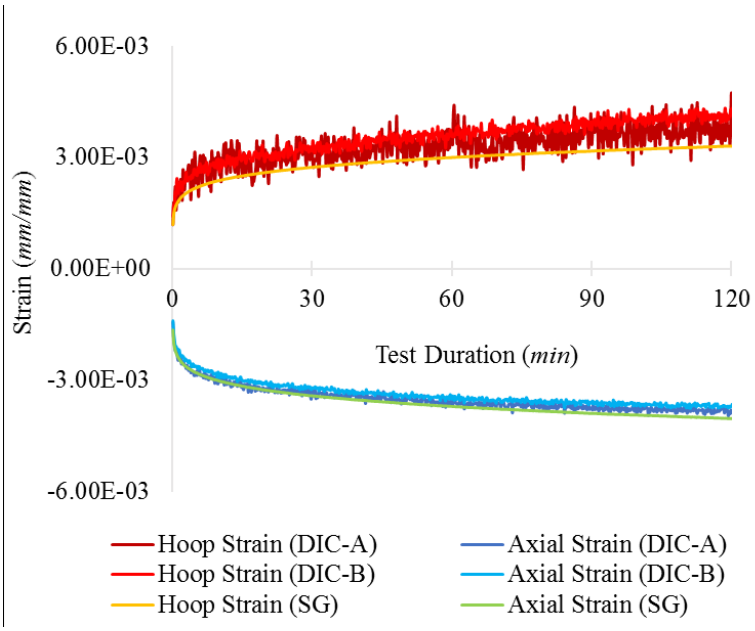

Figure 49: H004b test results

Figure 50 shows the change in Poisson ratio captured by the strain gauge measurements in the axial compression tests. The material has a lower Poisson ratio at the beginning of the test which agrees with the hypothesis that the fibres realigned. Recalling from the plot in Figure 43, the Poisson ratio will decrease as the fibre angle increases from 45 degrees with respect to the loading direction. Since the load is now in the axial direction and the fibres had realigned towards the hoop direction, the fibre angle between the loading direction has increased. The upward trend in Poisson ratio is observed which could be due to fibre realignment towards the direction of the applied load . It appears the material behaves in the same manner for the tensile and compressive loadings used in this study. Despite, the increasing Poisson ratio, it does not go above 1 which means the final axial strain is higher than the hoop strain for axial compression. Experiments conducted by Elghazouli [112] for a composite pipe with ±45° winding angle subjected to axial compression agrees with the trend in final strains observed in this study. The upward trend in Poisson ratio is also captured by the DIC measurements as seen in Figure 51; however, it is suspected that this is a coincidence as opposed to DIC being more accurate under compressive loading. The loading direction is in the axial direction which means the equation for Poisson ratio is now given by Equation (47). DIC tends to overpredict the hoop strain; in the case

of compression loading, the higher hoop strain calculated by the DIC will result in higher Poisson ratios.

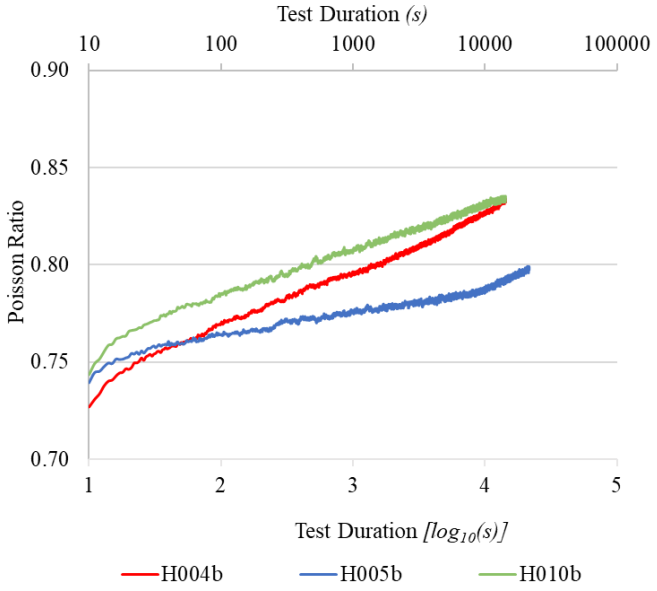

Figure 50: Pure axial compression Poisson ratio (SG)

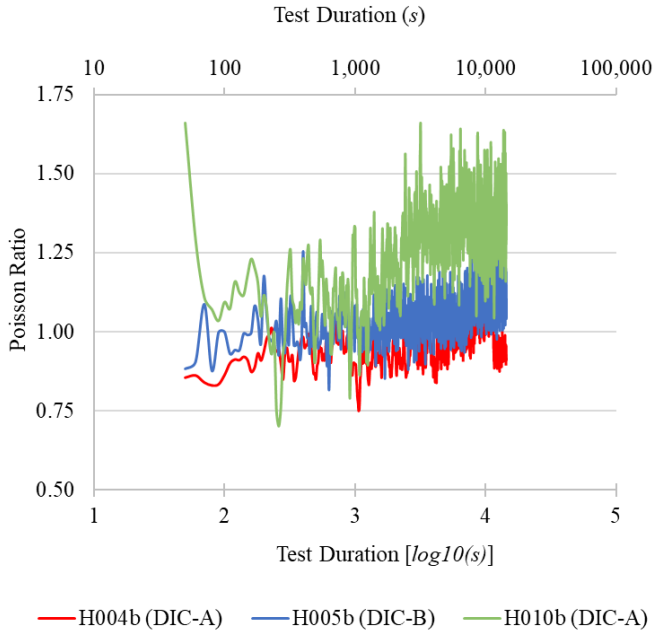

Figure 51: Pure axial compression Poisson ratio (DIC)

$$\nu = -\frac{\varepsilon_{hoop}}{\varepsilon_{axial}} \tag{47}$$

Figure 52 shows the strain rate for the axial compression tests. It is observed that the pure hoop tests having a higher stress of 10 MPa caused a higher strain rate than the axial compression tests which had a 5 MPa stress level. The strain rate is lower than the steady-state strain rate for pure HDPE of 2.22×10^{-6} s^{-1} observed by Pereira et al. [113]. The creep experiments conducted by Pereira et al. were at 3 MPa stress and only for 10 minutes but it provides an indication that the GFR-HDPE material has a reduced strain rate compared to the pure polymer.

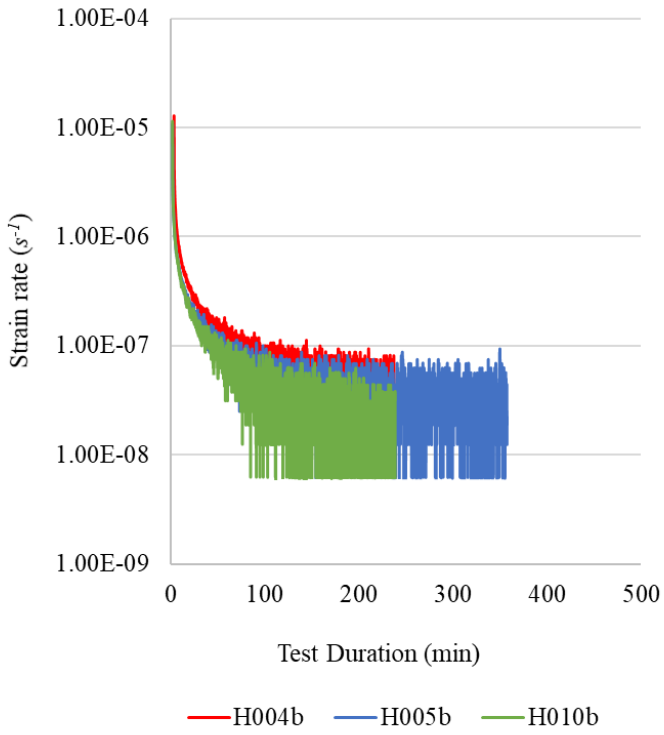

Figure 52: Pure axial compression strain rate

Figure 53 compares the strain rate of H010, from Batch #1, to H005b, from Batch #2. Due to the lower strain rates, the strain rate ratio is now more affected by noise; to reduce noise, the calculated values are averaged over 5 time steps. The strain rate ratio of H010b to H005b is much closer than the strain rate ratio seen in the hoop creep tests. A possible reason for this can

be attributed to fibre realignment. Test H005 was longer than Test H010 and a greater degree of fibre realignment could have occurred during this time. The fibres for H010 at the end of the test would be more aligned to the axial direction, which will allow for a higher resistance to creep in that direction. This result would suggest that initial fibre angle, as well as, fibre realignment can have a large role in creep rate.

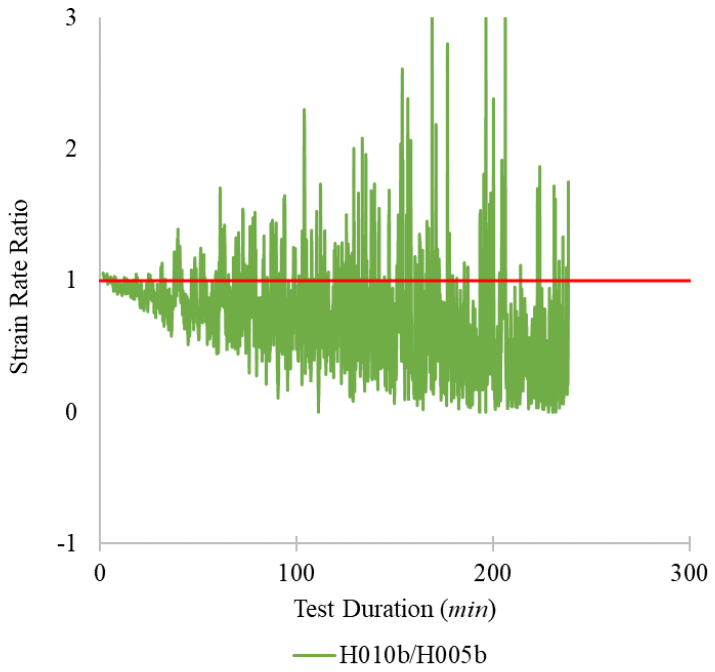

Figure 53: Comparison of strain rate (pure axial compression)

The creep compliance for axial compression tests are shown in Figure 54. The creep compliance is lower than observed during the pure hoop tests. This could be due to the lower stress level but also due to fibre realignment, which changes the properties of the material. In comparison, Elleuch and Taktak [111] observed a creep compliance of approximately 2×10^{-3} MPa^{-1} for pure HDPE subjected to 5 MPa compressive stress; this value was observed at approximately 2.5 hours (9000 seconds) into the creep test. fibreThe GFR-HDPE has demonstrated a lower creep compliance compared to the pure HDPE used by Elleuch and Taktak under both tensile and compressive loadings.

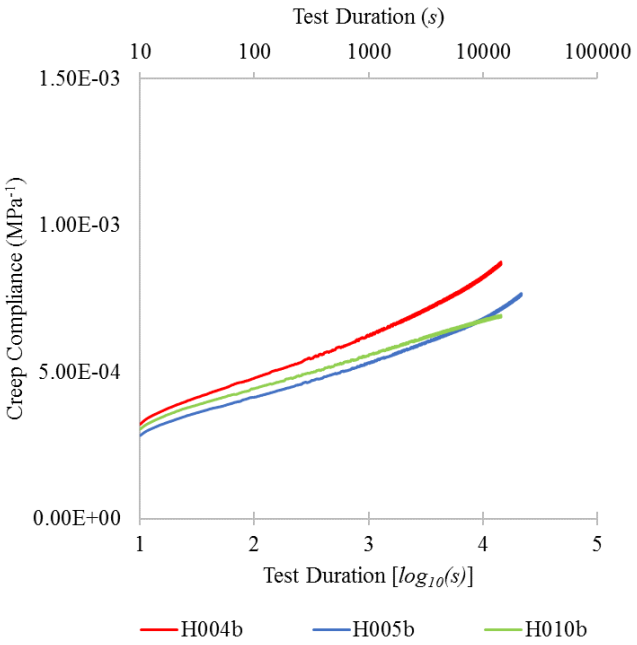

Figure 54: Pure axial compression creep compliance

5.6 Discussion of Discrepancies or Limitations

Based on the good agreement seen in the test results, DIC is considered a suitable technique to verify the strain gauge readings; however, there is room for improvement. Two issues observed with the DIC measurements is noise and a tendency to measure higher hoop strains than strain gauge measurements. The following section will identify possible reasons why the hoop strains measured by DIC, especially DIC-B, displays greater discrepancy than axial strains and possible improvements to the DIC setup.

Bias in the DIC measurements could be the result of poor calibration [83]. Proper calibration of the DIC system requires tilting of the calibration board in the vertical and horizontal directions. Due to the limited space around the test machine fixture, it is difficult to tilt the calibration board forward and backwards vertically while standing in front of the test machine. Standing behind the test machine allows more room and flexibility and allows a greater range of motion. Calibration for tests H004, H004b, H005 and H005b were conducted while standing in front of the testing machine; calibration for other tests were conducted while standing behind the testing machine. Both methods yielded non-abnormal calibration scores. It is

questionable that poor calibration would still allow good agreement between the DIC-A and SG readings.

It does not matter whether the calibration images are taken before or after the test since the post-processing software does not know when the calibration images are taken; however, the camera position and settings must remain unchanged. To test the effect of calibrating while standing behind or in front of the testing machine, tests H010 and H010b were calibrated using both methods to check for noticeable changes in strain measurements. For both tests, the change in calibration did not remove the bias in hoop measurements; in fact, for H010, there was little change in the strain measurements and the overall discrepancy with SG values did not change. There is confidence the calibration method is not the cause of the bias observed in the measured hoop strain. Regardless, it is recommended to perform the calibration while standing behind the test machine to allow for a greater range of motion when tilting the calibration board.

According to the DIC system developer, the ideal speckle pattern should have a speckle size between 3 to 5 pixels [85]. The size distribution of the speckle pattern from all specimens was measured using image analysis software, ImageJ, and a typical size distribution is displayed in Figure 55. All specimens had a high concentration of speckles in the size range of 1 pixel up to 3 pixels with the second highest concentration being speckle size above 10 pixels. The high concentration of smaller than ideal speckles will cause the moiré effect observed in Figure 37 and Figure 38 because the camera resolution cannot capture all the details if the speckle pattern is too fine [85]. The moiré pattern can cause noise and bias [83]; however, the application of a random speckle pattern using spray paint is not considered the cause of the bias in the hoop strain. The moiré pattern is present in both the axial and hoop strain contour maps but a greater biasin hoop strain, compared to the strain gauge measurements, is observed. The ideal speckle size range of 3 to 5 pixels are a guideline and the developer admits that good results can be obtained even if the speckle pattern is not ideal [85]. The result of this study confirms DIC measurements in good agreement with strain gauge readings can be achieved with a less than ideal speckle pattern.

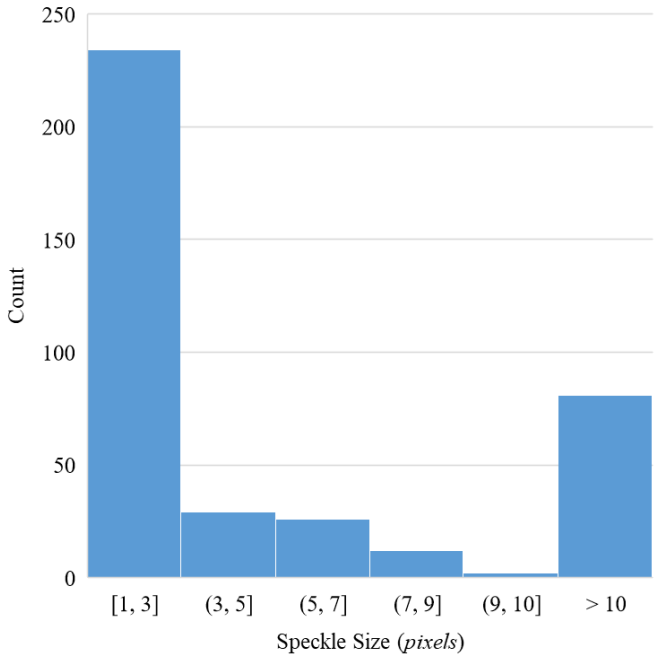

Figure 55: Speckle pattern size distribution

Spray paint was selected for applying the speckle pattern because it has been shown to obtain DIC results in good agreement with strain gauge measurements of polymer composite tubes [114]; however, it is a challenge to control the size of the speckles. There are several possible ways to improve the speckle pattern size distribution. Based on the author's experience, decreasing the distance between the specimen and the spray can during the application process can increase the speckle size. . Alternatively, the DIC camera setup can be brought closer to the specimen so the speckles appear larger on screen; however, this would require readjusting all the camera settings. The DIC system developer also sells a patterned paint roller which allows for application of the pattern but this is considered to be the most expensive option. A less-expensive method that could allow better control of the speckle pattern is to spray paint the specimen white and then manually create black dots using a marker. The size of the marker tip could be selected so the correct speckle size is obtained and the spacing of the dots can be well controlled. Extra care would be required to ensure the pattern being applied is random. The objective of the study was to provide a setup for DIC to verify the strain gauge measurements which has been demonstrated; optimization of the system will be left for future work.

The polycarbonate shield between the camera and the specimen is considered the most probable reason for the bias seen in the DIC-measured hoop strains. It has been demonstrated that a glass pane placed between the specimen and DIC setup will result in measurement errors due to refraction [115]. Refraction causes light to bend as it passes through a medium therefore the position in which the speckles appear to be is not accurate. The refraction index of polycarbonate is even higher than that of glass (1.58 versus 1.51) [116, 117]. The effect of the shield presence was investigated in this study. While the specimen is resting in the test machine, 12 images of were taken: six images with the shield and six without the shield. It was expected the measured strain to be zero. To account for noise in the measurements, the strain measurements were averaged over five pictures; the first image is the reference image and not used in the results. In total, three different specimens were used; the measured strains are summarized in Table 8. The change in strain measured with the shield is place is small but large enough to not discount it as the effect of noise in the measurements. The results indicate the shield does have an effect on DIC strain measurements; it is unclear how significant this effect would be if the specimen was stressed and experiencing deformation. It is considered unsafe to apply loading to the specimen without the shield in position though.

Table 8: Comparison of strain measurements with and without shield

Specimen	**No Shield (*mm/mm*)**		**Shielded (*mm/mm*)**	
	EXX	EYY	EXX	EYY
1	2.95E-05	5.53E-05	9.93E-05	1.10E-04
2	1.53E-05	6.75E-05	2.61E-04	-1.91E-04
3	4.54E-05	1.58E-04	9.25E-05	4.37E-04

The shield has five sides and is usually placed in the testing machine such that the side which is between the camera and specimen is angled for reduced glare. The DIC software developer indicates if a glass plane is to placed between specimen and cameras the glass pane should be positioned parallel to the camera sensors [118]. The effect of positioning the shield in a position for reduced glare and positioning it perpendicular to the camera sensors was tested in this study. For H005, a pure hoop test, the shield was positioned for reduced glare and the results are shown in Figure 56. The same specimen and camera setup was used for test H005b, a pure

axial compression test, but the shield was positioned so one side was perpendicular to the camera setup. The results for the H005b test are shown in Figure 57. The DIC results for the H005b test have greater noise compared to H005. The change in shield position appears to have caused more glare which is known to increase noise [83]. This results demonstrates the important role that shield position plays in DIC measurements for this setup. At this time, no optimal position for the shield has been determined; the shield position is adjusted and the amount of glare seen on the DIC image recording software is checked each time before the test. One solution to reduce the effect of the shield is to eliminate it completely by placing a safety barrier around the entire test area.

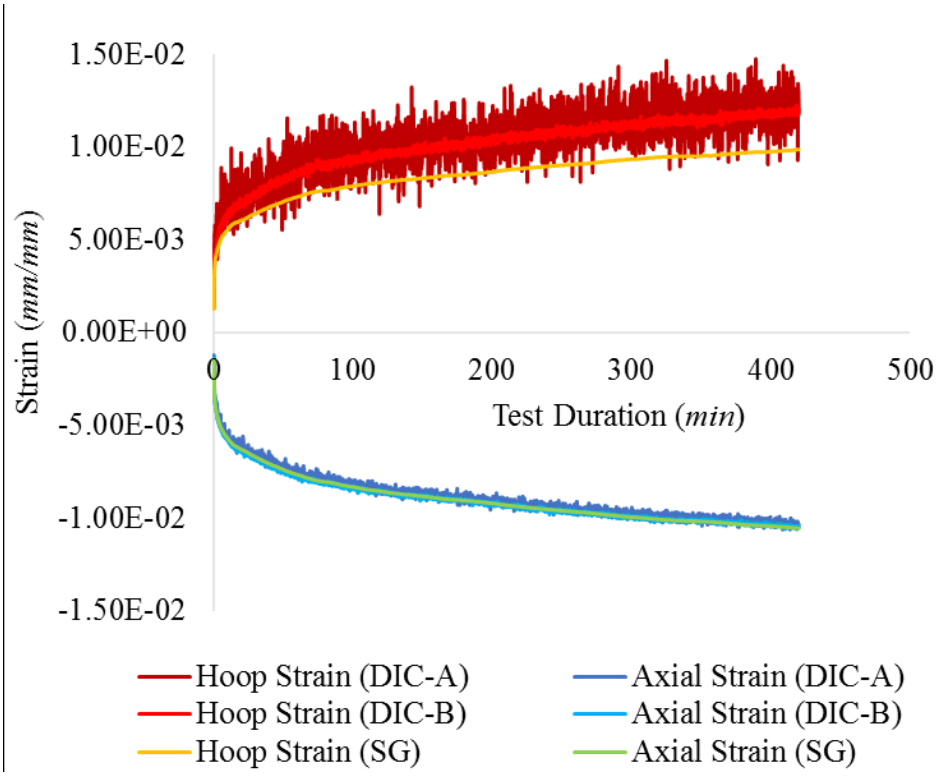

Figure 56: H005 test results

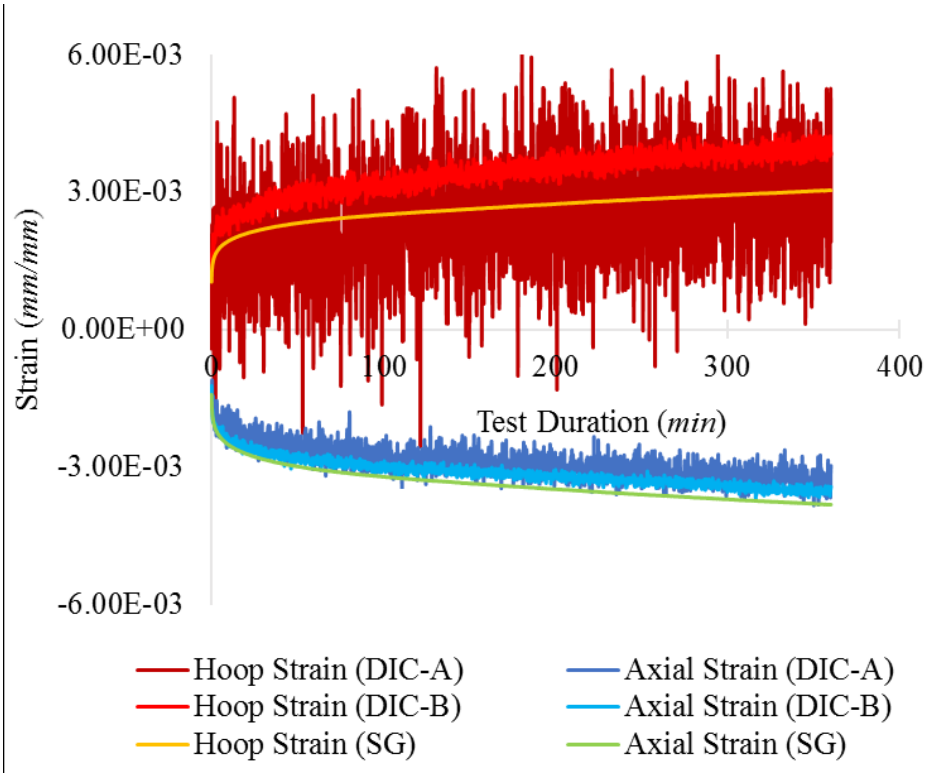

Figure 57: H005b test results

In addition to the shield position, sources of light besides the LED, such as sunlight, might affect the measurements of the test. There are sunroofs next to the test area; the angle of sunlight passing through those sunroof changes depending on time of day. It was noted that at around noon on sunny days, sunlight will be shining directly on the testing area. Although sunlight does not shine directly on the test machine, there is a possibility sunlight can reflect off of surfaces and be directed on the testing machine. In at least one test, areas of light are seen changing position in subsequent test images as the test progressed. The fact that light can shine in the test area has the potential to disrupt the test. A case for the need of a constant and controlled test environment is demonstrated in the comparison of test H010 and H010b. H010 was tested in pure hoop; the test started around 11:00 am. H010b, a pure axial compression test, was tested the next day using the same specimen and camera setup. H010b was tested on a cloudy day and the test images of H010 are noticeably brighter than H010b. Figure 58 and Figure 59 compare the test results of H010 and H010b. The DIC results for the H010b test have greater noise compared to H010. Upon review of the test images for H010b, the shield position could have shifted slightly overnight; therefore it is unclear what caused the additional noise but it is clear that

lighting conditions change and needs to be controlled. To better control the lighting conditions, a tarp or canopy could be placed in the testing area to block out the sunlight. Lights additional to the LED would be required to counter the decrease in ambient light.

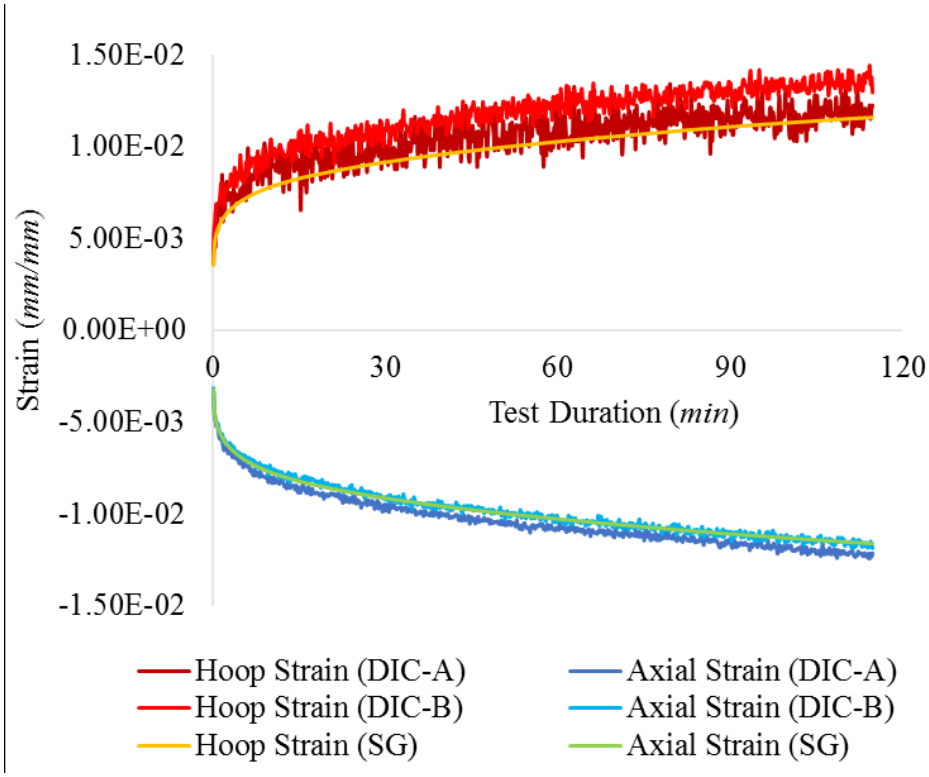

Figure 58: H010 test results

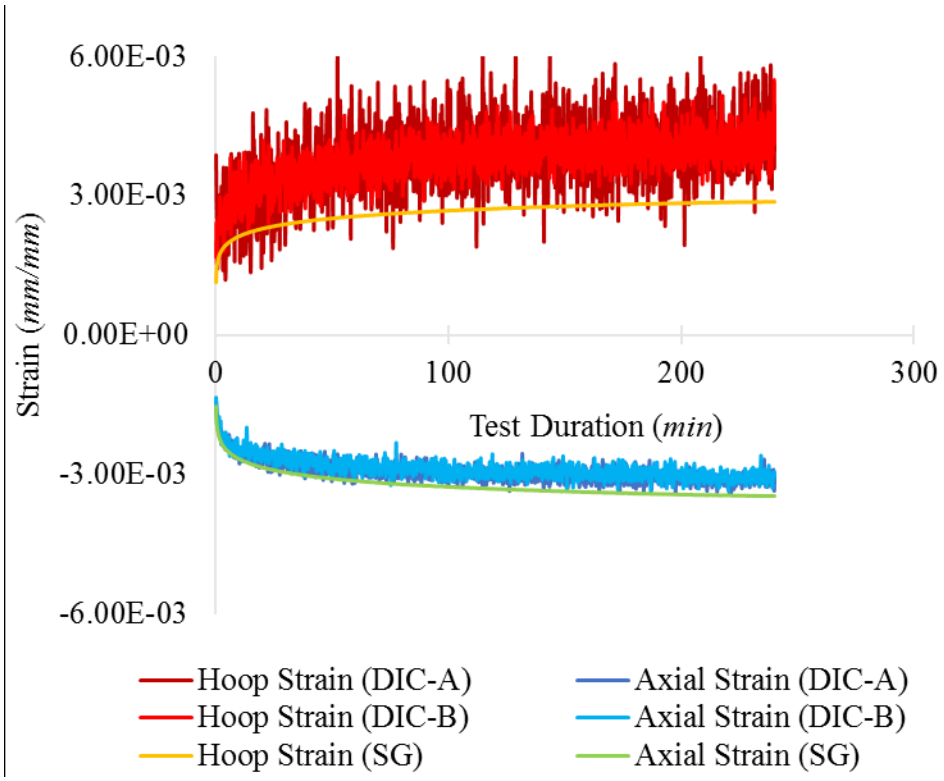

Figure 59: H010b test results

Shield position and changes in surrounding light can explain the increased noise but there is also the greater bias in hoop strain, compared to axial strain, to consider. It is unclear at this time what caused the result. One theory is that the curved surface of the tubular specimens combined with the shield is making it difficult for the DIC setup to accurately calculate the strain. The author is not aware of any feature of the DIC software that allows for input of the shield thickness or refraction index of the material; therefore, the software will not be able to accurately adjust for the presence of the shield. It has been demonstrated previously that the shield has an effect on the strain calculation; the curved surface of the cylinder can possibly add greater uncertainty. Figure 60 demonstrates that the distance between the shield and the specimen would change for a speckle moving along the circumference of the tube from Point A to Point B. In comparison, a speckle moving from Point A to Point B along the axial direction of the specimen will be approximately equidistant from the shield. In reality, the surface of the tube will have a curvature since it is being pressurized but the curvature in the axial direction should be less pronounced than the curvature along the circumference.

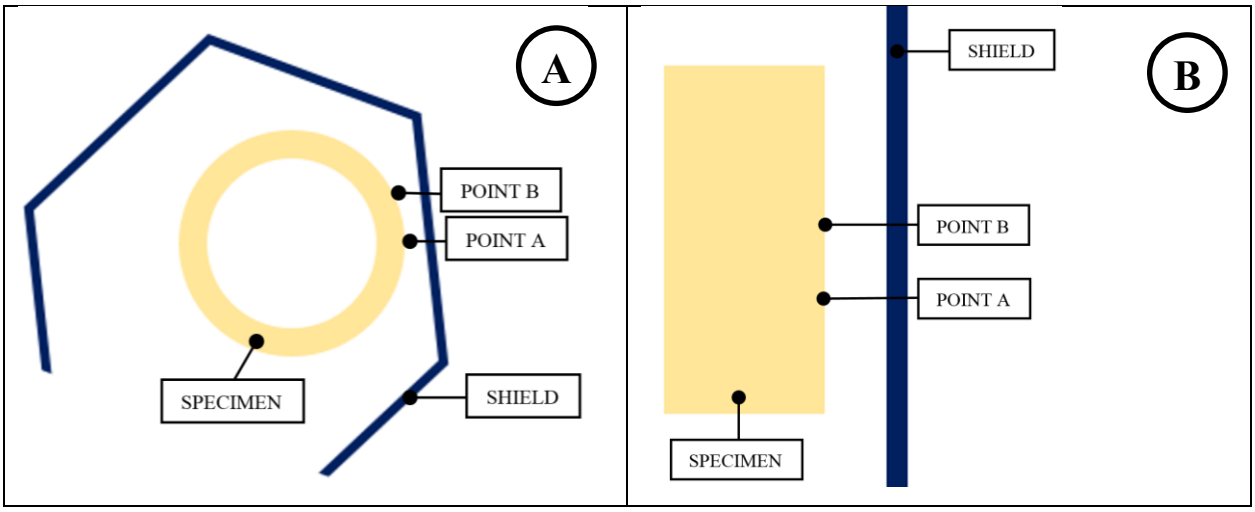

Figure 60: Motion of speckle in (a) vertical direction and (b) horizontal direction

Another theory to explain bias in hoop strain measured by DIC could be due to the improper setup of the camera system or DIC software, which prevents the DIC system from capturing the cylindrical profile of the specimen. If this was the case, it is expected that DIC-B measurements would consistently have greater bias than DIC-A since the area of interest for DIC-B experiences greater curvature change. However, the bias in hoop strain affected both DIC-A and DIC-B measurements. Furthermore, Figure 61 demonstrates the DIC system is capable of capturing the specimen's profile. It should be noted that the recommended stereo angle between the cameras is a minimum of 15° [119] but the angle used in the study was 4°. This is not considered the main cause for the bias in hoop strain but could be a starting point to improving the DIC measurements for future creep tests.

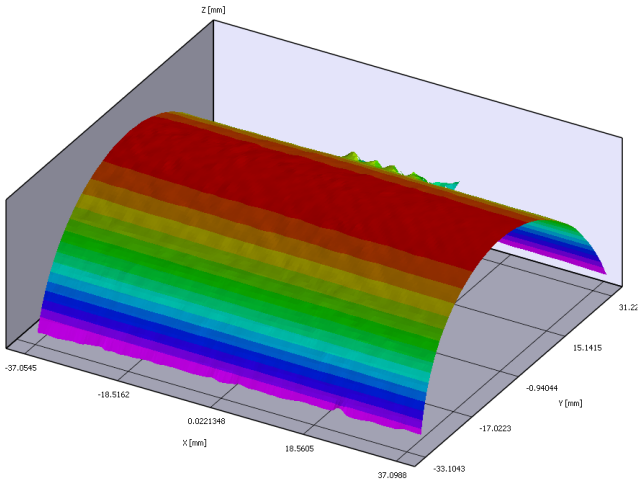

Figure 61: Specimen profile in Vic-3D software

To further improve the accuracy and repeatability of the DIC setup, better control of the lighting conditions, elimination of the shield and improving the speckle pattern should be implemented. The current DIC setup is not optimized; however, it is capable of measurements that are used to verify the SG readings. Table 9 compares the advantages and disadvantages of the DIC system and the strain gauge measurement system that were learned during the study.

Table 9: Advantages and disadvantages of strain gauges and DIC measurement methods

	Advantages	Disadvantages
Strain Gauges	• Real-time strain measurement	• Only measures surface strains • Measures strain in small location • Susceptible to misalignment or surface nonconformities • Used for single specimen
Digital Image Correlation	• No contact with specimen • Can analyze large areas • Can measure other variables than strain (such as displacement) • Provides strain contour map	• Only measures surface strains • Shield causes refraction errors • Long tests require large amount of storage for pictures • Requires control of lighting conditions

5.7 Empirical Creep Modelling

It has been demonstrated that the creep tests produced repeatable results in which the initial elastic strains agreed with theoretical calculations and the creep strains measured from both measurement techniques were in good agreement with each other. Although not all tests entered the steady-state creep phase, the observed creep strain rates were near zero. Based on these observations, the data is considered suitable to verify agreement with creep theory in the Findley Power Law and Burgers models.

The Burgers model (BM) and Findley Power Law (FPL) were used to fit the data from pure hoop and axial compression creep tests. Figure 62 shows the agreement between the theoretical models and the experimental results for the pure hoop tests. Material creep parameters were obtained for all creep test results but only one specimen each from short-term, intermediate and long-term creep tests are shown in the graph for clarity. The strains predicted by the BM and FPL show high deviation from the experimental strain values during the ramp up period of 10 seconds. Ten seconds after the ramp up period, FPL predicted values are within 10% of the experimental values. The BM shows higher deviation from experimental values than the FPL initially after the ramp up period; however, it also predicts within 10% of experimental results as the tests progressed. Xu et al. [120] conducted creep tests on a fibre-reinforced HDPE composite material and also noted that the fit between BM and experimental data improved as the creep test progressed. Overall, the average of the absolute percent difference between the experimental results for both models from after ramp up to end of hold period is under 1%. On average, FPL provides predictions closer to experimental results than the BM.

Assuming tertiary creep does not occur, the strains predicted by both models, for up to 12 hour long tests, are shown in Figure 62. It demonstrates the importance of models; they allow estimation of strain values when lengthy experimental tests are not possible since, for safety reasons, the testing machine can only be operated during normal working hours. The BM appears to over-predict the strain. The Burgers' model overpredicts greatly compared to the Findley's model for the short-term creep test data. The BM is not recommended for curve fitting with short-term creep tests (approximately 2 hours) since it results in a much higher predicted strain rate. Longer test periods, which provided more data points, resulted in a smaller difference between predicted values of the models.

Figure 63 shows the agreement between the theoretical models and the experimental results for the axial compression tests. Both models demonstrate good agreement with experimental results in both tensile and compression loading. The result was expected since both models have been shown to be in good agreement for fitting creep data of fibre-reinforced HDPE composite materials [120, 121, 122].

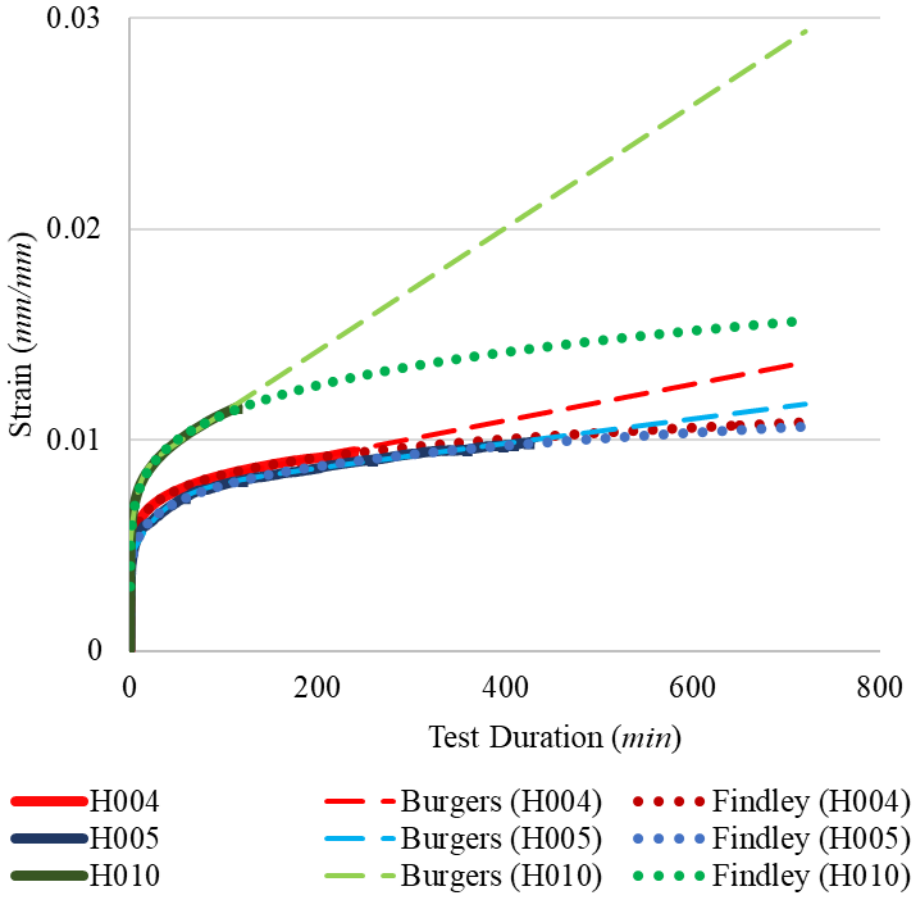

Figure 62: Curve fitting the hoop strain data from pure hoop creep tests

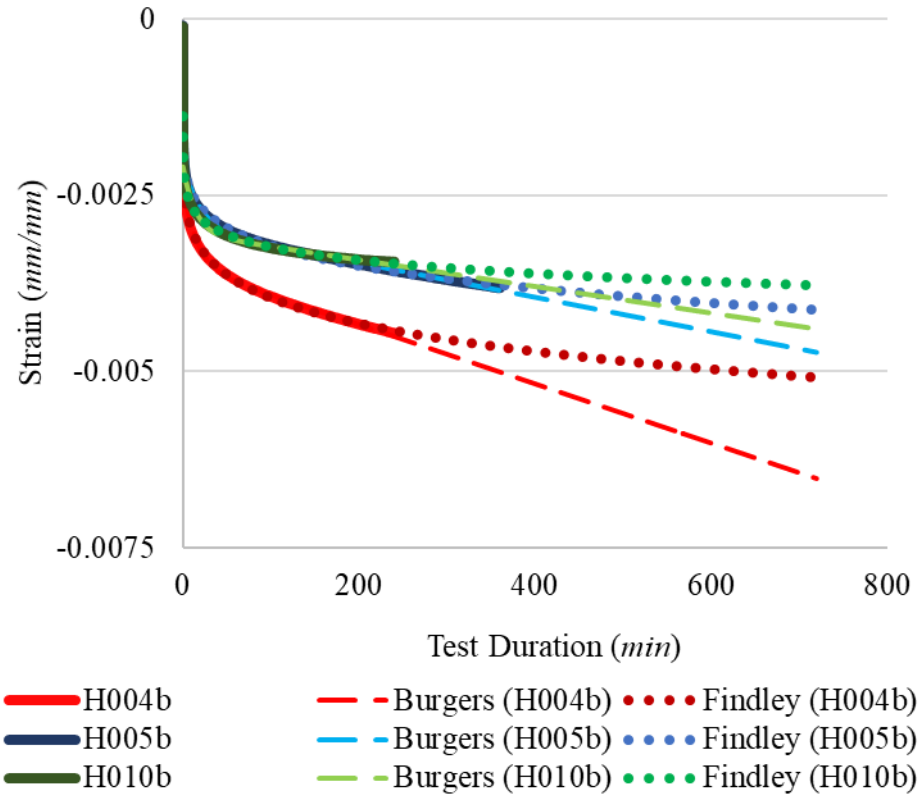

Figure 63: Curve fitting the axial strain data from pure axial compression tests

The material creep parameters obtained from the Findley's Power Law and Burgers model are shown in Table 10 and Table 11, respectively. The results from H006 do not agree with the other test results possibly due to the lack of strain data in the early stage of the creep test. The parameters were obtained by curve fitting the experimental data using MATLAB's built-in Curve Fitting app. The error sum of squares (SSE) and root mean square error (RMSE) values are close to zero while the adjusted R^2 values are close to 1 which confirm the models are a good fit for the data. FPL fits the data better than BM which was observed by Wang et al. [122] in their comparison of the models for curve fitting creep data of a fibre-reinforced HDPE material.

The Findley model fits the data better than Burgers model which can be explained by the fact that it is an empirical model found to be in good agreement with results from creep tests of pure polymers including polyethylene [123], in some cases the fit was performed on 15 years worth of creep test data [124]. As mentioned previously, the creep properties of the composite are predominantly determined by the matrix material; therefore, if the model can fit the pure polymer it is reasonable to expect it will fit GFR-HDPE.

The n term in the FPL is a material dependent term and the values in Table 10 do not differ greatly from the value of 0.154 for polyethylene observed by Findley and Tracy [124]. Wang et al. [122] also observed similar values for n (ranging from 0.119 to 0.185) when using FPL to curve fit the creep data of their fibre-reinforced HDPE material. This would suggest the addition of fibre reinforcement to polyethylene does not significantly change the value of n compared to the pure polymer.

Although FPL provides the better fit, the Burgers model uses the elastic spring and dashpot models and more material parameters which allows for better description of the behaviour of the material. As mentioned in Chapter 1, the E_1 term is related to elastic deformation, the η_1 term is for viscous deformation and viscoelastic deformation is related to the E_2 and η_2 terms. All terms for the specimens from the first batch are higher than the specimen from the second batch, which explains why they experienced higher strains during the test duration. As mentioned before, the hypothesis for the different material behaviour is increased crystallinity introduced due to different heating inputs during the tape winding process. The specimens tested in axial compression display an increase in the E_1, η_1 and E_2 terms. Fibre realignment can not explain this result since the fibres are considered to have realigned towards the hoop direction during the pure hoop tests; this would reduce the modulus of the specimen in the axial direction. Strain hardening due to plastic deformation and realignment of polymer chains could be a reason for the increase in Burgers parameters. This result suggests that the effect of strain hardening was greater than the effect of fibre realignment.

Table 10: Creep parameters determined for Findley's Power Law

	ε_0	ε^+	n	SSE*	RMSE**	Adjust R^2
H004	-6.15E-04	3.07E-03	0.124	5.292E-05	6.076E-05	0.9962
H005	-8.74E-04	2.59E-03	0.140	1.096E-04	6.545E-05	0.9968
H006	2.16E-03	7.62E-04	0.226	3.579E-06	2.348E-05	0.9992
H009	-5.09E-04	3.00E-03	0.151	6.6445E-05	8.854E-05	0.9956
H010	9.31E-04	2.11E-03	0.182	9.227E-05	1.157E-04	0.9931
H004b	-4.12E-04	-1.05E-03	0.140	1.438E-05	3.16E-05	0.9947
H005b	-9.52E-04	5.10E-04	0.171	2.004E-05	3.046E-05	0.9927
H010b	2.20E-03	-3.58E-03	0.048	1.193E-05	2.877E-05	0.9873

*sum of squares error

**root mean square error

Table 11: Creep parameters determined for Burgers Model

	E_1 (GPa)	η_1 (GPa·s)	E_2 (GPa)	η_2 (GPa·s)	SSE	RMSE	Adjusted R^2
H004	2.13	7.10E+04	3.83	4307	2.457E-04	1.309E-04	0.9824
H005	2.34	1.05E+05	3.26	6331	3.892E-04	1.233E-04	0.9887
H006	3.28	2.49E+04	4.44	0.351	5.283E-04	2.853E-04	0.8773
H009	1.99	2.98E+04	2.99	2148	2.578E-04	1.771E-04	0.9826
H010	2.05	2.10E+04	2.98	1336	2.284E-04	1.821E-04	0.983
H004b	2.20	7.31E+04	4.38	3948	4.431E-05	5.546E-05	0.9838
H005b	2.46	1.23E+05	5.31	6188	3.492E-05	4.02E-05	0.9873
H010b	2.38	1.59E+05	5.28	4524	3.399E-05	4.858E-05	0.9638

In summary, the Burgers model and Findley's Power Law were used to curve fit the creep data. The models were found to be in good agreement for the data obtained under tensile and compressive loadings. The use of models gives the ability to predict long-term strain values without having to conduct lengthy experiments. The results suggest limitations to the models' accuracy since they do not consider changes in the material such as fibre realignment or strain hardening. Future work could involve the application of the creep data obtained to other models, including finite element models, which do consider these changes.

6.0 Conclusion and Future Work

Polymer composite pipelines are gaining popularity for the advantages they have over steel pipelines such as superior corrosion resistance, higher strength-to-weight ratio and increased flexibility. Advances in materials have allowed composite pipelines to be used in both onshore and deep-sea applications. Composite pipelines can be divided into two categories: thermoplastic and thermoset. Thermoplastic composites are easier to process and exhibit greater toughness and impact resistance compared to their thermoset counterparts. However, thermoplastic composites are more prone to creep. Creep is an important consideration since certain pipelines are expected to have an operating life of 20 years. Despite, the increased use of the material, there is still limited research in the creep behaviour of these materials for pipeline applications; most previous research has focused on flat coupons or thermoset polymer composite pipes.

In the first stage of this study, an industrial filament winding machine was converted to fabricate tubular coupons from glass fibre reinforced high density polyethylene (HDPE) tape. After the development of a repeatable manufacturing process, a creep testing setup was developed to determine the creep behaviour of the material under bi-axial loading conditions.

The study identified critical parameters for the tape winding process: temperature, consolidation pressure and processing speed. Through many experimental trials and continual improvement of the fabrication setup, high-quality, bonded tubular specimens were produced. The quality of the tubes were verified through dimensional measurements, crush tests and analysis of their microstructure.

Creep tests, which ranged from 2 hours to 7 hours in length, were conducted in a tri-axial testing machine. The specimens were tested under comparatively low loads: 10 MPa pure hoop stress followed by 5 MPa pure compressive stress after a resting period. Strain gauges and digital image correlation (DIC) were employed to measure strain during the tests. The material exhibited creep behaviour despite the low loads; however, only the longer tests (4 hours or longer) reached steady state creep. Specimens from different batches displayed noticeably different creep properties but specimens within the same batch had consistent test results to each other. This result suggests that varying manufacturing parameters such as processing temperature affects the material's creep properties. All glass fibre reinforced HDPE specimens demonstrated

improved creep resistance, evaluated by strain rate and creep compliance, compared to creep results of pure HDPE found in literature.

There is good confidence in the accuracy of the strain gauge measurements since they were in good agreement with predicted strain values obtained by Classical Lamination Theory and DIC measurements. Despite agreement with the strain gauges, the DIC measurements experienced greater noise and had a tendency to over predict the hoop strain. However, the creep tests still yielded reliable data which could be used to determine parameters of empirical creep models such as Burgers model and Findley's Power Law.

Burgers model and Findley's Power Law were used to fit results from all creep tests; however, the shorter creep tests did not provide enough data points, which resulted in significant over prediction the strain. It is recommended to only use data from tests that are at least 4 hours in duration to obtain predictions that are more accurate. In comparing the two models, Findley's Power Law provided a closer fit to the creep data than the Burgers model.

The manufacturing and testing process have improved significantly from the beginning of the study but there are still topics for future research. The effect of manufacturing parameters on the mechanical properties of the tubular coupons, such as bond strength or density, can be quantified through additional mechanical tests. Different tape materials can be investigated to demonstrate the versatility of the fabrication setup. In terms of the test setup, the effect of different stress conditions (such as higher loads) on the creep behaviour of the material can be studied. Additionally, the tri-axial testing machine can apply axial and torsional loads simultaneously with internal pressure so this could be an option in the test matrix. In this study, the maximum length of the creep tests were limited since the triaxial testing machine can only be operated during regular working hours; however, future studies could explore the effect of sequential creep tests on the long-term behaviour of the material. The specimen could be tested during the day and then allowed to rest overnight before being subjected to test loads again the next day. This process could be repeated several times to observe the material's creep response after repeated loadings.

Although possible suggestions were provided for the bias in the DIC measurements, it is still unclear the root cause. DIC measurements with greater accuracy would be beneficial since the technique allows for analysis of a larger surface area of the specimen. Lastly, creep data can be used as input to finite element models instead of empirical models. Numerical models would

be able to overcome limitations in the empirical models such as inability to account for fibre realignment.

To summarize, the achievements of the study are the development of a repeatable manufacturing and creep testing process for tubular coupons made from thermoplastic fibre reinforced polymer composites. It will allow experimental creep results to be provided as input to the numerical models developed by the industrial partner. Additionally, it helps lay the foundation for future students to continue thermoplastic composite research at the Advanced Composite Materials and Engineering Group.

Bibliography

[1] Natural Resources Canada, 2016, “Pipelines Across Canada,” Nat. Resour. Canada [Online]. Available: https://www.nrcan.gc.ca/energy/infrastructure/18856. [Accessed: 23-Mar-2019].

[2] Bureau of Transportation, “U.S. Oil and Gas Pipeline Mileage,” Bur. Transp. Stat. [Online]. Available: https://www.bts.gov/content/us-oil-and-gas-pipeline-mileage. [Accessed: 23-Mar-2019].

[3] Green, K., and Jackson, T., 2015, “Safety in the Transportation of Oil and Gas: Pipelines or Rail?,” Fraser Inst., pp. 1–14 [Online]. Available: https://www.fraserinstitute.org/research/safety-transportation-oil-and-gas-pipelines-or-rail. [Accessed: 28-Aug-2019].

[4] Bogner, B. E., 2008, “Large Diameter Composite Pipe: Lasting Function in a World of Growth,” Mater. Today [Online]. Available: https://www.materialstoday.com/composite-applications/features/large-diameter-composite-pipe-lasting-function-in/. [Accessed: 28-Aug-2019].

[5] ASTM International, 2015, “Standard Specification for Glass Fiber Reinforced Thermoplastic Pipe,” F2686.

[6] Gibson, A. G., Hicks, C., Wright, P. N. H., and Fahrer, A., 2014, “Development of Glass Fibre Reinforced Polyethylene Pipes for Pressure Applications,” Plast. Rubber Compos., **29**(10), pp. 509–519.

[7] CAPP, 2017, *Use of Reinforced Composite Pipe (Non-Metallic Pipelines)*, Canada’s Oil & Natural Gas Producers (CAPP).

[8] Ossai, C. I., Boswell, B., and Davies, I. J., 2015, “Pipeline Failures in Corrosive Environments - A Conceptual Analysis of Trends and Effects,” Eng. Fail. Anal., **53**, pp. 36–58.

[9] Alberta Energy Regulator, “Pipeline Performance” [Online]. Available: https://www.aer.ca/protecting-what-matters/holding-industry-accountable/industry-performance/pipeline-performance. [Accessed: 23-Mar-2019].

[10] Koch, G. H., Brongers, M. P. H., Thompson, N. G., Virmani, Y. P., and Payer, J. H., 2002, “Corrosion Costs and Preventive Strategies in the United States,” NACE Int.

[11] Bogner, B. E., “Large Diameter Composite Pipe: Lasting Function in a World of Growth,” Mater. Today [Online]. Available: https://www.materialstoday.com/composite-applications/features/large-diameter-composite-pipe-lasting-function-in/. [Accessed: 23-Mar-2019].

[12] Baxter, L., 2015, “Composite Pipe Applications and Design Factors To Extend System

Life," Flexpipe Syst., pp. 1–17 [Online]. Available: https://www.lbcg.com/media/downloads/events/503/12-00-otto-comin-flexpipe-systems.8597.pdf. [Accessed: 28-Aug-2019].

[13] de Kanter, J. L. C. G., and Leijten, J., 2009, "Thermoplastic Composite Pipe: Analysis and Testing of a Novel Pipe System for Oil & Gas," Proc. 17th ICCM, pp. 1–10.

[14] Composites World, 2016, "The Markets: Oil and Gas (2017)," Compos. World [Online]. Available: https://www.compositesworld.com/articles/the-markets-oil-and-gas-2016. [Accessed: 20-Dec-2017].

[15] Fellet, M., and Nyborg, R., 2018, "Understanding Corrosion of Flexible Pipes at Subsea Oil and Gas Wells," MRS Bull., **43**(9), pp. 654–655.

[16] Shawcor Composite Production Systems, 2017, "FlexFlow Linepipe Produced Water Transfer Line Installation" [Online]. Available: https://www.shawcor.com/about/success-stories/flexflow-linepipe-produced-water-transfer-line-in. [Accessed: 26-Aug-2019].

[17] LeBlanc, J., and Sternisha, M., 2016, "Fiberglass Pipe Is Helping Solve the World's Drinking Water Shortage," Pipelines, pp. 1589–1599.

[18] Rafferty, K. D., 1991, "Piping," *Geothermal Direct-Use Engineering and Design Guidebook*, P. Lienau, and B. Lunis, eds., Oregon Institute of Technology, Oregon, pp. 242–259.

[19] Kaw, A., 2006, *Mechanics of Composite Materials*, Taylor and Francis Group, LLC.

[20] Hamed, A. F., Khalid, Y. A., Sapuan, S. M., Hamdan, M. M., Younis, T. S., and Sahari, B. B., 2007, "Effects of Winding Angles on the Strength of Filament Wound Composite Tubes Subjected to Different Loading Modes," Polym. Polym. Compos., **15**(3), pp. 199–206.

[21] Callister, W., and Rethwisch, D., 2012, *Fundamentals of Material Science and Engineering*, Wiley.

[22] Magma Global Limited, "M-Pipe FAQ" [Online]. Available: https://www.magmaglobal.com/community/faq/. [Accessed: 23-Mar-2019].

[23] Papanicolaou, G.C. Zaoutsos, S. P., 2011, "Viscoelastic Constitutive Modeling of Creep and Stress Relaxation in Polymers and Polymer Matrix Composites," *Creep and Fatigue in Polymer Matrix Composites*, R.M. Guedes, ed., Woodhead Publishing, pp. 3–47.

[24] Yu, K., Morozov, E. V., Ashraf, M. A., and Shankar, K., 2017, "A Review of the Design and Analysis of Reinforced Thermoplastic Pipes for Offshore Applications," J. Reinf. Plast. Compos., **36**(20), pp. 1514–1530.

[25] Yoon, S. H., and Oh, J. O., 2015, "Prediction of Long Term Performance for GRP Pipes under Sustained Internal Pressure," Compos. Struct., **134**, pp. 185–189.

[26] Faria, H., and Guedes, R. M., 2010, "Long-Term Behaviour of GFRP Pipes: Reducing the Prediction Test Duration," Polym. Test., **29**(3), pp. 337–345.

[27] Tuttle, M. E., and Brinson, H. F., 1986, "Prediction of the Long-Term Creep Compliance of General Composite Laminates," Exp. Mech., **26**(1), pp. 89–102.

[28] Rafiee, R., and Mazhari, B., 2015, "Modeling Creep in Polymeric Composites: Developing a General Integrated Procedure," Int. J. Mech. Sci., **99**, pp. 112–120.

[29] Yudhanto, A., Wafai, H., Lubineau, G., Goutham, S., Mulle, M., Yaldiz, R., and Verghese, N., 2019, "Revealing the Effects of Matrix Behavior on Low-Velocity Impact Response of Continuous Fiber-Reinforced Thermoplastic Laminates," Compos. Struct., **210**(September 2018), pp. 239–249.

[30] Schledjewski, R., 2009, " Thermoplastic Tape Placement Process – in Situ Consolidation Is Reachable ," Plast. Rubber Compos., **38**(9–10), pp. 379–386.

[31] Guo, W., Shi, J., Zheng, J., and Liu, Z., 2014, "Research on Ultrasonic Testing for Electro-Fusion Joint of Reinforced Thermoplastic Pipes," *ASME 2014 Pressure Vessels & Piping Conference*, Anaheim, pp. 1–5.

[32] Bengtsson, M., Gatenholm, P., and Oksman, K., 2005, "The Effect of Crosslinking on the Properties of Polyethylene/Wood Flour Composites," Compos. Sci. Technol., **65**(10), pp. 1468–1479.

[33] Green, J. E., 2011, "Automated Filament Winding Systems," *Composite Filament Winding*, S. Peters, ed., pp. 7–18.

[34] Hoa, S. V, 2009, "Filament Winding and Fiber Placement," *Principles of the Manufacturing of Composite Materials*, DEStech Publications, Inc., pp. 205–231.

[35] Henriquez, R., and Mertiny, P., 2018, "Comprehensive Composite Materials II," *Comprehensive Composite Materials II*, C. Zweben, and P. Beaumont, eds., Elsevier Ltd., pp. 557–577.

[36] Roychowdhury, S., and Advani, S. G., 1991, "An Experimental Investigation of Consolidation in Thermoplastic Filament Winding," Compos. Manuf., **2**(2), pp. 97–104.

[37] Mclarty, J. L., 2011, "Control of Filament Winding Parameters," *Composite Filament Winding*, S. Peters, ed., ASM International, pp. 65–79.

[38] Ghasemi Nejhad, M. N., Cope, R. D., and Güçeri, S. I., 2008, "Thermal Analysis of In-Situ Thermoplastic-Matrix Composite Filament Winding," J. Heat Transfer, **113**(2), p. 304.

[39] Stokes-Griffin, C. M., and Compston, P., 2016, "An Inverse Model for Optimisation of Laser Heat Flux Distributions in an Automated Laser Tape Placement Process for Carbon-Fibre/PEEK," Compos. Part A Appl. Sci. Manuf., **88**, pp. 190–197.

[40] Stokes-Griffin, C. M., and Compston, P., 2015, "The Effect of Processing Temperature and Placement Rate on the Short Beam Strength of Carbon Fibre-PEEK Manufactured Using a Laser Tape Placement Process," Compos. Part A Appl. Sci. Manuf., **78**, pp. 274–283.

[41] Buijs, J. A. H. M., and Nederveen, P. J., 1992, "A Study of Consolidation in Filament Winding with Thermoplastic Prepregs," J. Thermoplast. Compos. Mater., **5**(4), pp. 276–286.

[42] Wang, X., Weber, M. E., and Charrier, J. M., 1989, "Heating of Thermoplastic-Based Unidirectional Composite Prepregs," J. Thermoplast. Compos. Mater., **2**(2), pp. 105–121.

[43] Colton, J., and Leach, D., 1992, "Processing Parameters for Filament Winding Thick-Section PEEK/ Carbon Fiber Composites," Polym. Compos., **13**(6), pp. 427–434.

[44] Tannous, M., Barasinski, A., Binetruy, C., and Courtemanche, B., 2016, "Contribution of Thermo-Mechanical Parameters and Friction to the Bonding of Thermoplastic Tapes in the Tape Winding Process," J. Mater. Process. Technol., **229**, pp. 587–595.

[45] Dell'Anna, R., Lionetto, F., Montagna, F., and Maffezzoli, A., 2018, "Lay-up and Consolidation of a Composite Pipe by in Situ Ultrasonicwelding of a Thermoplastic Matrix Composite Tape," Materials (Basel)., **11**(5).

[46] Beyeler, E., Phillips, W., and Güçeri, S. I., 1988, "Experimental Investigation of Laser-Assisted Thermoplastic Tape Consolidation," J. Thermoplast. Compos. Mater., **1**(1), pp. 107–121.

[47] Quadrini, F., Squeo, E. A., and Prosperi, C., 2010, "Diode Laser Assisted Filament Winding of Thermoplastic Matrix Composites," Materials (Basel)., **3**(1), pp. 563–571.

[48] Agarwal, V., Mccullough, R. L., and Schultz, J. M., 1996, "The Thermoplastic Laser-Assisted Consolidation Process - Mechanical and Microstructure Characterization," J. Thermoplast. Compos. Mater., **9**(4), pp. 365–380.

[49] ASTM International, 2016, "Standard Test Method for Short-Beam Strength of Polymer Matrix Composite Materials and Their Laminates," D2344.

[50] Mazumdar, S. K., and Hoa, S. V., 1996, "Determination of Manufacturing Conditions for Hot-Gas-Aided Thermoplastic Tape Winding," J. Thermoplast. Compos. Mater., **9**(1), pp. 35–53.

[51] ASTM International, 2016, "Standard Test Methods for Void Content of Reinforced Plastics," D2734.

[52] ASTM International, 2013, "Standard Test Methods for Density and Specific Gravity (Relative Density) of Plastics by Displacement," ASTM D792.

[53] Mason, K., 2019, "Thermoplastic Composite Pipe on the Rise in the Deep Sea," Compos.

World, pp. 16–19.

[54] Alger, M., 2017, *Polymer Science Dictionary*, Springer Netherlands.

[55] Brauner, C., Herrmann, A. S., Niemeier, P. M., and Schubert, K., 2017, "Analysis of the Non-Linear Load and Temperature-Dependent Creep Behaviour of Thermoplastic Composite Materials," J. Thermoplast. Compos. Mater., **30**(3), pp. 302–317.

[56] Ebewele, R. O., 2000, *Polymer Science and Technology*, CRC Press LLC.

[57] Lakes, R., 2009, "Viscoelastic Composite Materials," Viscoelastic Mater., (May), pp. 341–376.

[58] Ashby, M. F., and Jones, D. R. H., 2012, *Engineering Materials 1 - An Introduction to Properties, Applications, and Design*, Elsevier.

[59] Findley, William N. Lai, James S. Onaran, K., 1976, *Creep and Relaxation of Nonlinear Viscoelastic Materials - With an Introduction to Linear Viscoelasticity*, Dover Publications.

[60] Brinson, H. F., and Brinson, L. C., 2015, *Polymer Engineering Science and Viscoelasticity*, Springer.

[61] Scott, D. W., Lai, J. S., and Zureick, A.-H., 1995, "Creep Behavior of Fiber-Reinforced Polymeric Composites: A Review of the Technical Literature," J. Reinf. Plast. Compos., **14**(6), pp. 588–617.

[62] ISO International, 2003, "Plastics - Determination of Creep Behaviour (Part 2: Flexural Creep by Three-Point Bending)," ISO 899-2, pp. 1–20.

[63] ISO International, 2015, "Plastics Piping Systems — Glassreinforced Thermosetting Plastics (GRP) Pipes — Determination of Time to Failure under Sustained Internal Pressure," ISO 7509.

[64] ISO International, 1997, "Plastics Piping Systems - Glass-Reinforced Thermosetting Plastics (GRP) Pipes - Determination of the Creep Factor under Dry Conditions," ISO 7684, pp. 1–14.

[65] P.V. Vlasov, G.G. Gusev, D.F. Kagan, I.Ya. Klinov, A. V. M., 1967, "Carrying Capacity and Deformation Properties of Glass-Reinforced Plastic Pipes of Various Construction," Mekhanika Polim., **3**(6), pp. 1082–1088.

[66] Ghorbel, I., 1996, "Durability of Closed-End Pressurized GRP Filament Wound Pipes under Hygrothermal Aging Conditions. Part II: Creep Tests," J. Compos. Mater., **30**(14), pp. 1581–1595.

[67] Ghorbel, I., and Spiteri, P., 1996, "Durability of Closed-End Pressurized GRP Pipes under Hygrothermal Conditions. Part I: Monotonic Tests," J. Compos. Mater., **30**(14), pp. 1562–

1580.

[68] Yao, J., and Ziegmann, G., 2006, “Equivalence of Moisture and Temperature in Accelerated Test Method and Its Application in Prediction of Long-Term Properties of Glass-Fiber Reinforced Epoxy Pipe Specimen,” Polym. Test., **25**(2), pp. 149–157.

[69] Xian, G., Wu, J., Li, H., Yang, Y., Hamada, H., and Fukui, E., 2013, “Hygrothermal Ageing and Creep Behavior of Glass Fiber Reinforced Polymer Composites,” *19th International Conference on Composite Materials*, Montreal, pp. 1–8.

[70] Yang, Z., Wang, H., Ma, X., Shang, F., Ma, Y., Shao, Z., and Hou, D., 2018, “Flexural Creep Tests and Long-Term Mechanical Behavior of Fiber-Reinforced Polymeric Composite Tubes,” Compos. Struct., **193**(January), pp. 154–164.

[71] Fliegener, S., Hohe, J., and Gumbsch, P., 2016, “The Creep Behavior of Long Fiber Reinforced Thermoplastics Examined by Microstructural Simulations,” Compos. Sci. Technol., **131**, pp. 1–11.

[72] Xiao, X., 1989, “Studies of the Viscoelastic Behaviour of a Thermoplastic Resin Composite,” Compos. Sci. Technol., **34**(2), pp. 163–182.

[73] Nguyen, D. H., and Ogale, A. A., 1991, “Compressive and Flexural Creep Behavior of Carbon Fiber/PEEK Composites,” J. Thermoplast. Compos. Mater., **4**(January), pp. 83–99.

[74] ISO International, 2017, “Plastics - Determination of Creep Behaviour - Part 1: Tensile Creep,” ISO 899-1, pp. 1–20.

[75] Kruijer, M. P., Warnet, L. L., and Akkerman, R., 2006, “Modelling of the Viscoelastic Behaviour of Steel Reinforced Thermoplastic Pipes,” Compos. Part A Appl. Sci. Manuf., **37**(2), pp. 356–367.

[76] Mittelstedt, C., and Becker, W., 2007, “Free-Edge Effects in Composite Laminates,” Appl. Mech. Rev., **60**(5), p. 217.

[77] Funck, R., and Neitzel, M., 1995, “Improved Thermoplastic Tape Winding Using Laser or Direct-Flame Heating,” Compos. Manuf., **6**(3–4), pp. 189–192.

[78] Khashaba, U. A., 2004, “In-Plane Shear Properties of Cross-Ply Composite Laminates with Different off-Axis Angles,” Compos. Struct., **65**(2), pp. 167–177.

[79] Kugler, D., and Moon, T. J., 2002, “The Effects of Mandrel Material and Tow Tension on Defects and Compressive Strength of Hoop-Wound, on-Line Consolidated, Composite Rings,” Compos. - Part A Appl. Sci. Manuf., **33**(6), pp. 861–876.

[80] Micro-measurements, 2010, “Optimizing Strain Gage Excitation Levels,” Tech Note TN-502, pp. 11–18 [Online]. Available: http://www.vishaypg.com/docs/11052/tn502.pdf. [Accessed: 28-Aug-2019].

[81] National Instruments, 1998, “Application Note 078 - Strain Gauge Measurements,” (August), p. 12 [Online]. Available: http://elektron.pol.lublin.pl/elekp/ap_notes/NI_AN078_Strain_Gauge_Meas.pdf. [Accessed: 28-Aug-2019].

[82] Sause, M., 2016, *In Situ Monitoring of Fiber-Reinforced Composites*, Springer.

[83] Correlated Solutions, 2016, “Minimizing Noise and Bias in 3D DIC: Overview of Noise and Bias,” Correl. Solut. Knowledgebase, pp. 1–86 [Online]. Available: http://www.correlatedsolutions.com/supportcontent/dic-noise-bias.pdf. [Accessed: 28-Aug-2019].

[84] Correlated Solutions, 2016, “Strain Calculation in Vic-3D,” Correl. Solut. Knowledgebase, pp. 1–4 [Online]. Available: http://www.correlatedsolutions.com/supportcontent/strain.pdf. [Accessed: 28-Aug-2019].

[85] Correlated Solutions, 2017, “Application Note AN -1701 Speckle Pattern Fundamentals,” Speckle Pattern Fundam., pp. 1–13 [Online]. Available: https://www.correlatedsolutions.com/support/index.php?/Knowledgebase/Article/View/80/1/speckle-pattern-fundamentals. [Accessed: 28-Aug-2019].

[86] Simonsen, M., 2016, “Heat Waves in Digital Image Correlation,” Correl. Solut. Knowledgebase [Online]. Available: https://www.correlatedsolutions.com/support/index.php?/Knowledgebase/Article/View/5/1/heat-waves-in-digital-image-correlation. [Accessed: 28-Aug-2019].

[87] Behjat, Y., Cheng, J. J., Polak, M. A., Asce, M., and Penlidis, A., 2014, “Effect of Molecular Structure on the Short-Term and Long-Term Mechanical Behavior of High-Density Polyethylene,” **26**(May), pp. 795–802.

[88] Vullo, V., 2014, “Thin-Walled Circular Cylinders Under Internal and/or External Pressure and Stressed in the Linear Elastic Range,” *Circular Cylinders and Pressure Vessels: Stress Analysis and Design*, Springer International Publishing, Cham, pp. 1–22.

[89] Barkoula, N. M., Alcock, B., van Erp, T. B., Govaert, L. E., and Peijs, T., 2018, “Nonlinear Creep Response of Oriented Polypropylene Tapes,” Proc. Inst. Mech. Eng. Part L J. Mater. Des. Appl., **232**(12), pp. 987–992.

[90] Montero, W., Farag, R., Díaz, V., Ramirez, M., and Boada, B. L., 2011, “Uncertainties Associated with Strain-Measuring Systems Using Resistance Strain Gauges,” J. Strain Anal. Eng. Des., **46**(1), pp. 1–13.

[91] Mertiny, P., and Ellyin, F., 2006, “Joining of Fiber-Reinforced Polymer Tubes for High-Pressure Applications,” Polym. Compos., **27**(1), pp. 99–109.

[92] Moghadamzadeh, H., Rahimi, H., Asadollahzadeh, M., and Hemmati, A. R., 2011, “Surface Treatment of Wood Polymer Composites for Adhesive Bonding,” Int. J. Adhes. Adhes., **31**(8), pp. 816–821.

[93] Vishay, 2014, “AN B-129-8 - Surface Preparation for Strain Gage Bonding,” MicroMeasurements, (11129), pp. 1–8 [Online]. Available: http://www.vishaypg.com/docs/11129/11129B129.pdf. [Accessed: 28-Aug-2019].

[94] Micro-measurements, V., 2014, “CEA Strain Gage Installation with M-Bond 200 Adhesive (Training Video)” [Online]. Available: https://www.youtube.com/watch?v=SjXpF61HRys. [Accessed: 01-Nov-2018].

[95] Simonsen, M., 2016, “Projection Error: Explanation and Causes,” Correl. Solut. Knowledgebase [Online]. Available: https://www.correlatedsolutions.com/support/index.php?/Knowledgebase/Article/View/1/1/projection-error-explanation-and-causes. [Accessed: 27-Aug-2019].

[96] Clancy, G., Peeters, D., Oliveri, V., Jones, D., O’Higgins, R. M., and Weaver, P. M., 2019, “A Study of the Influence of Processing Parameters on Steering of Carbon Fibre/PEEK Tapes Using Laser-Assisted Tape Placement,” Compos. Part B Eng., **163**(October 2018), pp. 243–251.

[97] Kim, B. C., Potter, K., and Weaver, P. M., 2012, “Continuous Tow Shearing for Manufacturing Variable Angle Tow Composites,” Compos. Part A Appl. Sci. Manuf., **43**(8), pp. 1347–1356.

[98] Raj, P. P., and Ramasamy, V., 2012, *Strength of Materials*, New Delhi: Dorling Kindersley.

[99] Roy, A. K., and Tsai, S. W., 2009, “Design of Thick Composite Cylinders,” J. Press. Vessel Technol., **110**(3), p. 255.

[100] “A-Glass Fiber, Generic,” MatWeb Mater. Prop. Data [Online]. Available: http://www.matweb.com/search/DataSheet.aspx?MatGUID=8f9003366c9044bdb91bcd86e1fa6e42. [Accessed: 28-Aug-2019].

[101] Roychowdhury, S., Gillespie, J. W., and Advani, S. G., 1992, “Void Formation and Growth in Thermoplastic Processing,” *Computer Aided Design in Composite Material Technology III*, S.G. Advani, W.R. Blain, W.P. de Wilde, J.W. Gillespie, and O.H. Griffin, eds., Springer Netherlands, Dordrecht, pp. 89–107.

[102] “Overview of Materials for High Density Polyethylene (HDPE), Pipe Grade,” MatWeb (Material Prop. Data) [Online]. Available: http://www.matweb.com/search/DataSheet.aspx?MatGUID=c305addb2e1c4a58a3dece14122acfde. [Accessed: 28-Aug-2019].

[103] Xia, X. C., Zhang, Q. P., Wang, L., Feng, J. M., Fu, X. R., and Yang, M. B., 2014, “Role of Gas Cooling Time on Crystalline Morphology and Mechanical Property of the HDPE Parts Prepared by Gas-Assisted Injection Molding,” Colloid Polym. Sci., **292**(5), pp. 1129–1142.

[104] Peel, L. D., 2005, “Investigation of High and Negative Poisson’s Ratio Laminates,” Proc.

Int. SAMPE Symp. Exhib., **50**(January 2005), pp. 821–834.

[105] Kaddour, A. S., Hinton, M. J., and Soden, P. D., 2003, "Behaviour of ±45° Glass/Epoxy Filament Wound Composite Tubes under Quasi-Static Equal Biaxial Tension-Compression Loading: Experimental Results," Compos. Part B Eng., **34**(8), pp. 689–704.

[106] Al-Salehi, F. A. R., Al-Hassani, S. T. S., and Hinton, M. J., 1989, "An Experimental Investigation into the Strength of Angle Ply GRP Tubes under High Rate of Loading," J. Compos. Mater., **23**(3), pp. 288–305.

[107] Liang, Y., Wang, H., and Gu, X., 2013, "In-Plane Shear Response of Unidirectional Fiber Reinforced and Fabric Reinforced Carbon/Epoxy Composites," Polym. Test., **32**(3), pp. 594–601.

[108] Rosenow, M. W. ., 1984, "Wind Angle Effects in Glass Fibre-Reinforced Polyester Filament Wound Pipes," Composites, **15**(2), pp. 144–152.

[109] Nomula, S. S. R., Rathore, D. K., Ray, B. C., and Prusty, R. K., 2019, "Creep Performance of CNT Reinforced Glass Fiber/Epoxy Composites: Roles of Temperature and Stress," J. Appl. Polym. Sci., **136**(25), pp. 1–15.

[110] Mathers, G., "Creep and Creep Testing," Weld. Inst. [Online]. Available: https://www.twi-global.com/technical-knowledge/job-knowledge/creep-and-creep-testing-081. [Accessed: 13-Jun-2019].

[111] Elleuch, R., and Taktak, W., 2006, "Viscoelastic Behavior of HDPE Polymer Using Tensile and Compressive Loading," J. Mater. Eng. Perform., **15**(1), pp. 111–116.

[112] Elghazouli, A. Y., Chryssanthopoulos, M. K., and Spagnoli, A., 1999, "Experimental Response of Glass-Reinforced Plastic Cylinders under Axial Compression," Mar. Struct., **11**(9), pp. 347–371.

[113] Pereira, A. A. C., D'Almeida, J. R. M., and Castro, T. M. L., 2018, "Evaluation of Short-Term Creep Behavior of PE-HD after Aging in Oil Derivatives," Polym. Polym. Compos., **26**(3), pp. 243–258.

[114] Mertiny, P., 2009, "Pvp2009-77522 Analysis of Surface Strains and Leakage Behavior in Composite Pipes And," pp. 1–7.

[115] Lyons, J. S., Liu, J., and Sutton, M. A., 1996, "High-Temperature Deformation Measurements Using Digital-Image Correlation," Exp. Mech., **36**(1), pp. 64–70.

[116] "Optical Constants of Plastics (PC - Polycarbonate)," Database, Refract. Index [Online]. Available: https://refractiveindex.info/?shelf=3d&book=plastics&page=pc%0A. [Accessed: 03-May-2019].

[117] "Optical Constants of BK7 N-BK7 (SCHOTT)," Refract. Index Database [Online]. Available: https://refractiveindex.info/?shelf=glass&book=BK7&page=SCHOTT.

[Accessed: 03-May-2019].

[118] Byrne, E., and Simonsen, M., 2016, “Viewing Through a Window,” Correl. Solut. Knowledgebase [Online]. Available: http://correlatedsolutions.com/support/index.php?/Knowledgebase/Article/View/49/0/viewing-through-a-window. [Accessed: 24-Mar-2019].

[119] Byrne, E., and Simonsen, M., 2016, “Lens Selection and Stereo Angle,” Correl. Solut. Knowledgebase [Online]. Available: http://www.correlatedsolutions.com/support/index.php?/Knowledgebase/Article/View/50/1/lens-selection-and-stereo-angle. [Accessed: 25-Sep-2019].

[120] Xu, Y., Wu, Q., Lei, Y., and Yao, F., 2010, “Creep Behavior of Bagasse Fiber Reinforced Polymer Composites,” Bioresour. Technol., **101**(9), pp. 3280–3286.

[121] Xu, H. L., Cao, Y., Wang, W. H., and Wang, Q. W., 2016, “Creep Model of Natural Fiber Reinforced Polymer Composite,” Mater. Sci. Forum, **850**, pp. 86–90.

[122] Wang, W.-H., Huang, H.-B., Du, H.-H., and Wang, H., 2015, “Effects of Fiber Size on Short-Term Creep Behavior of Wood Fiber HDPE Composites,” Polym. Eng. Sci.

[123] Findley, W. N., and Khosla, G., 1955, “Application of the Superposition Principle and Theories of Mechanical Equation of State, Strain, and Time Hardening to Creep of Plastics under Changing Loads,” J. Appl. Phys., **26**(7), pp. 821–832.

[124] Findley, W. N., and Tracy, J. F., 1974, “16-Year Creep of Polyethylene and PVC,” Polym. Eng. Sci., **14**(577–580).

Appendix A: Procedure to Bond End Fittings

Bonding of the end fittings to the specimen is completed in the fume hood due to the chemicals involved. The materials required for the procedure are summarized in Figure 64 and Table 12. Prior to assembly, the base of the alignment jig is coated with a mold release agent (MAC-860, McLube, Aston, PA, United States) and the end fittings are cleaned. Cleaning the mating surfaces of the end fittings is a two-step process. First, wet scrubbing with Scotch-Brite abrasive pads (3M, Maplewood, MN, United States) and acetone is used to remove coarse residue. The mating surfaces are then wiped with acetone-soaked paper towels until no residue on the paper towel is observed. The inner sleeve followed by the outer flange is slid down onto the alignment jig as shown in Figure 65-1 and Figure 65-2, respectively. A two part (2:1 ratio) epoxy adhesive (DP460, 3M, Maplewood, MN, Unite States) is injected into the cavity between the outer flange and inner sleeve using an applicator gun (EPX Plus II,3M, Maplewood, MN, United States) as shown in Figure 65-3. Six full pumps of the applicator are required to fill the cavity.

Due to the difficulty of bonding to HDPE, the surface of the tube has to be cleaned and flame treated to promote bonding before insertion into the end fitting assembly. The outside and inside surface at the end of the tube is cleaned with acetone; cleaning of its midsection is avoided to preserve the strain gauge location markings. For flame treatment, the specimen is placed on a level surface while a handheld propane torch (Bernzomatic, Columbus, OH, United States) is angled toward its surface as shown in Figure 65-4. The tube is rotated slowly to allow the flame to touch along its circumference. The treatment is applied to an area up to approximately 25.4 mm from one end. The process continues until the surface obtains a glazed appearance. After surface treatment, the tube is inserted into the adhesive-filled cavity as shown in Figure 65-5. Excess epoxy is wiped away with paper towels; however a fillet is allowed to form to reduce the stress concentration at the transition from end fitting to specimen. The second inner sleeve and alignment spacer is installed into the top end of the tube as shown in Figure 65-6 to ensure the vertical alignment of the tube. The second outer flange is placed on top of the assembly to act as a weight. The weight ensures the tube is uniformly pressed up against the surface of the inner sleeve. The tube is rotated inside the cavity to align the pencil marking line with the middle of a bolt hole on the outer flange as indicated by the red line in Figure 65-7. Aligning the strain gauge location line with the bolt hole allows for consistent orientation of the specimen once it is

installed in the testing machine. The assembly remains in the fume hood overnight to allow the epoxy to cure. The process is repeated to install the second set of end fittings onto the other end of the tube. The combined mass of the inner sleeve and outer flange is 1.28 kg; this weight is considered insignificant compared to the test loads and is hypothesized to cause negligible creep in the specimen.

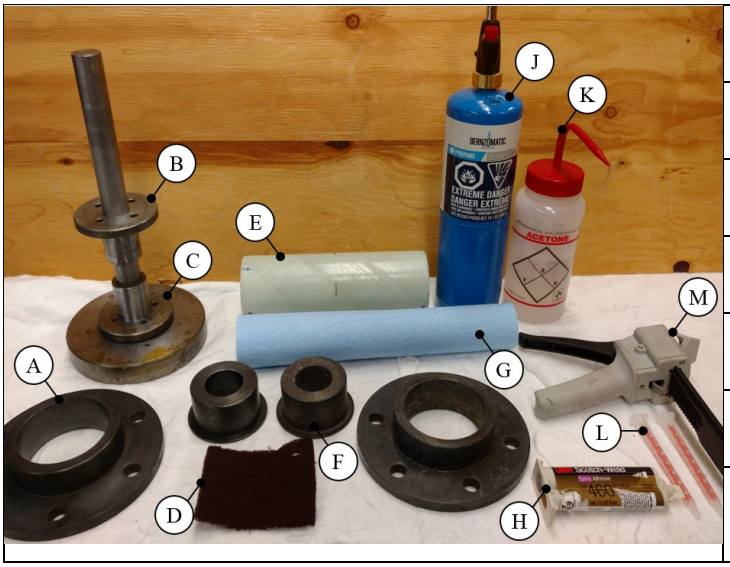

Figure 64: Materials for end fitting installation

Table 12: Materials for end fitting installation

(A) Outer flange (x2)	(G) Paper towels
(B) Alignment spacer	(H) 3M DP460 adhesive
(C) Alignment jig	(J) Propane torch
(D) Scotch-Brite pads	(K) Acetone
(E) Specimen	(L) 2:1 nozzles (x2)
(F) Inner sleeve (x2)	(M) Applicator gun

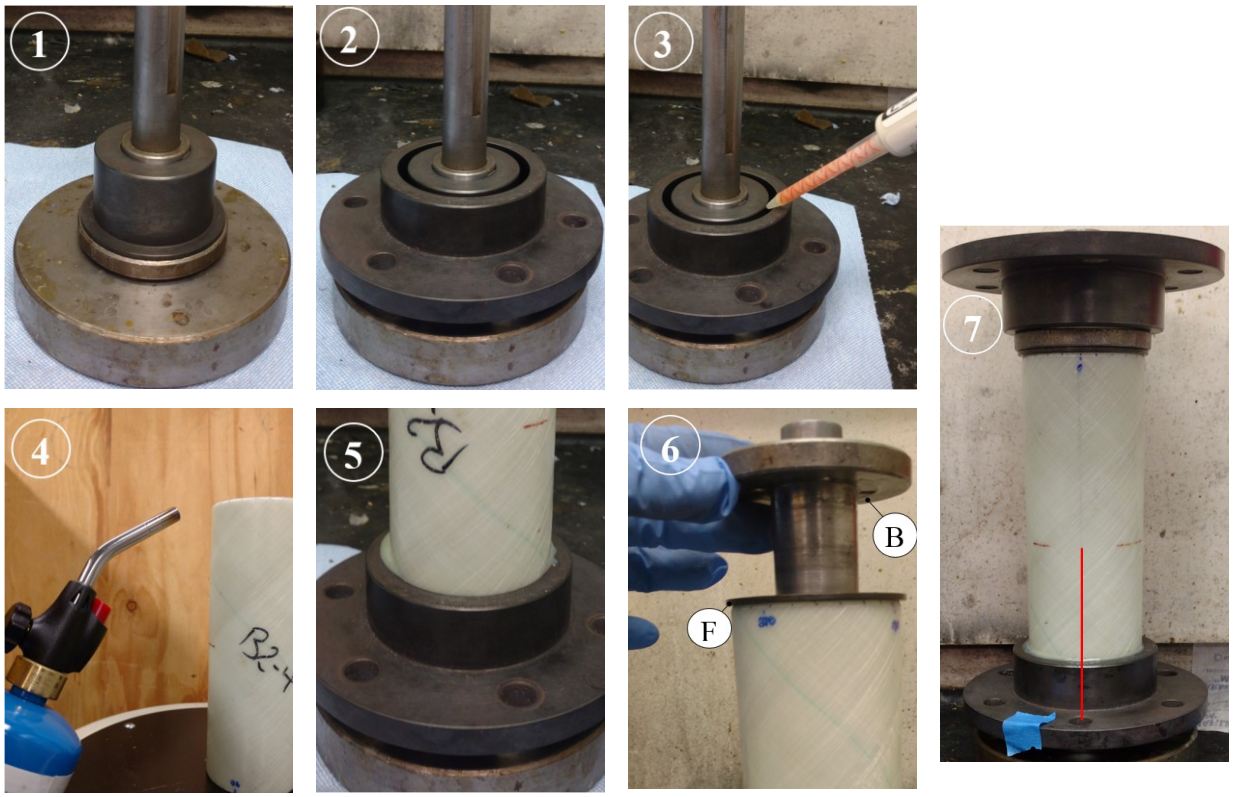

Figure 65-1 to Figure 65-7: Procedure for installing first end fitting

Appendix B: Procedure to Apply Strain Gauges

Figure 66 and Table 13 show the materials required for applying the strain gauge. All steps involving isopropanol alcohol (IPA) or adhesive are completed in the fume hood. While in the fume hood, a glass pane is wiped with IPA and then dried with lint-free gauze. A strain gauge is removed from the package using tweezers and placed gauge side up on the glass. A strip of tape is dispensed, and one end section of the tape is folded onto itself. This provides an easy section to lift the tape off the glass pane. The tape is aligned so the width of the tape covers the strain gauge as shown in Figure 67-1. The tape is pressed down and rubbed on the strain gauge to ensure a close seal. The glass pane with strain gauge is then removed from the fume hood. The strain gauge application area on the specimen is wiped with IPA-soaked gauze as shown in Figure 67-2; the wiping direction is kept constant to avoid introducing contaminants into the treated area. A crosshatch pattern is applied to the surface of the specimen with 400-grit sandpaper as shown in Figure 67-3. The sandpaper is rubbed at +45° and then -45° to the axis of the tube. The surface is wiped again with IPA-soaked gauze and rinsed with water. Gauze is used to dry the treated area as shown in Figure 67-4. Once surface preparation is complete, the midline markings on the strain gauge are aligned with the location lines drawn on the specimen. The strain gauge is oriented for its soldering tabs to be pointing upwards and the blue tape applied during end fitting installation to be to the right as shown in Figure 67-5. Applying the strain gauge in this orientation allows the strain gauge lead wires to be consistently pointing upwards when the specimen is installed in the testing machine. A protractor, as shown in Figure 67-6, is used to confirm the alignment of the strain gauge before adhesive is applied. The specimen is placed back into the fume hood and the tape holding the strain gauge is peeled back approximately 25.4 mm from the edge of the strain gauge as demonstrated in Figure 67-7. Two wipes of the primer (SF-770, Loctite, Düsseldorf, Germany) is applied to the back of the strain gauge; the applicator brush is allowed to extend past the edges of the strain gauge and apply primer to the tape as well. The primer is allowed to air-dry for 3 minutes. A pea-sized drop of cyanoacrylate instant adhesive (Loctite 454, Loctite, Düsseldorf, Germany) is applied to the area where the tape makes contact with the specimen's surface as shown in Figure 67-8. While holding a piece of gauze, the tape and strain gauge are firmly pressed back onto the specimen; excess adhesive is squeezed out and removed by the gauze. The ball of the thumb is used to

apply firm pressure to the strain gauge, as shown in Figure 27-9, for 10 minutes. Cyanoacrylate adhesives require heat and moisture to cure. Due to the lower humidity (approximately 13%) and temperature in the lab the firm pressure is applied for a longer period of time than manufacturer recommendations. The specimen is allowed to rest for 1 hour before the tape is removed.

Soldering of the lead wires to the strain gauge is completed using 60/40 tin/lead 20 AWG solder wire (SMD2SW.031, ChipQuik Ltd., Ancaster, ON, CA). The soldering iron (WES51, Weller, Besigheim, DE) temperature is set to 600°F (316°C). The lead wire arrangement is shown in Figure 68. To check for proper soldering of the strain gauge, the lead wires are connected to the dummy gauge and a voltmeter. The specimen is oriented vertically and then a weight is placed on top of it. The resulting change in voltage on the voltmeter is observed. The compressive load from the weight will cause a negative and positive change in voltage for the hoop and axial directions, respectively. The same weight is used for each specimen so the voltage change will be consistent.

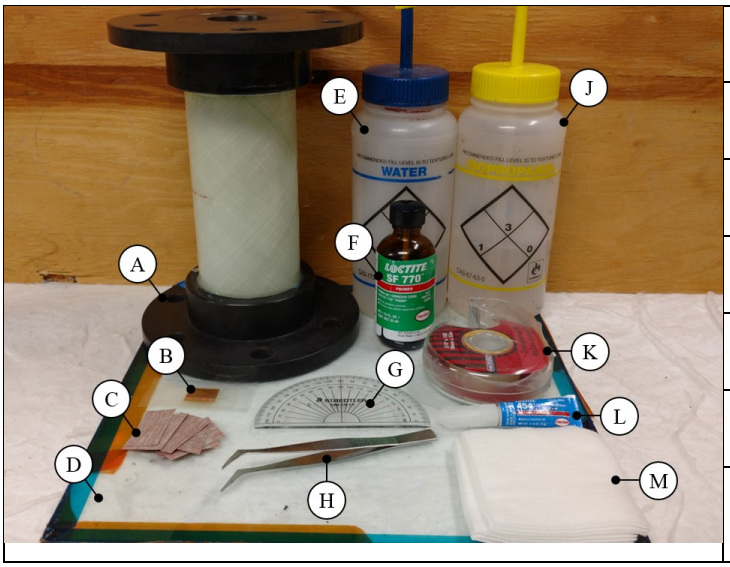

Figure 66: Materials for strain gauge application

Table 13: Materials for strain gauge application

(A) Specimen	(G) Clear protractor
(B) Strain gauge	(H) Tweezers
(C) 400 grit sandpaper	(J) Isopropanol alcohol
(D) Glass pane	(K) Tape
(E) Water	(L) Loctite 454 adhesive
(F) SF-770 primer	(M) Lint-free gauze

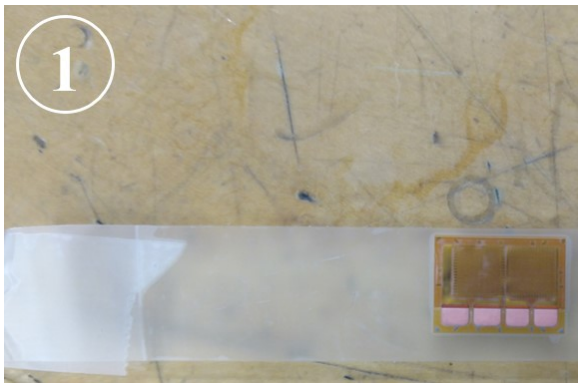
1


2
ISOPROPANOL
3

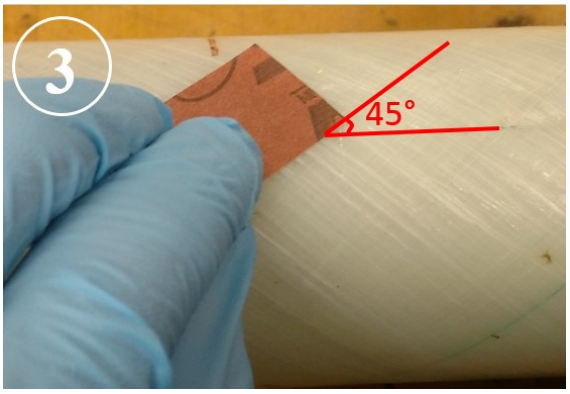
3
45°

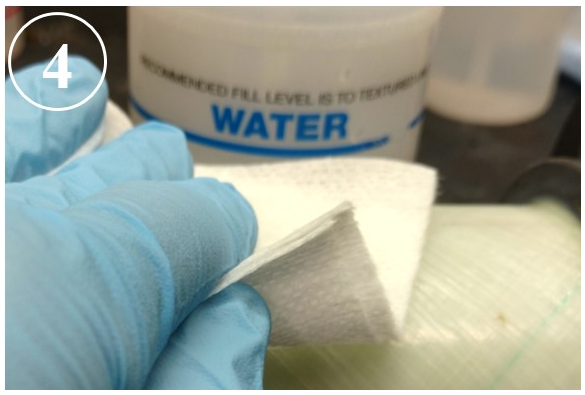
4
WATER

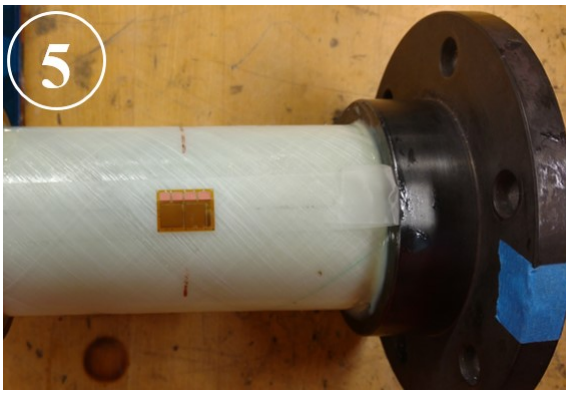
5


6
STAEDTLER
568 50-10

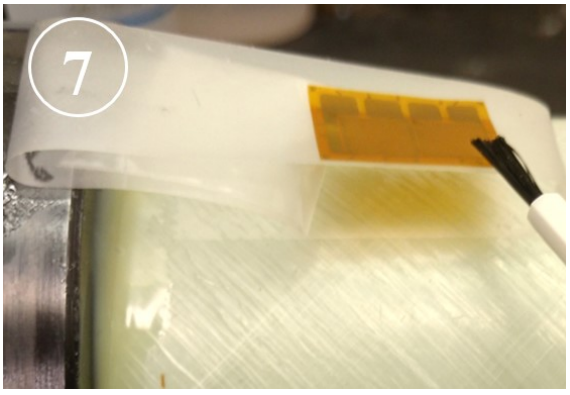
7

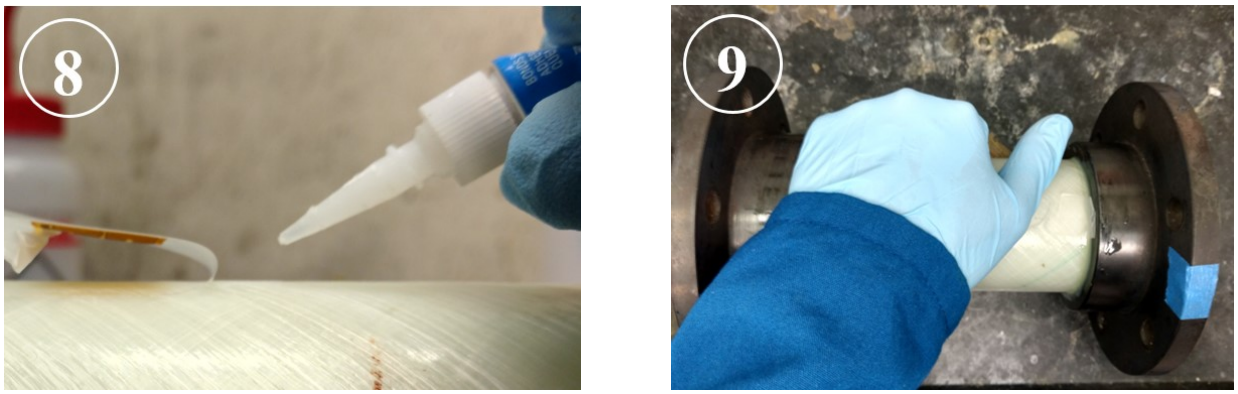

Figure 67-1 to Figure 67-9: Procedure for strain gauge application

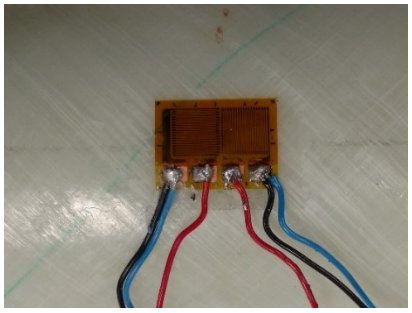

Figure 68: Wire configuration for strain gauge

Appendix C: Procedure to Apply Speckle Pattern for DIC

The procedure for applying the DIC speckle pattern is completed in the fume hood. Figure 69 and Table 14 show the materials used in applying the speckle pattern for DIC. Prior to speckle pattern application, the end fittings and strain gauge lead wires are masked off using plastic wrap and masking tape as shown in Figure 70-1. Cardboard is used to form a screen to minimize the paint spatter on the fume hood walls. The specimen is placed on a raised block, 11.7 cm high, with the strain gauge facing outwards as shown in Figure 70-2. The specimen is rotated approximately 15° counterclockwise; the specimen to be in the same orientation it will be when installed in the testing machine. Resting the specimen on the blocks allows the strain gauge to be approximately level with the nozzle of the paint spray can when the can is placed on the surface of the fume hood. A layer of matte white paint (Spectra, Queensburgh, South Africa) is applied to the specimen as demonstrated in Figure 70-3. The matte black paint can (Rust-Oleum Corp, Vernon Hills, IL, United States) is shaken and two sprays of the can is completed to clear any clogs in the nozzle. A custom-made paint tool is used to provide fine control of the application pressure on the paint can nozzle. Rotation of the knob on the paint tool causes the lever arm to lower and apply pressure on the nozzle. The opening of the nozzle is aligned with the lever arm of the paint tool and a plastic shim is placed between the nozzle and the lever arm to better distribute the pressure. The spray can is placed approximately 152 mm (6 inches) away from the surface of the specimen as shown in Figure 70-4. The opening of the nozzle is angled to the left of the specimen to avoid accidentally spraying the specimen with too much paint. The knob is rotated slowly, as shown in Figure 70-5, until a slow, intermittent hissing is heard, signaling the release of paint. The paint can is rotated towards the right of the specimen for paint speckles to cover the surface. Multiple passes are completed as required to adequately cover the specimen. The specimen is turned upside down and a second series of spraying is completed. Figure 70-6 shows a completed speckle pattern.

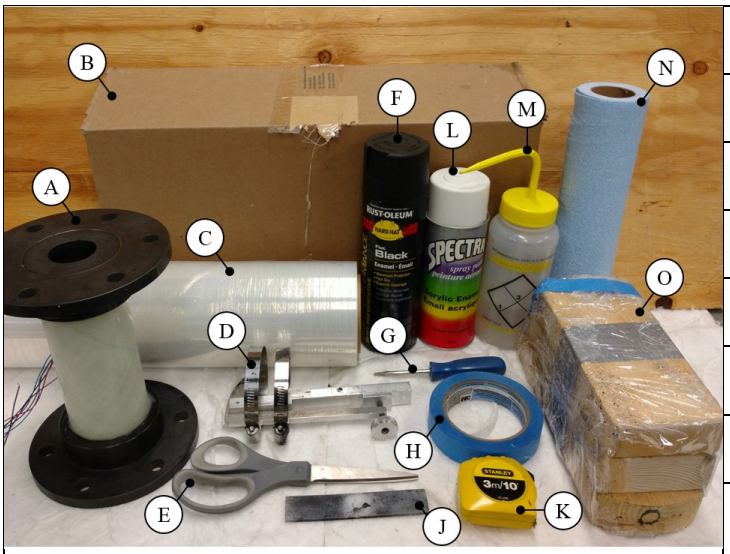

Table 14: Materials for applying speckle pattern	
(A) Specimen	(H) Masking tape
(B) Cardboard	(J) Shim
(C) Plastic wrap	(K) Measuring tape
(D) Paint tool	(L) White spray paint
(E) Scissors	(M) ISO alchohol
(F) Black spray paint	(N) Paper towel
(G) Flat-head screwdriver	(O) Blocks

Figure 69: Materials for applying speckle pattern

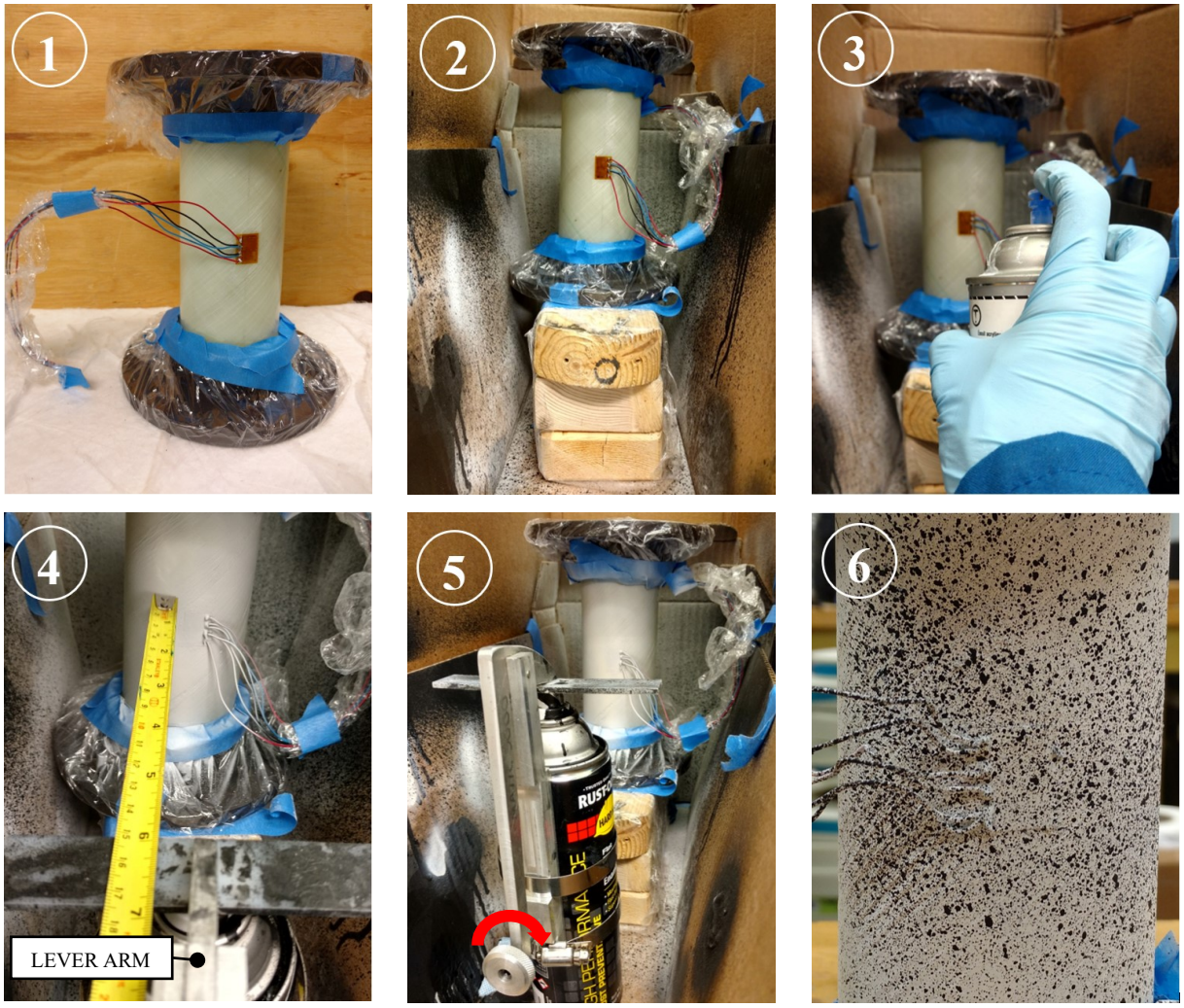

Figure 70-1 to Figure 70-6: Procedure for applying speckle pattern

Appendix D: Procedure to Calibrate DIC System

The quality of the speckle is confirmed before each creep test. The specimen is installed into the tri-axial testing machine, with the speckle pattern facing the cameras, and held in place using one hex bolt. The quality check involves taking a picture of the speckle pattern of the specimen in the testing machine and seeing the projection error between the two cameras reported by the DIC system. The lenses' minimum focusing distance, as measured from the camera body to the specimen, is 80 cm. Therefore, cameras are set at 78.5 cm from the specimen, measured from the front of the lenses. The cameras lenses are adjusted to f50mm and an aperture of f3.5. The right camera, as viewed from behind the tripod and facing the specimen, is positioned to point straight ahead while the second camera is adjusted to allow an angle of 4° between the cameras. The lenses are adjusted to focus on the specimen's speckle pattern. The fine focus dial for the right camera is set to 0.8m and the coarse focus is adjusted until the speckles are in focus. Both the fine and coarse focus of the angled camera is adjusted until maximum focus is achieved. A polycarbonate shield is used as safety precaution in case of specimen failure. The shield is now installed over top the specimen to mimic actual test conditions. The shield is positioned to minimize the amount of glare seen in the specimen images in Vic-Snap. A picture of the specimen is taken after both lenses are focused and then imported into Vic-3D.

Calibration of the DIC system is conducted using a 9 x 12 calibration board, with 9 mm spacing between the dots. The board is placed at approximately the same location as the specimen in the testing machine as shown in Figure 71. A total of forty pictures are taken of the board while it is tilted out-of-plane vertically and then horizontally followed by in-plane rotations. Standing behind the testing machine allows more room for full rotation of the board. The calibration images are imported into Vic-3D for calibration and syncing of the two cameras. Once the calibration is complete, the picture of the specimen is analyzed in the software to ensure the projection error between the two cameras is acceptable. Common error values are between 0.02 and 0.05. Once the quality of the speckle pattern is verified, the test setup could proceed.

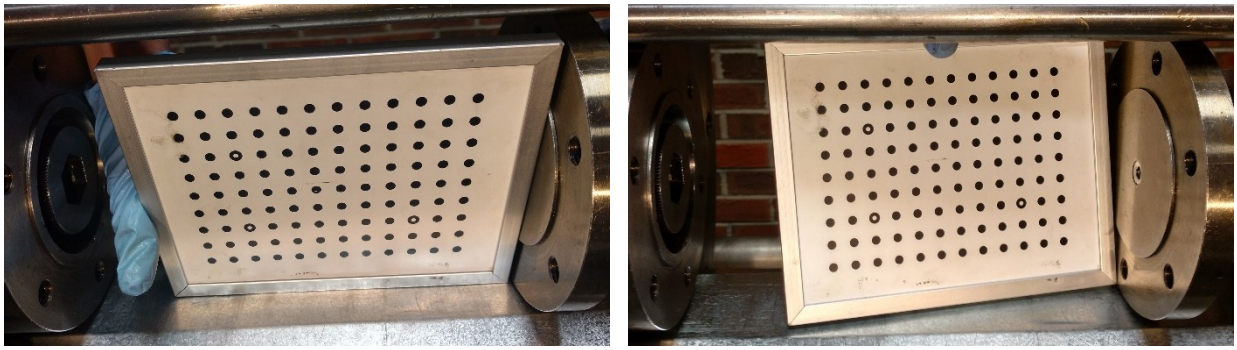

Figure 71: Out-of-plane rotations of the DIC calibration board

Appendix E: Procedure for Setting Up Testing Equipment

The tools required to install the specimen into the tri-axial testing machine are shown in Figure 72 and Table 15. Black tape is wrapped around the unpainted areas on the ends of the specimen to reduce glare. Motor assembly grease (Lubriplate No. 105, Newark, NJ, United States) is applied to the O-rings of the end caps as shown in Figure 73-1. With the specimen oriented vertically and the lead wires from the strain gauge pointing to the left of the specimen, the passive end cap is installed on the bottom of the specimen. The specimen is filled quarter full with hydraulic oil (Esso NUTO H-46, Imperial Oil Limited, Calgary, AB, Canada) as shown in Figure 73-2, and then the supply-side endcap is installed on top of the specimen. A screw for a bleed hole, circled in red in Figure 73-3, is removed using the 5/64” allen key. The specimen is filled until oil comes out the bleed hole.

Figure 72: Materials for specimen test setup

Table 15: Materials for specimen test setup

(A) Grease	(H) Monkey wrench
(B) 5/64” allen key	(J) 3/8” allen key
(C) Plank ratchet wrench	(K) End cap (supply)
(D) Snorkel	(L) End cap (passive)
(E) Screwdriver	(M) Black tape
(F) Specimen	(N) 3/8” bolts (x8)
(G) 3/8” wrench	(O) 3/8” bolts (x8)

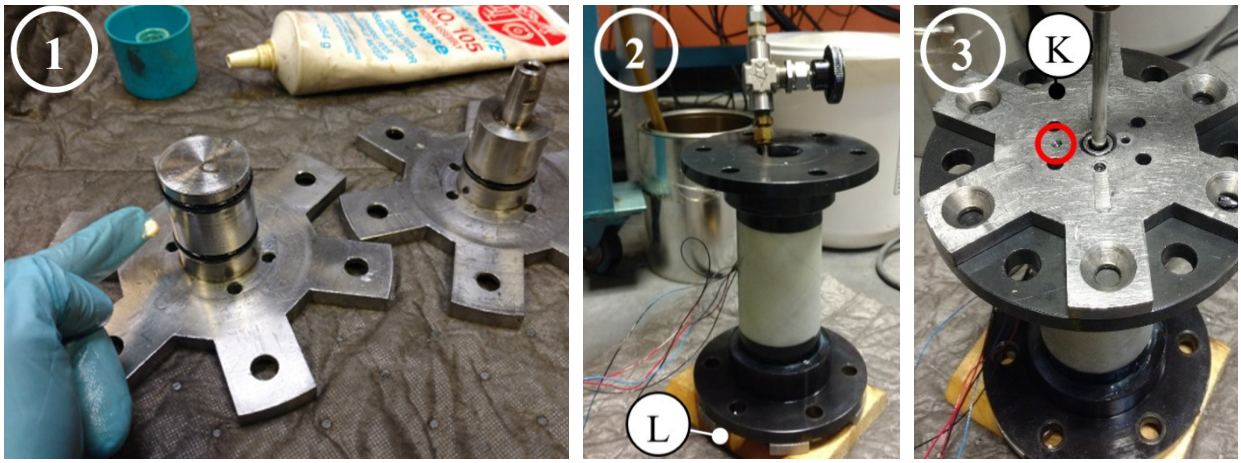

Figure 73-1 to Figure 73-3: Applying grease to o-rings and filling specimen with oil

First, the supply-side end cap is bolted into the supply side of the testing machine using six 3/8” bolts. Before operating the test micro-controller (Model 458.10, MTS), shown in Figure 74, the transducer outputs and set points are set to zero. The cover on top of the micro-controller is opened and the integrator switch for the axial position controller is turned off as shown in Figure 75 to slow the motion of the piston during installation. Axial load, internal pressure and torsional position controllers are set to active and the rotary actuator is turned on. The piston is then rotated to align its holes with the bolt holes of the passive end cap. The piston is brought into contact with the passive end cap and a small compressive load is applied. The specimen is bolted to the piston using six 3/8” bolts with the lead wires for the strain gauge leading upwards as shown in Figure 76.

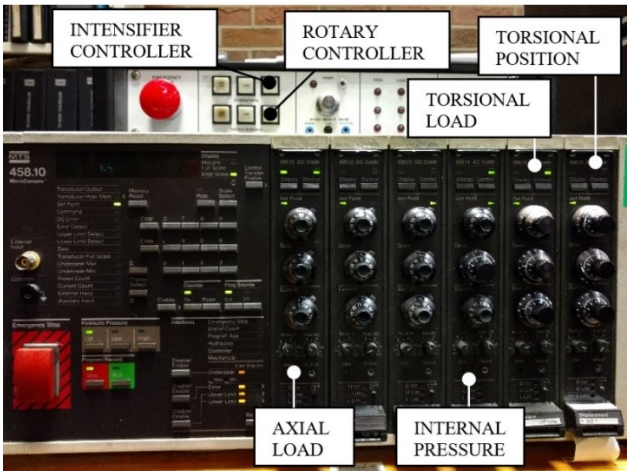

Figure 74: Analog micro-controller for testing

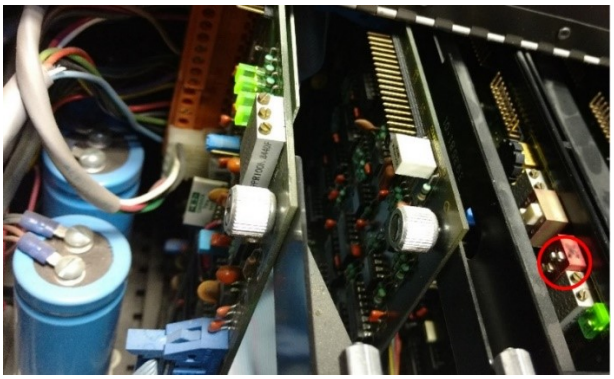

Figure 75: Turning off the integrator on the axial load circuit

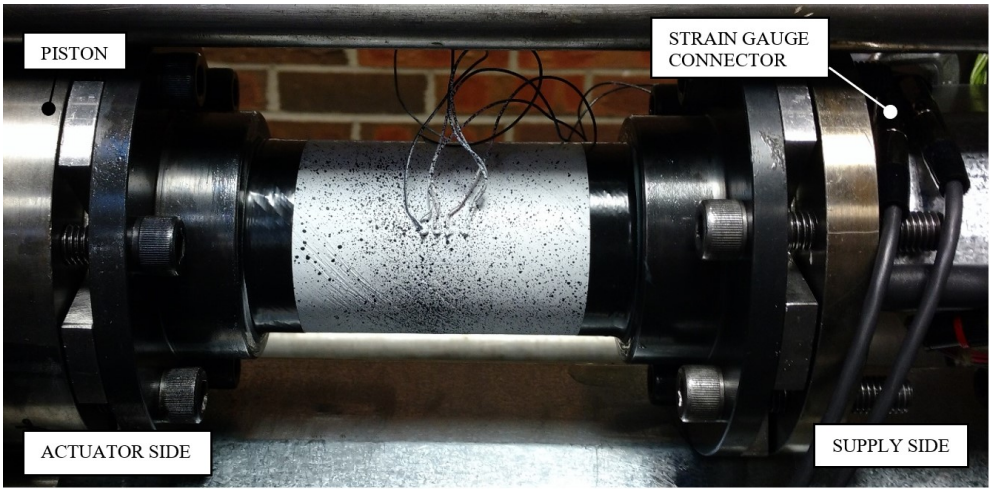

Figure 76: Specimen bolted into testing machine

The pressure intensifier can store 10 cm^3 of hydraulic oil and can be pressurized up to 68.9 MPa (10,000 psi). It is filled by opening the fill valve shown in Figure 77. The fill valve is closed once the voltage reading on the test software meter reads 9.95 V indicating the intensifier is full. The pressure reads over 2,000 psi (13.8 MPa). The set point for the pressure is adjusted to 1 psi (0.007 MPa) and the pressure intensifier controller is turned on. After waiting for approximately 30 seconds for any air bubbles in the intensifier to rise to the top, the relief valve is opened to allow air to escape. The relief valve is closed once the pressure reads 10 psi (0.07 MPa); keeping a low pressure inside the pressure intensifier allows the oil to flow easier when the specimen supply valve is opened. The specimen supply valve is then opened until a small amount of oil flows through the oil supply hose, ensuring there is no air in the hose.

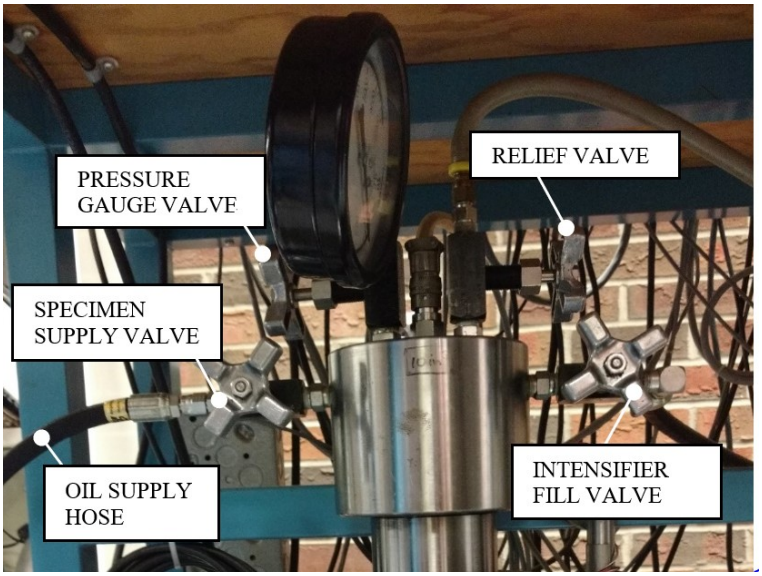

Figure 77: Valves for the pressure intensifier

The snorkel, which allows oil to be injected into the specimen, is connected to the supply side of the testing machine as shown in Figure 78-1. The oil supply hose is then connected to the snorkel as shown in Figure 78-2. The specimen supply valve is opened to connect the specimen with the pressure intensifier. Before testing, the integrator switch for the axial position controller is turned on and the axial load, internal pressure and torsional load controllers are set to active.

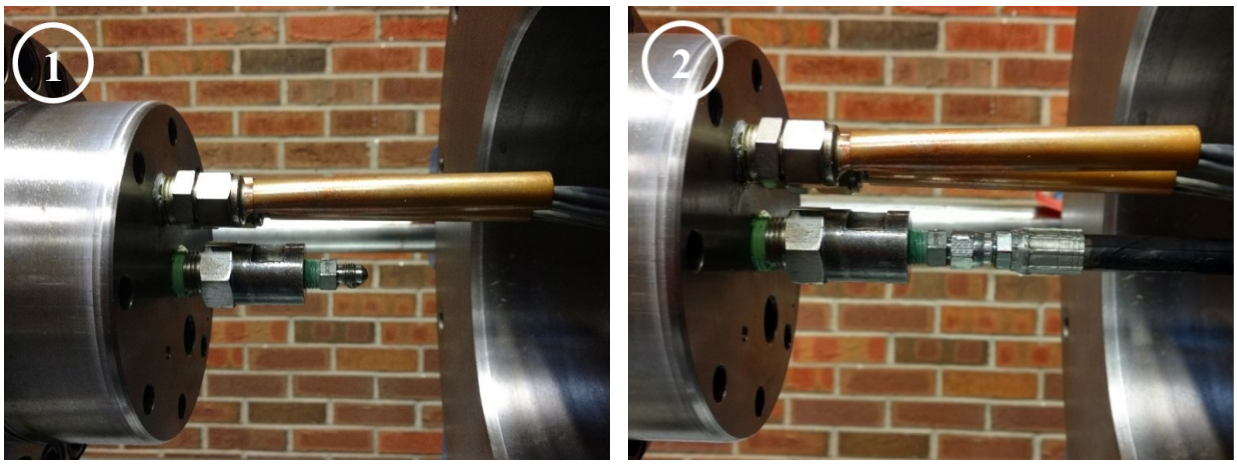

Figure 78-1 and Figure 78-2: Installing snorkel and oil supply hose

The lead wires from the specimen are connected to the dummy gauge and strain gauge connector. The placement of the dummy gauge and strain gauge connector in the testing machine is shown in Figure 79. The mass of the dummy gage is 4 g; therefore, any forces and strains caused by the weight of the dummy gauge dangling from the lead wires is considered negligible compared to the applied test loading conditions. The strain gauge condition is set to an excitation voltage of 5.000 ± 0.009 V while the amplifier and bridge balance are zeroed.

The shield is installed in front of the specimen and another picture of the specimen is taken with the DIC calibration. The projection error is confirmed be within acceptable limits, 0.02 to 0.05, for this shield placement. The Vic-Snap software is configured to take a picture every 10 seconds for the duration of the test. The test is now ready to begin.

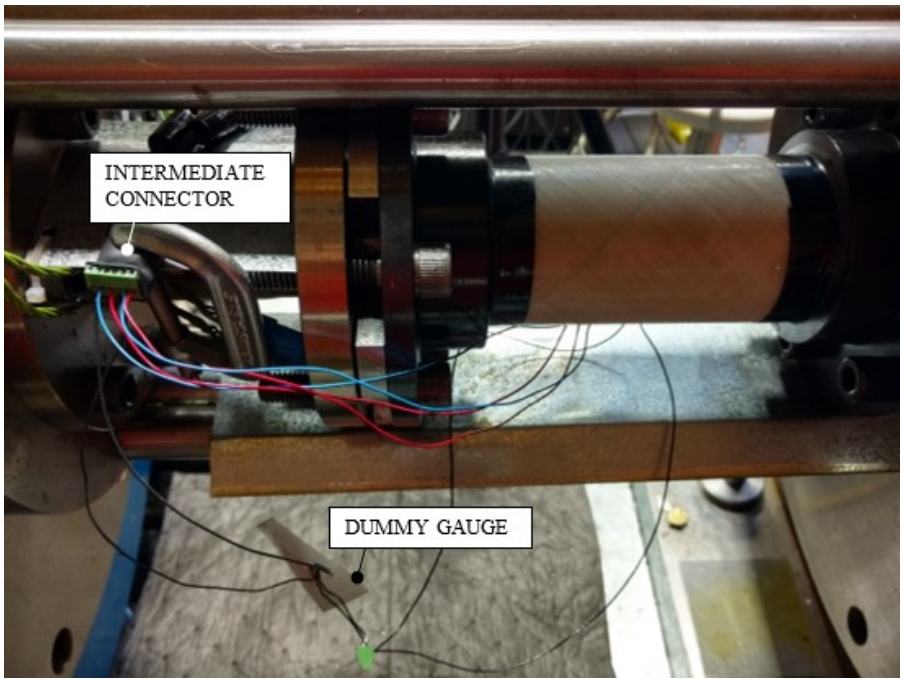

Figure 79: Arrangement for strain gauge wiring

Appendix F: Post-Test Burnout Process

The end fittings are reusable but require a burnout process to dispose of the epoxy adhesive. After testing, the specimen is removed from the tri-axial testing machine and the remaining oil in the specimen is properly disposed. The specimen is cut from the end fittings using a hacksaw. The end fittings are placed into a steel pan at an angle with the base of the outer flange facing down as seen in Figure 80. The position allows the inner sleeve to be released from the outer flange as the epoxy adhesive degrades; the clearance between the two parts exposes a greater area of the epoxy ensuring all of it would be incinerated. The pan with end fittings is placed in a ventilated oven at 450°C for 4 hours. The pan is removed from the oven after allowing the parts to cool down overnight.

Figure 80: Placement of end fittings for epoxy burnout

Appendix G: Inner Diameter and Wall Thickness Plots

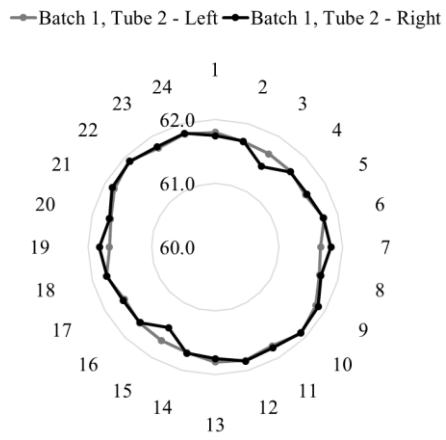

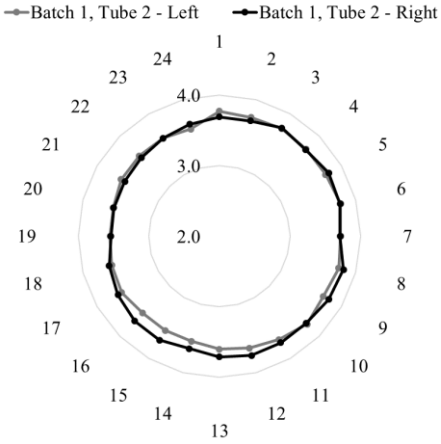

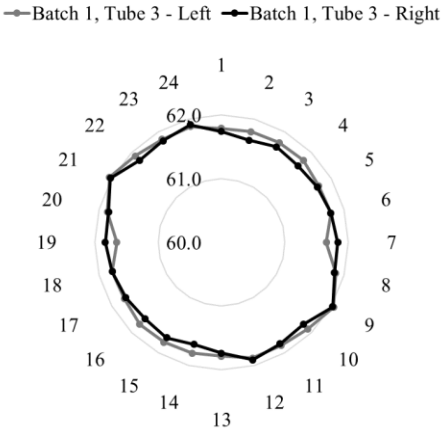

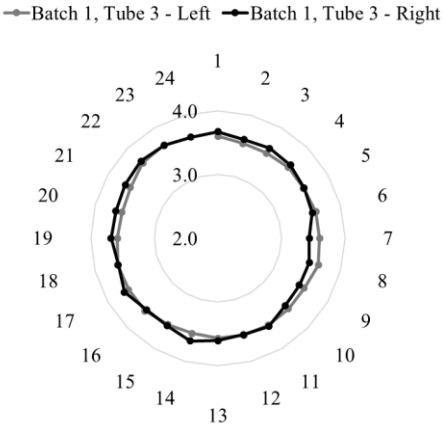

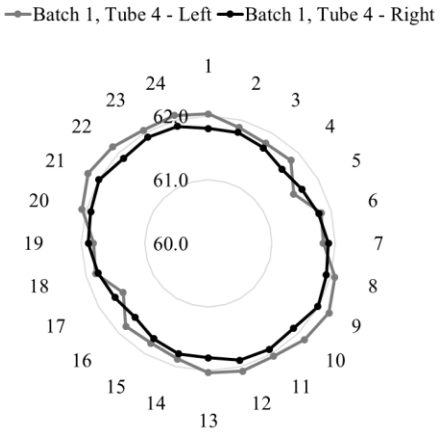

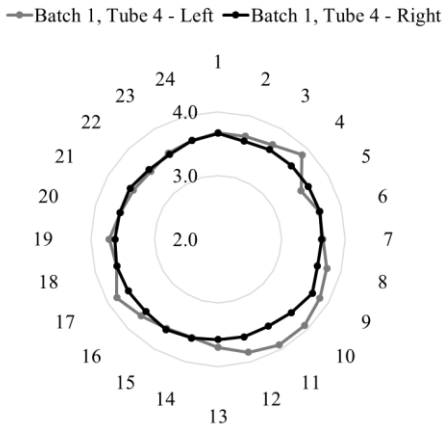

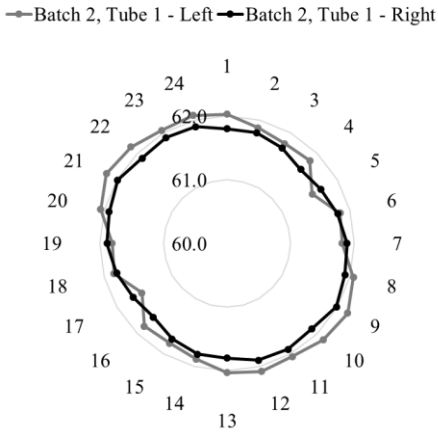
Batch 2, Tube 1 - Left
Batch 2, Tube 1 - Right
62.0
61.0
60.0

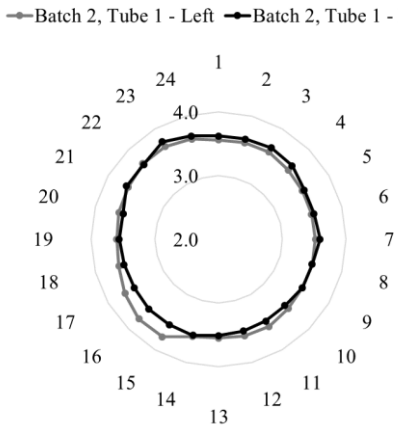
Batch 2, Tube 1 - Left
Batch 2, Tube 1 - Right
4.0
3.0
2.0

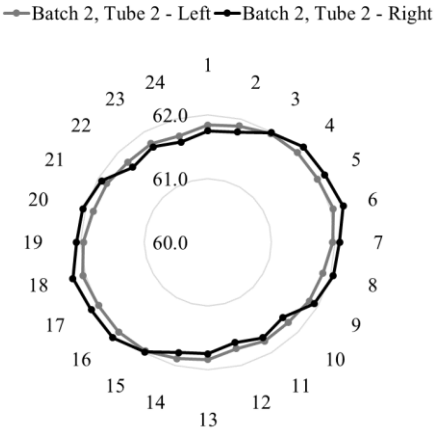
Batch 2, Tube 2 - Left
Batch 2, Tube 2 - Right
62.0
61.0
60.0

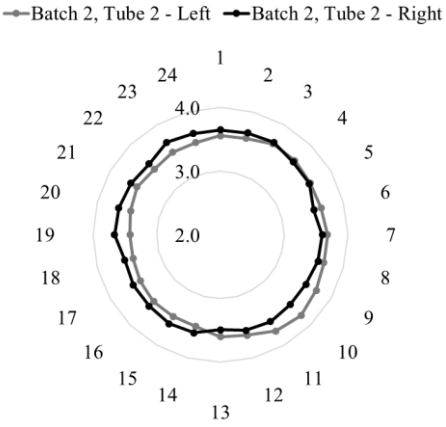
Batch 2, Tube 2 - Left
Batch 2, Tube 2 - Right
4.0
3.0
2.0

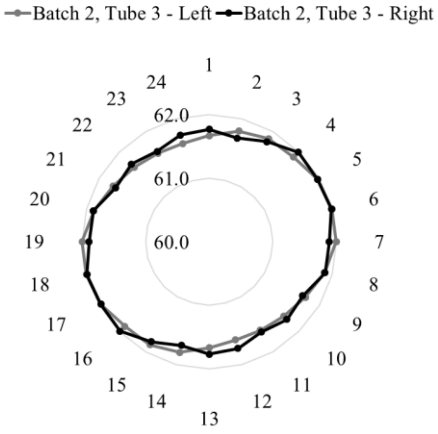
Batch 2, Tube 3 - Left
Batch 2, Tube 3 - Right
62.0
61.0
60.0

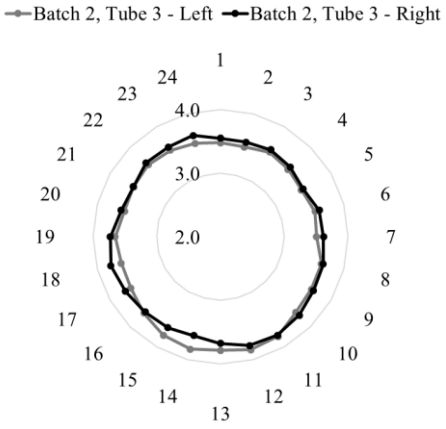
Batch 2, Tube 3 - Left
Batch 2, Tube 3 - Right
4.0
3.0
2.0

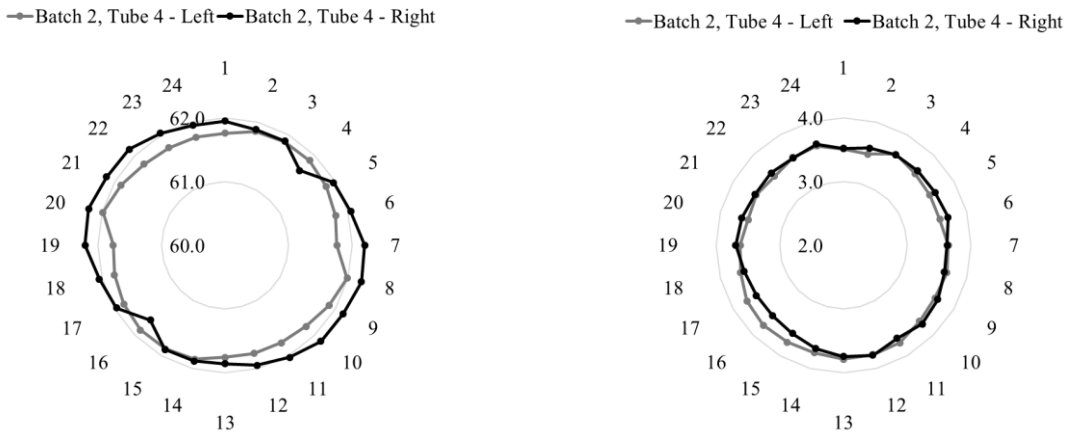

Figure 81: Inner diameter and wall thickness plots (Dimensions in millimeters)